

**ULTRA-SOFT MAGNETIC PROPERTIES OF TWO PHASE
NANOCRYSTALLINE $(\text{Fe}_{0.8}\text{Co}_{0.2})_{73.5}\text{Cu}_1\text{Nb}_3\text{Si}_{13.5}\text{B}_9$ ALLOY**

by

ISRAT ZERIN

Roll No: 100614021
Session: October 2006

A THESIS SUBMITTED TO THE DEPARTMENT OF PHYSICS,
BANGLADESH UNIVERSITY OF ENGINEERING & TECHNOLOGY, DHAKA-1000
IN PARTIAL FULFILLMENT OF THE REQUIREMENT FOR THE DEGREE OF
MASTER OF PHILOSOPHY



**DEPARTMENT OF PHYSICS
BANGLADESH UNIVERSITY OF ENGINEERING & TECHNOLOGY
DHAKA-1000, BANGLADESH
OCTOBER-2012**

CANDIDATE'S DECLARATION

This is to certify that the thesis work entitled as “**ULTRA-SOFT MAGNETIC PROPERTIES OF TWO PHASE NANOCRYSTALLINE $(\text{Fe}_{0.8}\text{Co}_{0.2})_{73.5}\text{Cu}_1\text{Nb}_3\text{Si}_{13.5}\text{B}_9$ ALLOY**” has been carried out in fulfillment of the requirement for M.Phil degree in the Department of Physics, Bangladesh University of Engineering and Technology, Dhaka, Bangladesh. It is, hereby declared that this thesis or any part of it has not been submitted elsewhere for the award of any degree or diploma. No other person's work has been used without proper acknowledgement.

Signature of the Candidate

.....

(Israt Zerin)

To the memorable person who inspired me to go for the M.Phil Course

CONTENTS

Title	Page No.
Table of contents	i-iii
List of figures	iv-vi
List of tables	vii
List of symbols	viii-ix
Acknowledgements	x-xi
Abstract	xii
 CHAPTER-I	
INTRODUCTION	
1.1 General Introduction	1
1.2 A glimpse on FINEMET	2
1.3 Aim of the present research	4
1.4 Review of researches on FINEMET	5
1.5 Overview of this thesis	7
 CHAPTER-II	
FORMATION OF SOFT MAGNETIC NANOCRYSTALLINE MICROSTRUCTURE	
2.1 Alloy design issues	8
2.2 Synthesization techniques of amorphous & nanocrystalline soft magnetic materials	9
2.3 Composition of the Nanocrystalline alloy	10
2.4 Stages of evolution of microstructure	10
2.5 Scope and constraints of choosing alloy compositions for achieving expected properties	12
2.6 Microstructure-Property relationship	15
 CHAPTER-III	
THEORETICAL ASPECTS	
3.1 Origin of magnetism	17
3.2 Types of magnetism	17
3.3 Exchange interaction and Ferromagnetic ordering	19
3.4 Theories of Ferromagnetism	20
3.5 Ferromagnetic domains	22
3.6.1 Amorphous Alloy or Metallic Glass	25
3.6.2 Theoretical understanding of amorphous alloy	26
3.6.3 Synthesization of amorphous alloys	27
3.6.4 The liquid-glass transition	28
3.6.5 Factors contributing to glass formation and stability	30
3.7 Differential Thermal Analysis and its application	31
3.8 Theory of X-ray diffraction	34
3.9 The fast cooling of the melt	35
3.10 Primary Crystallization	36
3.11 Magnetic Dipole Moments and Magnetization	38

3.12. Magnetocrystalline anisotropy and Magnetostriction	40
3.13. Random Anisotropy Model	42
3.14. Magnetic coupling in two phase microstructures	45
3.15. Concepts and Theories of Permeability	48
3.15.1. Complex permeability $\underline{\mu}$	48
3.15.2. Initial permeability μ_i	49
3.16. Permeability mechanisms	51
3.16.1. Wall permeability	51
3.16.2. Rotational permeability	52
3.17. AC magnetic response	53
3.18. High frequency behavior & losses	54

CHAPTER-IV

EXPERIMENTALS

4.1 Melt spin system	55
4.2 Preparation of Fe-based soft magnetic ribbon by melt spin system	55
4.3 Thermal Analysis Techniques	56
4.3.1 Differential thermal analysis (or DTA)	56
4.4 Annealing	58
4.5 Thermal Treatment of the amorphous ribbon	60
4.6 Powder / polycrystalline diffraction	60
4.6.1 Theoretical Considerations	60
4.6.2 Applications	63
4.6.3 Philips X'Pert Pro Multipurpose X-ray Diffractometer	65
4.6.4 Materials Geometries	66
4.6.5 Preparation of the Samples for Complex Permeability measurement	68
4.7 Inductance Analyzer	68
4.8 Initial permeability measurement	69

CHAPTER-V

RESULTS AND DISCUSSIONS

5.1 Crystallization behavior of $(\text{Fe}_{0.8}\text{Co}_{0.2})_{73.5}\text{Cu}_1\text{Nb}_3\text{Si}_{13.5}\text{B}_9$ alloy	70
5.2 DTA Results of $(\text{Fe}_{0.8}\text{Co}_{0.2})_{73.5}\text{Cu}_1\text{Nb}_3\text{Si}_{13.5}\text{B}_9$ alloy	70
5.3 Study of DTA traces of $(\text{Fe}_{0.8}\text{Co}_{0.2})_{73.5}\text{Cu}_1\text{Nb}_3\text{Si}_{13.5}\text{B}_9$ alloy	71
5.4 The activation energies for formation of nanocrystalline phase	76
5.5 A comparison between DTA results of $(\text{Fe}_{0.8}\text{Co}_{0.2})_{73.5}\text{Cu}_1\text{Nb}_3\text{Si}_{13.5}\text{B}_9$ alloy and other FINEMETs	78
5.6 Microstructure Analysis of amorphous and nanocrystalline $(\text{Fe}_{0.8}\text{Co}_{0.2})_{73.5}\text{Cu}_1\text{Nb}_3\text{Si}_{13.5}\text{B}_9$ alloy by XRD experiments	80
5.7 Identification of phases by XRD experiment	82
5.8 Lattice parameter determination	86
5.9 Silicon content in nanograins	88
5.10 Grain size determination	89
5.11 Dynamic Magnetic properties of $(\text{Fe}_{0.8}\text{Co}_{0.2})_{73.5}\text{Cu}_1\text{Nb}_3\text{Si}_{13.5}\text{B}_9$ alloy	91
5.12 Frequency dependence of initial permeability	93
5.13 Loss factors and relative quality factor	96
5.14 Frequency dependence of Relative Quality Factor	97
5.15 Curie Temperature Measurements of $(\text{Fe}_{0.8}\text{Co}_{0.2})_{73.5}\text{Cu}_1\text{Nb}_3\text{Si}_{13.5}\text{B}_9$ alloy	99
5.16 Temperature dependence of initial permeability	99

5.17 The initial permeability vs relative loss factor	103
5.18 The variation of Curie temperature with respect to annealing temperature	104
5.19 Enhancement of Curie temperature due to cobalt addition	105
CHAPTER-VI	
CONCLUSION	107
References	110

List of Figures

Fig.1.1 Relationship between permeability, μ_e (at 1 kHz) and saturation polarization for soft magnetic materials (adapted from Ref.13).	3
Fig.2.1 Flow chart for the considerations in designing and developing a nanocrystalline soft material from an amorphous precursor.	9
Fig.2.2 Schematic illustration of the formation of nanocrystalline structure.	11
Fig.3.1 Bethe–Slater curve for the magnetic exchange interaction energy as a function of interatomic spacing (normalized by spatial extent of the magnetic 3d orbitals). Also showing large variations of J with position on the left of the curve.	22
Fig.3.2 Magnetic domains in a ferromagnetic material in the demagnetized state.	23
Fig.3.3 Rotation of atomic magnetic dipole moments in a 180° (Block) domain wall in a ferromagnetic material.	24
Fig.3.4 Schematic sketches of the atomic configuration and its pair distribution function $g(r)$ in a gas, liquid, glass and crystal.	26
Fig.3.5 Schematic TTT diagram for the onset of crystallization.	28
Fig.3.6 Viscosity $\eta(T)$ and constant $\tau(T)$ for structural relaxation in a PdCuSi alloy.	29
Fig.3.7 Illustration of the effect of fine particle broadening in XRD (a) fine particles and (b) perfect crystal.[adapted from Cullity].	35
Fig.3.8 Schematic free energy concentration diagram of a model amorphous binary alloy system.	36
Fig.3.9 Typical demagnetization curves $M(H)$ (schematic). (a) Slater-Pauling curve for TM alloys (after Bozorth) (b) Spin only Slater Pauling curve for the ordered Fe-Co alloy as determined from LKKR band structure calculation (c) Density of states for Co and Fe (d) in the ordered equiatomic alloy. The Fermi level is taken as the zero of energy.	40
Fig.3.10 (a) Saturation magnetization and Curie temperature (b) magnetocrystalline anisotropy, K_1 and magnetostriction, λ in the FeCo system (reproduced from Pfeifer and Radeloff).	42
Fig.3.11 Schematic representation of the random anisotropy model for grain embedded in an ideal soft ferromagnetic matrix. The double arrows indicate the random fluctuating anisotropy axis, hatched area represents the ferromagnetic correlation volume determined by the exchange length $L=(A/K)_{1/2}$.	43
Fig.3.12. Schematic of A (filled) and B(open) atom distributions in (a) a disordered (random), (b) a structurally ordered and (c) a directionally ordered AB alloy .	46

Fig.3.13. Representation of the complex permeability.	49
Fig.3.14. Magnetization by wall motion and spin rotation .	5
Fig.3.15. Low core losses of Fe-based nanocrystalline alloy at high frequency.	54
Fig.4.1 Schematic diagram of melt spin system.	55
Fig.4.2 Melt spinning Machine.	56
Fig.4.3 Schematic illustration of a DTA cell.	58
Fig.4.4 Diffractometer Slit System.	61
Fig.4.5 Bragg reflection of two parallel incident rays 1 and 2.	62
Fig.4.6 Diffractometer Slit System.	65
Fig.4.7 X-ray Diffractometer (model : PW 3040-X'Pert PRO Philips) with high temperature attachment	65
Fig.4.8 Testing individual strip sample.	67
Fig.4.9 Inductance Analyzer (Wayne Kerr) 3255 B.	69
Fig.5.1(a) DTA trace of as cast nanocrystalline amorphous ribbon (Fe _{0.8} Co _{0.2}) _{73.5} Cu ₁ Nb ₃ Si _{13.5} B ₉ at the heating rate 10°C/min.	73
83	
Fig.5.1(b) DTA trace of as cast nanocrystalline amorphous ribbon (Fe _{0.8} Co _{0.2}) _{73.5} Cu ₁ Nb ₃ Si _{13.5} B ₉ at the heating rate 10°C/min .	73
Fig.5.1(c) DTA trace of as cast nanocrystalline amorphous ribbon (Fe _{0.8} Co _{0.2}) _{73.5} Cu ₁ Nb ₃ Si _{13.5} B ₉ at the heating rate 30°C/min.	73
Fig.5.1(d) DTA trace of as cast nanocrystalline amorphous ribbon (Fe _{0.8} Co _{0.2}) _{73.5} Cu ₁ Nb ₃ Si _{13.5} B ₉ at the heating rate 40°C/min.	73
Fig.5.2 Effects of heating rate on DTA traces of nanocrystalline amorphous ribbon (Fe _{0.8} Co _{0.2}) _{73.5} Cu ₁ Nb ₃ Si _{13.5} B ₉ at the heating rates of 10- 40°C/min.	74
Fig.5.3(a) Kissinger's plot to determine the activation energy of FeCo(Si) phase.	77
Fig.5.3(b) Kissinger's plot to determine the activation energy of boride phase.	77
Fig.5.4 XRD patterns of (Fe _{0.8} Co _{0.2}) _{73.5} Cu ₁ Nb ₃ Si _{13.5} B ₉ alloys for as cast and annealed at different annealing temperatures for 30 minutes.	84
Fig.5.5 Variation of lattice parameter with annealing temperature	85

Fig.5.6 Variation of Si% with annealing temperature	85
Fig.5.7 Variation of lattice parameter and Si% with annealing temperature	85
Fig.5.8 Variation of Grain size with annealing temperature	86
Fig.5.9 (a, b, c) Frequency dependent real part of complex initial permeability at different of $(\text{Fe}_{0.8}\text{Co}_{0.2})_{73.5}\text{Cu}_1\text{Nb}_3\text{Si}_{13.5}\text{B}_9$ alloy at annealing temperatures for constant annealing time minutes.	92
Fig.5.10 Frequency dependence of real part of complex initial permeability of $(\text{Fe}_{0.8}\text{Co}_{0.2})_{73.5}\text{Cu}_1\text{Nb}_3\text{Si}_{13.5}\text{B}_9$ alloy at different annealing temperatures for constant annealing time 30 minutes.	95
Fig.5.11 (a, b, c) Frequency vs Relative Quality factor for as cast and different annealing temperatures for constant annealing time 30 minutes.	98
Fig.5.12 (a, b, c) Temperature dependent real part of complex initial permeability of $(\text{Fe}_{0.8}\text{Co}_{0.2})_{73.5}\text{Cu}_1\text{Nb}_3\text{Si}_{13.5}\text{B}_9$ alloy at different annealing temperatures for constant annealing time 30 minutes.	102
Fig.5.13 Annealing temperature (T_a) dependence of initial permeability(μ') and relative loss factor ($\tan\delta/\mu$) for $(\text{Fe}_{0.8}\text{Co}_{0.2})_{73.5}\text{Cu}_1\text{Nb}_3\text{Si}_{13.5}\text{B}_9$ alloy, for constant annealing time 30 minutes measured at 10 kHz frequency.	104
Fig.5.14 Variation of Curie temperature with respect to annealing temperature	105

List of Tables

Table-3.1 Summary of different types of magnetic behavior.	19
Table-3.2 Spontaneous and room temperature magnetizations, magnetic dipole moments and Curie temperature for elemental ferromagnets.	39
Table-5.1 Effects of heating rate on 1 st and 2 nd crystallization states of the nanocrystalline amorphous ribbon with composition $(\text{Fe}_{0.8}\text{Co}_{0.2})_{73.5}\text{Cu}_1\text{Nb}_3\text{Si}_{13.5}\text{B}_9$.	75
Table-5.2 Comparison of the activation energies and peak temperatures of original FINEMET and $(\text{Fe}_{0.8}\text{Co}_{0.2})_{73.5}\text{Cu}_1\text{Nb}_3\text{Si}_{13.5}\text{B}_9$ alloy [5.9].	79
Table-5.3 Experimental XRD data of $(\text{Fe}_{0.8}\text{Co}_{0.2})_{73.5}\text{Cu}_1\text{Nb}_3\text{Si}_{13.5}\text{B}_9$ alloy for as cast and annealed at different annealing temperatures for 30 minutes.	81
Table-5.4 Curie temperatures obtained at different annealing temperatures.	106

List of Symbols

Angular frequency	ω
Annealing temperature	T_a
Applied magnetic field vector	\mathbf{H}_a
Anisotropy contribution to domain wall	γ_k
Atom density	$\rho(r)$
Atomic dipole moment	μ_m
Average atomic dipole moment	$\langle \mu_m \rangle$
Average magnetocrystalline anisotropy	$\langle K \rangle$
Average magnetostriction	$\langle \lambda \rangle$
Boltzmann constant	k_B/K
Bohr magneton	μ_B
Brillouin function	B_J
Coercivity	H_c
Complex permeability	$\underline{\mu}$
Critical cooling rate	R_c
Critical crystallite size	δ^*
Critical exchange length	L_0
Cross-sectional area of toroids	S
Crystallization onset temperature	T_x
Crystallization Peak temperature	T_p
Curie temperature	T_c
Curie temperature of residual amorphous matrix	T_c^{am}
Density	ρ
Diffraction angle	θ
Domain wall interfacial energy	γ_{wall}
Domain wall width	δ_w
Eddy current loss	P_e
Effective magnetic anisotropy	K_{eff}
Energy per unit area of a 180° Bloch wall	γ
Exchange correlation length	L_{ex}
Exchange energy density	J_{ex}
Exchange interaction parameter	γ_{ex}
Exchange stiffness constant	A
Fermi energy	E_F
Ferromagnetic Exchange Length	E_x
Frequency	f
Full width at half maxima	FWHM
Gas constant	R
Glass transition temperature	T_g
Grain size	D
Heating rate	β
Inter planner spacing	d

Hysteresis power loss	P_h
Imaginary part of initial permeability	μ''
Inductance	L
Initial permeability	μ_i
Internal field magnetic	H_{INT}
Lattice parameter	a_0
Loss factor	$\tan \delta$
Magnetization	M
Magnetization (magnitude)	M
Magnetic anisotropy constant	K_u
Magnetocrystalline anisotropy constant	K_1
Magnetic hardness parameter	κ
Maximum crystallite size	δ_0
Melting temperature	T_m
Modified L_{ex}	L^*
Number of spin up electrons	n_+
Number of spin down electrons	n_-
Number of turns in a coil	N
Packing fraction	p
Pair correlation function	$g(r)$
Permeability in vacuum	μ_0
Power loss coefficients	C_e, C_h
Primary crystallization temperature	T_{x1}
Quality factor	Q
Real part of complex permeability	μ'
Rotational susceptibility	χ_r
Saturation magnetization	M_s
Saturation polarization/magnetization	J_s
Secondary crystallization	T_{x2}
Spin up density of states	$g_+(E)$
Spin down density of states	$g_-(E)$
Spin vector	S
Structural anisotropy	k^*
Susceptibility	χ
Thickness of the Bloch wall	δ
Temperature difference	ΔT
Uniaxial magnetic anisotropy	K_u
Viscosity	η
Volume fraction	v_{cr}/X
Wall susceptibility	χ_w
Wavelength	λ
Weiss molecular field constant	λ_w

Acknowledgement

At first, true regards to my Supervisor, Dr. Md. Feroz Alam Khan, Professor, Department of Physics, Bangladesh University of Engineering and Technology who granted me as his student to undertake this research project. His guideline helped me continue my research and establish my thesis.

I want to acknowledge the memorable guidance of my Co-supervisor, Dr. A.K.M. Abdul Hakim, (Retd.) Chief Engineer, Material Science Division (MSD), Atomic Energy Centre (AEC), Dhaka who has provided consistent support and necessary motivations to progress my thesis work.

My true respect and gratitude to Dr. Md. Mostak Hossain, the Head, Department of Physics, Bangladesh University of Engineering and Technology, who helped me with all necessary supports to make authentic steps towards the achievement of an M.Phil degree.

My best regards all honorable professors of the Department of Physics including Prof. Dr. Abu Hashan Bhuiyan, Prof. Dr. Jiban Podder and Prof. Dr. A.K.M. Akhter Hossain who made memorable motivations for me different times. Honest gratitude to the honorable tabulator Dr. Md. Rafi Uddin, who necessarily supported towards proceeding for the publication of my M.Phil result. Earnest thanks to Dr. Mohammed Abdul Basith who patiently went through my thesis by each and every word and suggested for necessary corrections. My heartfelt regards to all other faculty members of the Department of Physics, BUET who are inspirations for me to go on with a research in the area of Material Science.

My sincere thanks to Dr. Sheikh Manjura Hoque, Principal Scientific Officer, Material Science Division, AECD, who provided valuable guidelines for my work. Honest gratitude to Dr. Dilip Kumar Saha, CSO, AECD who supported me to perform the XRD experiment in the existing laboratory of AECD.

My earnest regards and thanks to Dr. Md. Tofazzal Hossain, Member, Science program in BCSIR for his kind cooperation to prosecute the experiments to be done in relevant laboratories here. My honest gratitude to Dr. M.A. Gafur, Sr. Engineer, PP & PDC, Bangladesh Council for Scientific and Industrial Research (BCSIR), Dhaka for providing kind opportunity to work in his laboratory for experimental purposes regarding my thesis.

I also thank all the office staffs and laboratory assistants of the Department of Physics, Bangladesh University of Engineering and Technology who helped me at every respect to proceed the course work.

My heartfelt honour and thanks to Nazrul Islam Khan, who was the first to inspire me to go for an M. Phil degree course in BUET. I am indebted to my family which has been my consistent support notwithstanding the academic respect. The support of Taslima Akter is worth to mention for whom I could never back down. I can't help mentioning my eldest maternal uncle, Late Abdus Samad whose admiration to me is always memorable. The cooperation of Subrata Roy is not forgottable. I gratefully thank to Dr. Sarwat Noor, who helped me providing and suggesting comparable reports to be helpful for analyzation of my experimental results. Thanks to Md. Forhad Hossain who once wasted his valuable time helping into organization of a part of my thesis presentation. Honest thanks to Mr. Kabir who helped me in a small calculation which came into its solution. The kind cooperation of Harinarayan Das, Scientific officer of AECD is thankfully mentionable.

I express my gratitude to the authority of BSTI who kindly permitted me to end up my M.Phil degree course in spite of my office responsibility. I also express my heartfelt thanks to my superiors in the office as well as my colleagues who more or less supported me to make my duties easier and with necessary relief.

My sincere thanks to the Director, Atomic Energy Centre, Dhaka (AECD), who kindly permitted me to use the laboratory facilities existing in the Material Science Division (MSD), Atomic Energy Centre (AEC), Dhaka.

Lastly, I gratefully acknowledge the authority of Bangladesh University of Engineering and Technology to provide me this great opportunity to continue the M.Phil Course with all kinds of academic, financial and institutional supports.

ABSTRACT

Amorphous ribbon of composition $(\text{Fe}_{0.8}\text{Co}_{0.2})_{73.5}\text{Cu}_1\text{Nb}_3\text{Si}_{13.5}\text{B}_9$ was prepared by rapid quenching method at wheel speed of 25 m/s in an Ar atmosphere. The alloy has been annealed in a controlled way in the temperature range of 400-700°C for 30 minutes. Crystallization onset temperature for FeCo(Si) phase was found 525°C from Differential Thermal Analysis Experiment and from the obtained data, the activation energy was calculated to be 3.11eV. Amorphosity of the ribbon and nanocrystalline state was evaluated by X-ray diffraction. In the optimized annealing condition the grain size has been obtained in the range of 2-26 nm. Temperature and frequency dependence of permeability of amorphous and devitrified toroid shaped samples have been measured. The low frequency value of μ' increases with the increase of annealing temperature up to 550°C. Very low value of relative loss factor of the order of about 10^{-2} has been observed at this annealing temperature. It is notable that the addition of Co has significant effects on enhancement of Curie temperature. In the as-prepared condition the Curie temperature has been found to be 421°C, which is quite high compared to the Curie temperature of conventional FINEMET (i.e. sample without Co), which is about 354°C. Enhancement of Curie temperature occurs with increasing annealing temperature up to 475°C. As the nanocrystalline phase appeared, it was found that at and above the crystallization temperature, the Curie temperature of the residual amorphous phase gradually decreases with the increase of annealing temperature. This is because the amorphous matrix is depleted with Fe and relative amount of Nb in the amorphous matrix increases, which weakens the exchange interaction resulting in reduction of Curie temperature.

1.1 General Introduction

Magnetic materials played a prominent role in the discovery of new civilizations and also development of modern technology. The use of magnetic materials has been extended from the utility industries to others include communication, computer, audio-visual and home appliances, to name just a few.

Magnetism is one of the basic properties of materials. Magnetism appears in various forms, but one of the kinds that have practical value and therefore interests us is soft magnetic materials. The term ‘soft’ means temporary in the sense that ferromagnetism emerges only when a magnetic field is applied. In contrast, hard or permanent magnets display ferromagnetism even in the absence of external field. All magnetic elements in the pure form are soft; whereas magnetic solid solutions and compounds can be either soft or hard. The distinguishing characteristic of the first type is high permeability which as usual, is accompanied by low coercivity. It is the flux-multiplying power of the magnetically soft materials that fits them for their jobs in machines and devices.

Soft magnetic materials are basically required to have high initial or maximum permeabilities or susceptibilities and low losses; that is to say, the permeabilities should remain high over a considerable range of frequencies.

Soft magnetic materials face demanding requirements from new, high-performance electronic and power distribution systems. The new systems must operate in high temperature and high-frequency regimes that are inaccessible to conventional crystalline and amorphous magnetic materials. The need for increased energy efficiency requires reduced power loss from inductive components.

The enhancement of soft magnetic properties requires reduction of crystalline grain sizes to a much smaller length scale that can overcome the anisotropy effects and result in an improved soft magnetic behavior. This needs for a look into ‘Nanoscience’ which has made immense progress in previous respects within the last decades.

Nowadays, the attempts to understand different properties of materials on a smaller and smaller length scale are making footsteps for development of research in many areas of material science. With the reduction of size into nanometer range, the materials exhibit interesting properties including physical, chemical, mechanical, magnetic and electrical, comparing to conventional coarse-grained counterparts. This new field based on nanomaterials has been named as ‘Nanotechnology’ and emerged as a new branch of science and technology.

Nanomaterials can be classified into nanocrystalline materials and nanoparticles. The former are polycrystalline bulk materials devitrified from the previously synthesized amorphous precursor through appropriate thermal treatment with grain sizes into nano-meter range (< 100 nm) while the latter refers to ultrafine dispersive particles with diameters < 100 nm.

Nano-crystalline materials are distinguished from conventional polycrystalline materials by the size of crystallites that compose them. Defined broadly the term nanostructured is used to describe materials characterized by structural features in the range of ≈ 1 - 10 nm corresponding typically to ≈ 50 - 5×10^7 atoms respectively.

The soft magnetic properties of nano-materials are connected with size, distribution of the nano-metric grains, their composition, interfaces of constituent phases, vanishing magnetic anisotropy ($\langle k \rangle \approx 0$), vanishing magnetostriction ($\langle \lambda \rangle \approx 0$), strong intergrain magnetic coupling and reduced magnetic-elastic energy.

Nanocomposite magnetic materials have their origin in the amorphous alloys that are characterized by a lack of long range atomic order. Amorphous alloys were brought to market in the 1970's. Production techniques for amorphous materials include rapid quenching from the melt, mechanical alloying, plasma processing and physical vapor deposition, etc. [1.1, 1.2]

1.2 A glimpse on FINEMET

A new class of Fe based alloys was introduced by Yoshizawa, Oguma and Yamauchi, in 1988 which exhibited superior soft magnetic behavior. The material was produced by crystallization of an amorphous Fe-Si-B alloy with small additions of Cu and Nb. The identifying characteristic of the new material is its ultrafine microstructure of Fe-Si with grain sizes of 10-15 nm from which their soft magnetic properties emerge. These include coercivities of 0.01 Oe and permeabilities of $\sim 10^5$. The alloy system, originally proposed as Fe-Cu-Nb-Si-B alloys, was manufactured by Hitachi Co. Ltd. under the tradenames FINEMET [1.3]. The originally proposed composition was $\text{Fe}_{73.5}\text{Cu}_1\text{Nb}_3\text{Si}_{13.5}\text{B}_9$.

The unique properties of FINEMET alloys include low losses, high permeability and near-zero magnetostriction achieved by permalloys and Co-based amorphous alloys, but much higher saturation magnetization up to 1.3 Tesla, than these materials usually have ever offered.

In fig.1.1 [1.4], figures of merit for Co-base amorphous alloys, Fe based amorphous alloys and nanocrystalline alloys are summarized. Co-base amorphous alloys, Fe based amorphous alloys and nanocrystalline alloys have evolved over past decades with soft magnetic properties which now exceed those of bulk alloys based on Co, Fe and Fe-Co.

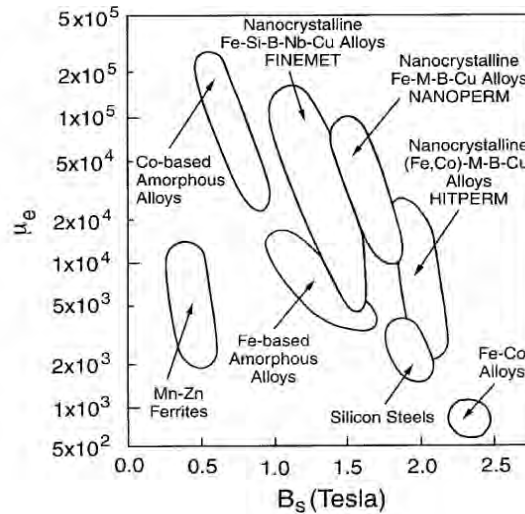


Fig.1.1 Relationship between permeability, μ_e (at 1 kHz) and saturation polarization for soft magnetic materials (adapted from Ref. 1.4)

With a view to improve the soft magnetic behavior of FINEMET type alloys, partial substitution of Fe with various elements has been widely investigated [1.5-1.6]. It was found that the partial substitution of Fe by Co leads to the increasing of magnetic moment and Curie point of the amorphous phase. Controlled Co addition [1.7-1.9] enhances the Curie temperature of the resulting nanocrystalline material while good soft magnetic properties are also observed at elevated temperature, thus making these materials appropriate for working at high temperature [1.10]. Adding Co is also expected to be beneficial to induce in-plane magnetic anisotropy to ribbons by magnetic field annealing, because the substitution of Fe with Co is known to be effective for increasing the magnetic anisotropy constant, K_u , of Fe-Si-B amorphous alloys. A large K_u can increase the magnetic resonance frequency, which is advantageous for the good permeability-frequency (μ - f) property in a high frequency region [1.11].

It is well known that the microstructure, noticeably the grain size, essentially determines the hysteresis loop of a ferromagnetic material. From the nanometer regime to macroscopic grain sizes- the permeability shows an analogous behavior being essentially inversely proportional to H_c . Lowest coercivities, however are again found for smallest structural correlation lengths like in amorphous alloys (“grain size” of the order of atomic distances) and in nanocrystalline alloys for grain sizes $D < 20$ nm.

In magnetic materials, the ‘Ferromagnetic Exchange Length (L_{ex})’ expresses the characteristic distance over which a magnetic atom influences its environment, and has values on the order of 100 nm. If the magnet has a structure with grain diameters smaller than the average length, it

becomes possible to “average” the anisotropy of the grains to a low bulk value. Under the sequence of this randomized anisotropy, such a material realizes the high saturation magnetization, M_s in the crystalline state and low coercivity, H_c due to randomized anisotropy. Accordingly magnetic softening should occur as soon as the structural correlation length or grain size (D) becomes smaller than the Ferromagnetic Exchange Length (L_{ex}) which is in the order of domain wall width. In this case, the local anisotropies are randomly averaged out by exchange interaction so that there is no anisotropy net effect on the magnetization process. It is well accepted that good magnetic properties are obtained when $D \ll L_{ex}$ [1.12].

1.3 Objective of the present research

In the present work, soft magnetic amorphous FINEMET type alloy with nominal compositions of $(Fe_{0.8}Co_{0.2})_{73.5}Cu_1Nb_3Si_{13.5}B_9$ synthesized by a melt-spinning technique is reported.

To improve the magnetic properties of these amorphous ribbons, microstructure is an important parameter that can be controlled by heat treatment condition. Also one effective way of preparing nanocrystalline alloy via the amorphous state of material is an appropriate heat treatment that has been found leading to a two-phase crystallization. The nanostructures are often obtained by primary crystallization. As a consequence, the aim of current study is to observe the microstructural evolution as a function of heat treatment temperature.

As the composition of a primary crystal differs from that of an amorphous matrix, the process of crystal growth becomes diffusion controlled. In order to control the growth process of nanostructured alloys, it is important to investigate the kinetics of crystallization. The crystallization of these metallic glasses enables the study of both nucleation and growth processes. Thus the main objective of this thesis is to describe the kinetics of solid phase transformation taking place on the nano-scale, i.e., a study of nanocrystallization which promotes the evolution of superior soft magnetic properties in the studied composition.

In this research work the kinetics of crystallization of amorphous FINEMET type alloys were investigated by the use of Differential Thermal Analysis (DTA) and X-ray Diffraction (XRD) Technique. The combination of these two techniques is necessary for the complete description of the processes occurring during the nanocrystallization from amorphous precursors as well as microstructural evolution in FINEMET type alloys in its crystalline state. Results will aid in interpreting the effect of heat treatment on magnetic properties and application of this type of alloys. Finally, magnetic properties were studied by using an Inductance Analyzer.

The present sample is obtained by replacement of 14.7% cobalt for iron as a transitional element. It can be observed that in this composition Fe has been partially replaced by Co as comparing to original FINEMET alloy of the composition $\text{Fe}_{73.5}\text{Cu}_1\text{Nb}_3\text{Si}_{13.5}\text{B}_9$. Cobalt is well known for its anisotropy effect which would play an important role on both structural and magnetic phase transition temperature. It may be mentioned that magnetocrystalline anisotropy constant K_1 of Co is $4.3 \times 10^5 \text{ J/m}^3$ whereas that of Fe is $-4.5 \times 10^3 \text{ J/m}^3$. Higher value of magnetocrystalline anisotropy constant of Co shows that the presence of Co in the alloy system would give rise to frequency stability of permeability compared to original FINEMET which will increase the resonance frequency to higher value. Further, Curie temperature of Fe and Co are 770°C and 1127°C , respectively. Replacement of Co for Fe would enhance the Curie temperature because of the much higher magnetocrystalline anisotropy of Co which increases thermal stability of this type of alloy from application point of view. This is an important characteristic of this type of alloy.

1.4 Review of researches on FINEMET

This review is intended to summarize recent developments in the synthesis, structural characterization, properties and applications of nanocrystalline and amorphous magnets.

The study of Yoshizawa *et al.* [1.13] and Noh *et al.* [1.14] on the role of nucleating agent Cu on the crystallization behavior of the composition $\text{Fe}_{73.5}\text{Cu}_1\text{Nb}_3\text{Si}_{13.5}\text{B}_9$ revealed that the average grain size is relatively large at crystallization temperature due to lower crystallization rate with no addition of Cu and annealing of this Cu free alloy leads to simultaneous or sequential formation of several crystalline phases. Kataoka *et al.* [1.15] verified the role of Au in place of Cu and reported that Au is the only element, which has a comparable effect on the crystallization behavior.

Müller *et al.* [1.16] showed that like Nb, the atomic volumes of refractory elements (group V or VI elements (Cr, V, Mo, W or Ta)) are larger than that of Fe that reduces diffusion coefficients and thus stabilizes the amorphous matrix and slows down the kinetics of grain coarsening. The efficiency of these elements for grain size refinement increases in the order of their atomic volumes i.e., $\text{Cr} < \text{V} < \text{Mo} \approx \text{W} < \text{Nb} \approx \text{Ta}$. Thus, finest grain structures and superior magnetic properties require a certain amounts of elements Nb and Ta. Inoue *et al.* [1.17] observed that group IVa to VIa transition metals extends the glass forming range at low Si or B contents. The glass forming range is the widest for Hf containing alloys and decreases in the

order $Zr > Nb \approx Ta > Mo \approx W > V > Cr$. According to Suzuki *et al.* [1.18, 1.19] the glass forming ability is considerably improved with the addition of Hf or Zr.

Herzer [1.20] reported that in amorphous state the onset crystallization temperature is almost same for B content (at.%). But for annealed sample, the onset crystallization temperature decreases with increasing B content (at.%). Thus B content should be kept at a low or moderate level in order to obtain an optimum nanoscale structure. Like B in $Fe_{73.5}Cu_1Nb_3Si_{13.5}B_9$, another glass forming element is Si that cannot be simply reduced without substituting other glass formers for it.

Suzuki *et al.* [1.18], Alben *et al.* [1.21] and Sawa *et al.* [1.22] worked on the relation of grain size and domain wall width. If the grain size exceeds the domain wall width, domains can be formed within the grains and the coercive field, H_c is found to depend on the grain size, D as $H_c \propto D^6$.

Dalpadodo *et al.* [1.23] and G. Butinno *et al.* [1.24] studied the effect of annealing temperature on H_c . Due to stress produced during the quenching process the as-quenched metallic glasses always have anisotropy. Anisotropy is averaged out after annealing because annealing can relieve stress and causes reduction of H_c . Hence annealing makes the amorphous ferromagnet a magnetically soft material.

Herzer [1.12] studied on Curie temperature and permeability of nanocrystalline material. According to him when measuring temperature approaches the Curie point of the intergranular amorphous phase, the exchange coupling between the crystallites is largely reduced. As a result, the initial permeability drops down. As reported by Hakim *et al.* [1.25], magnetic initial permeability of nanocrystalline amorphous ribbon strongly depends on annealing temperature and exhibits superparamagnetic behavior at $T > T_c$.

Franco *et al.* [1.26] also studied the superparamagnetic relaxation in FINEMET type of alloy Fe-Cu-Nb-Si-B without adding any extra refractory element and they have demonstrated that this behavior is a general characteristic of this nanocrystalline alloys provided the volume fraction of crystallites are very low. If the size of the nanocrystals is small enough and the intergranular amorphous matrix is sufficiently thick to minimize the magnetic interactions between them, the superparamagnetic behavior of the nanocrystalline particles is expected.

There have been done so many researches [1.6-1.11] on various effect of replacement of Co for Fe as a late transitional metal element. The research on Co substituted Fe-Nb-Ta-Mo-B amorphous alloys [1.27] showed that Co substitution increased saturation magnetization and Curie temperature of the amorphous phase and decreased coercivity.

1.5 Overview of this thesis

After a brief introduction about the history, application and interest for this research work in sections 1.1 and 1.2, the specific research interests are described in section 1.3 of introductory chapter leading to a review on FINEMET material in the preceding section, 1.4.

The research presented in this thesis proceeds to experimentally investigate the crystallization process during annealing of amorphous precursors and to compare these results with the physical models that describe grain nucleation and grain growth during the transformation. As controlled annealing produces nanosized grain through primary crystallization Chapter 2 reviews the phenomena based on the basis of the grain refinement mechanism and the physical models that explain the transformation kinetics during heat treatment of amorphous samples. Different theoretical viewpoints on crystallization and magnetic behavior of materials is depicted in chapter 3. The experimental techniques applied in this study are described in chapter 4. These experimental techniques involve Differential Thermal Analysis (DTA), X-ray Diffraction (XRD), frequency and temperature dependent initial permeability as well as loss factor of toroid-shaped samples measured by an inductance analyzer.

Based on different experimental techniques, results and discussions are presented in Chapter 5. Finally all outcomes from this investigation are summarized in chapter 6. Magnetic nanocomposites comprised of nano-sized magnetic crystals embedded in an amorphous matrix have been shown to have excellent soft magnetic properties. In particular, amorphous and nanocrystalline materials have been investigated for various soft magnetic applications including transformers and inductive devices. In these materials, it has been determined that an important averaging of the magnetocrystalline anisotropy over many grains coupled within an exchange length is at the root of magnetic softness of these materials. The crystallization kinetics and the chemical partitioning occurring during crystallization will be described essentially. In particular, the role of the amorphous phase in exchange coupling magnetic nanoparticles at elevated temperatures will be discussed. Furthermore, the effect of addition of Co on frequency and thermal stability of the alloy draws much interest for the present research from the viewpoint of application.

2.1 Alloy design issues

Alloy design issues include issues of chemistry and processing designed to (1) optimize one of a number of important intrinsic and/or extrinsic magnetic properties as well as to (2) structural or microstructural features which promote important (usually extrinsic) magnetic properties.

The first of these issues concerns the choice of chemistry to impact the intrinsic magnetization of the material. The second issue pertinent to alloy additions designed at aiding formation of an amorphous phase.

The desire for large magnetic inductions typically limits choices to alloys of Fe and Co (the elemental transitional metal magnets with the largest atomic dipole moments). Curie temperatures are also largest for elemental Fe(770°C) and Co(1127°C), suggesting the use of Fe or Co (or Fe-Co) alloys especially in high temperature applications.

As intrinsic properties we take to mean microstructure insensitive properties including the saturation magnetization, Curie temperature, magnetocrystalline anisotropy and magnetostrictive coefficients are all important. Also it includes magnetic dipole moment and exchange interaction. Extrinsic magnetic properties important in soft magnetic materials include the magnetic permeability and coercivity, which typically have an inverse relationship. Also induced magnetic anisotropy and magnetic coupling through amorphous phases are included to these properties. Magnetic anisotropy and magnetostriction can be considered as extrinsic (microstructure sensitive) in the sense that for a two phase material (in aggregate) they depend on microstructure.

Since microstructure of alloy influence extrinsic magnetic properties, the important microstructural features should be recognized including grain size, shape and orientation, defect concentrations, compositional inhomogeneties, magnetic domains and domain walls.

The development of soft magnetic materials for applications requires attention to a variety of intrinsic magnetic properties as well as development of extrinsic magnetic properties through an appropriate optimization of the microstructure.

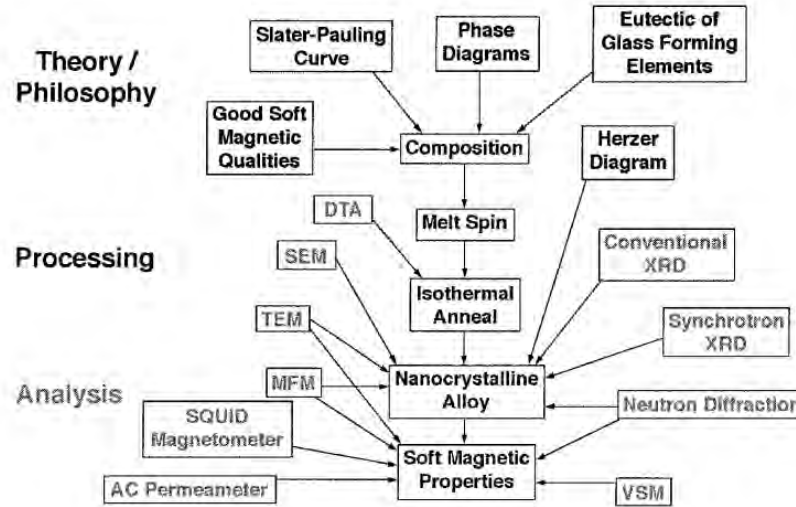


Fig.2.1. Flow chart for the considerations in designing and developing a nanocrystalline soft magnetic material from an amorphous precursor.

2.2 Synthesization techniques of amorphous & nanocrystalline soft magnetic materials

There are different techniques to synthesize nanocrystalline alloys [2.1] such as: (1) Rapid Solidification from the liquid state, (2) Mechanical Alloying (3) Plasma processing and (4) Vapour Deposition. Due to introduction of some undesired micro structural condition, only the first method have been proved suitable. We have to choose the process of synthesization which fits best to enhance the soft magnetic properties overcoming all risks of introducing any adverse effect that deteriorates the soft magnetic properties; that is which may not introduce any internal strain or unfavourable intergranular linkage which would reduce the ferromagnetic coupling between the grains.

The only method presently available to synthesize nanocrystalline alloys with attractive soft magnetic properties is the controlled crystallization. Following this method, the amorphous pre-cursor material can be prepared in two ways: either (1) as a thin film by sputtering techniques or (2) as a ribbon by rapid solidification from a melt. The second one is a well established technique for large scale production of amorphous metals.

A nanocrystalline structure with good soft magnetic properties can be achieved if primary crystallization of body centered cubic Fe, originated from amorphous state occurs before inter-metallic phases like Fe-B compounds may be formed. In order to obtain a nanoscaled microstructure, both an extremely high nucleation rate and slow growth of the crystalline precipitates are required. An appropriate alloy design accompanied with a controlled

crystallization based on isothermal annealing can bring successful achievement of a nanostructured soft magnet. The constraint regarding alloy design is, only particular kinds of elements should be chosen from the periodic table which would simultaneously-(1) have a good glass forming ability, (2) promote the nucleation of Fe, (3) retard the grain growth and (4) inhibit the formation of intermetallic phases.

2.3 Composition of the Nanocrystalline alloy

Generally, the optimum mechanical and magnetic properties of nanocrystalline soft magnetic materials are obtained for partially crystallized materials. This means that these materials are formed in two phases. [2.1]

This composition usually consists of a late ferromagnetic transition metal elements (Fe, Co or Ni) as possible. The remaining early or middle transition metals (Zr, Nb, Hf, Ta, etc.) and metalloids (B, P, Si, etc.) are added to promote glass formation in the precursor. The noble metal elements (Cu, Ag, Au, etc.) serve as nucleating agents for the ferromagnetic nanocrystalline phase. The compositions are limited by where glass formation can occur prior to the nanocrystallization route. These alloys may be single phase (Type I) but are generally two phase materials with a nanocrystalline ferromagnetic phase and a residual amorphous phase at the grain boundaries (Type II). In the ongoing research we are only interested about the second type.

One of the important features of this magnetic system is that one can play with different compositions, annealing temperatures and time to control the grain size and their distribution upon which the magnetic properties of these new materials strongly depend. In choosing the composition, one has to consider the magnetic component like Fe, Co or Ni, the crystallization initiating component e.g. Cu and the component Nb or Ta for stabilizing the nanocrystal by inhibiting the grain growth and glass forming materials like Si, B etc.

2.4 Stages of evolution of microstructure

Formation of the nanocrystalline microstructure in the amorphous phase was depicted by G.Herzer in the ‘nanocrystalline soft magnetic alloys’ [2.2]. Fig.2.2 presents the steps of formation of the nanocrystalline microstructure from the amorphous state.

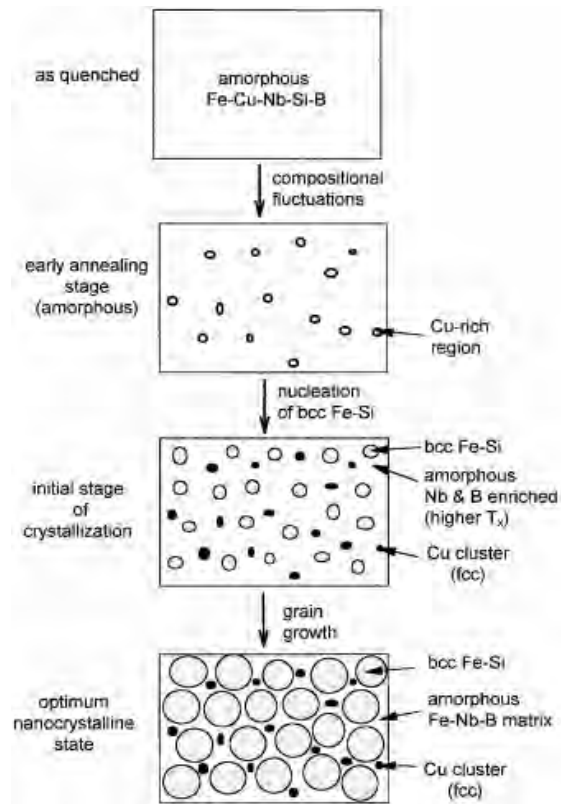


Fig.2.2 Schematic illustration of the formation of nanocrystalline structure [2.2].

The formation of the particular nanocrystalline structure is essentially related to the combined addition of Cu and Nb (or other group IV or VI elements) and their low solubility in Fe-Si (<0.2 at% Cu, <0.1 at% Nb): copper enhances the nucleation of grains while Nb impedes grain coarsening and at the same time, inhibits the formation of boride compounds. The microstructure evolution is schematically illustrated in Fig.2.2 can be summarized as follows:

Annealing at temperatures in general between about 500°C to 600°C leads to primary crystallization of the Fe. At the initial stage of annealing, before the onset of crystallization, the phase-separation tendency between Cu and Fe leads to the formation of Cu-rich clusters, with 5 nm size and probably still amorphous. [2.3-2.4]. The presence of Nb seems to promote the formation of these Cu-rich clusters on a much finer scale than in an Nb-free alloy composition [2.5].

This cluster formation causes a concentration fluctuation of Fe, since Cu substitutes for Fe. Thus, the regions in between Cu-rich clusters provide a significantly increased density of nucleation sites for the crystallization of Fe. The consequence is an extremely fine nucleation

of Fe-Si crystallites at a high rate which subsequently grow in a diffusion controlled process [2.6] as the annealing proceeds further.

As the Fe-Si phases forms, Nb and B are excluded from the crystallites because of their low solubility in b.c.c Fe-Si and are enriched in the residual amorphous matrix. At the same time all Si effectively tends to be partitioned into the Fe-Si phase [2.4]. The enrichment with B and in particular, with Nb increasingly stabilizes the residual amorphous matrix and thus hinders coarsening of grains.

The presence of Nb at the same time inhibits the formation of Fe-B compounds. The transformation finally ceases in a meta-stable two-phase microstructure of Fe-Si embedded in an amorphous Fe-Nb-B matrix.

The resulting microstructure is characterized by randomly oriented, ultrafine grains of Fe-Si (20 at%) with typical grain sizes of 10-15 nm immersed in a residual amorphous matrix which occupies about 20-30% of the volume and separates crystallites at a distance of about 1-2 nm. These features are basis for the excellent soft magnetic properties indicated by the high values of initial permeability of about 10^5 correspondingly low coercivities of less than 1 A/m.

A characteristic feature is that nanocrystalline microstructure and the accompanying soft magnetic properties are rather insensitive to the precise annealing conditions within a wide range of annealing temperature, T_a of about $\Delta T_a \approx 50-100^\circ\text{C}$. They develop in a relatively short period of time and do not much alter even after prolonged heat treatment of several hours [2.7]. Only annealing at an elevated temperatures above about 600°C leads to the precipitation of small fraction of boride compounds like Fe_2B or Fe_3B with typical dimensions of 50-100 nm, while the ultrafine grain structure of Fe-Si still persists. Further increase of annealing temperature above about 700°C , finally yields grain coarsening. Both the formation of Fe borides and grain coarsening deteriorates the soft magnetic properties significantly.

Our present composition is $(\text{Fe}_{0.8}\text{Co}_{0.2})_{73.5}\text{Cu}_1\text{Nb}_3\text{Si}_{13.5}\text{B}_9$ which possess 14.7% Co as a part of ferromagnetic transitional element. For cobalt substituted FINEMET alloy system, Mössbauer spectra and XRD results [2.8] show that $\alpha\text{-FeCo}$ is the first crystalline phase that precipitates in this alloy system. Researchers [2.9] found that addition of cobalt causes alteration of disordered DO_3 -type structure of Fe-Si grains occurred in classical nanocrystalline FINEMET, into $(\text{FeCo})\text{Si}$ solid solution of low silicon concentration. In case of Co substituted FINEMETS, it has been reported [2.10] that cobalt takes part in the main composition of nanocrystal i.e. the nanocrystalline part should be $(\text{FeCo})_3\text{Si}$.

2.5 Scope and constraints of choosing alloy compositions for achieving expected properties

It has been found in case of alloys with a small Cu-addition (of about 1 at.%) comparing to the Cu-free alloy that there are two clearly separated peaks, the first of which corresponds to the primary crystallization of b.c.c. Fe at T_{x1} and subsequently, the second to precipitation of Fe₂B compounds at T_{x2} . The separation between the two peaks is practically insensitive on the further increase of the Cu content, beyond a small, critical concentration of about 0.5 at.%. The onset temperature for the first crystalline stage is found lower than the Cu-free alloy which reflects the local clustering of Cu atoms that obviously lowers the configurational energy of the sub-critical nucleus [2.11]. Fe and the precipitation of Fe-B compounds not only is determined by Cu and Nb additions, but decreases with increasing boron content. So, it puts a constraint that boron should be kept in a low or moderate level to obtain an optimum nanoscaled structure.

Hence, the basic condition for the formation of a typical nanocrystalline structure is given by a primary crystallization process before stable or meta-stable intermetallic phases are formed. Obviously, this can be attained by (i) alloying additions which lead two clearly separated stages of crystallization at T_{x1} and T_{x2} and (ii) by annealing at $T_{x1} < T_a < T_{x2}$ such that only the phase forming at and above T_{x1} is crystallizing.

The effect of copper in enhancing the nucleation density is unique. To find a comparable effect on the crystallization behavior, Gold has been verified as the only element [2.12]. Silver, though belongs to the same noble metal group, practically is immiscible in iron even in liquid state, thus could not be verified successfully.

Although essential, Cu addition alone is not sufficient. Its effect is considerably promoted by the simultaneous presence of Nb. Nb enhances the crystallization temperatures and retards the grain growth by limiting diffusion [2.13]. In particular, the Nb-addition significantly increases separation between two crystallization stages which promotes the primary crystallization of Fe and stabilizes the residual amorphous matrix against the precipitation of Fe-B compounds. All together leads to an increased number of simultaneously growing and competing crystals resulting in the nanoscaled microstructure upon alloying at least about 2-3 at.% of Nb.

Niobium can be substituted by other group V or VI refractory elements like Cr, V, Mo, W or Ta which act similarly on the crystallization process and on the magnetic properties [2.14]. Like for Nb, the atomic volumes of these refractory elements are larger than that of Fe which reduces the diffusion coefficients and thus stabilizes the amorphous matrix and slows down the

kinetics of grain coarsening [2.15]. Accordingly the efficiency of these elements for grain size refinement increases in the order of their atomic volumes i.e. $Cr < V < Mo \approx W < Nb \approx Ta$. Thus finest grain structures and superior soft magnetic properties in practice require at least a certain amount of Nb or Ta.

The achievement of good soft magnetic properties requires an enhanced value of saturation magnetization (J_s). It demands increase of saturation magnetization of the value attained for the optimized composition $Fe_{73.5}Cu_1Nb_3Si_{13.5}B_9$, limited to about 1.2 to 1.3 T. The reason found behind lying this value within this limit is the high Si content in the b.c.c grains, which is though soluble in b.c.c Fe lattice, but in fact, not ferromagnetic and hence cannot contribute to enhance the saturation magnetization. Without Si, composition consisting of pure α -iron can cause an appreciable increase of J_s but it on the other side lacks in having good glass forming ability as Si.

So, to limit Si within a tolerable amount without risking the enhancement of J_s it needs replacement of Si for another type of element having good glass forming ability. From a study on a composition $Fe-Cu_1Nb_3Si_xB_{z-x}$ it was found that J_s increased up to about 1.6 T if B is substituted for Si. But this benefit is accompanied by a drawback that proportion of boron content beyond a particular limit favors formation of boride compounds at higher temperatures which have been proved deteriorous to soft magnetic properties. So in order to obtain a homogeneous nanocrystalline b.c.c. structure, with good soft magnetic properties, it is necessary to keep the boron content at a moderate level below about 10 at%. A low boron content yields a high crystalline fraction as well as maximizes the saturation magnetization.

However, a corresponding reduction of boron content at low Si contents, for the sake of a good glass forming ability is only possible if other good glass forming elements are added simultaneously. Such elements which extend the glass forming range at low Si and B contents are group IV to VIA transition metals [2.16]. The glass forming range is the widest for Hf containing alloys and decreases in the order of $Zr > Nb \approx Ta > Mo \approx W > V > Cr$. The most stable amorphous phase is thus obtained in alloys containing refractory metals with large atoms and low d-electron concentrations, i.e., particularly Zr, Hf, Nb and Ta. These elements at the same time are very effective in suppressing the formation of the undesired boride compounds. Accordingly, high iron content $Fe-(Cu_1)-M_{\sim 7}B_{2-9}$ alloys with $M = Hf, Zr, Nb$ and/or Ta have been found to exhibit both a more or less sufficient glass forming ability and the necessary crystallization characteristics in order to give a nanocrystalline structure with good soft magnetic properties, low magnetostriction and a high saturation induction upto 1.7 T [2.17] Nb

containing alloys are located at the border of the glass forming range [2.18] which makes them most difficult to produce in particular on larger scale. The glass forming ability is considerably improved with the addition of Zr or Hf. However, strong oxygen reactivity of either of the two elements is a severe problem and requires a good protecting casting atmosphere. Moreover, the composition with the highest saturation magnetization of $J_s = 1.6-1.7$ T, like $Fe_{91}Zr_7B_2$ are again located at the border of the glass forming range. The preparation for Fe-M-B thin ribbons by rapid solidification thus requires substantially more effort than necessary for the more conventional Fe-(Cu, Nb)-Si-B compositions and therefore, presently is still restricted to the laboratory scale.

2.6 Microstructure-Property relationship

The nanocrystalline microstructure obtained by crystallization from the amorphous state is essentially composed of two phases:

- (i) the randomly oriented grains and
- (ii) a still amorphous minority matrix. The crystalline fraction and the local atomic concentrations are determined by the original alloy composition.

In thermodynamical equilibrium, boron is practically insoluble in Fe ($\ll 0.01\text{at.}\%$); the solubilities of Cu and Nb are low: $< 0.2 \text{ at.}\% \text{ Cu}$, $< 0.1\text{at.}\% \text{ Nb}$. If these values apply to the nanocrystalline phase too, the grains essentially consist of Fe-Si which is supported by atom probe analysis.

The crystalline fraction v_{cr} is mainly determined by boron content and independent of the Si content. Both the crystalline fraction and the average grain size decreases with the increasing boron content. This indicates that boron plays a similar role as Nb in retarding grain growth. The average spacing between the crystallites δ i.e. the thickness of intergranular amorphous layer can be estimated by [2.19].

$$\delta = D (1/v_{cr}^{1/3} - 1) \approx (1 - v_{cr})/3 \dots \dots \dots (2.1)$$

and typical ranges between about 1-2 nm i.e. about 5-10 atomic layers.

The local Si content in the grains is considerably larger than the average Si content of the alloy. For the high Si content alloys, the composition of the grains is close to stoichiometric Fe_3Si which results in a DO_3 superlattice structure [2.15, 2.20] the Si content in the grains $y_{si}(\text{b.c.c.})$ can be approximately related to the average Si content x_{si} by

$$y_{\text{Si}}(\text{b.c.c.}) \approx x_{\text{Si}}/v_{\text{cr}} \dots\dots\dots(2.2)$$

which indicates that effectively all Si has partitioned into the crystallites [2.2]

$$\text{Fe-Cu-Nb-Si-B} \rightarrow v_{\text{cr}} \alpha\text{-Fe}_{1-y}\text{Si}_y + (1-v_{\text{cr}})(\text{Fe}_{1-y}\text{Si}_y)_n\text{B} + x_{\text{Cu}}\text{Cu} \dots\dots\dots (2.3)$$

where $a = n^{-1}x_{\text{Nb}}/x_{\text{B}}$ where x_{Nb} , x_{Cu} and x_{B} denote the alloy's niobium, copper and boron contents respectively.

Eq.2.3 allows estimating the composition of the intergranular amorphous phase from the data for the crystalline fraction by balance of atomic concentrations. The result of this evaluation, is a high local boron content of around 31at.% (i.e., $n \approx 2.2$) which is fairly independent of the original alloy composition. Obviously, the nucleation and growth of the grains proceeds until the residual amorphous matrix is enriched with boron such that its composition is close to stoichiometric $(\text{Fe}_{1-a}\text{Nb}_a)_2\text{B}$. The presence of Niobium hereby stabilizes the amorphous structure and impedes the formation of the corresponding crystalline boron compounds. The local Nb content is independent of the Si content and increases with decreasing average boron content. This is a consequence of the simultaneously decreasing amorphous fraction, $v_{\text{am}} = 1 - v_{\text{cr}}$ in which the available niobium is enriched. This local enrichment of niobium lastly signs responsible for the increase of the onset temperature of the second crystallization stage and the decrease of Curie temperature and the saturation magnetization of the residual amorphous matrix with decreasing average B content.

Considering addition of 14.7 % cobalt, the mean composition of the crystalline and amorphous phase may be estimated as follows [2.21]:

- i) Taking lattice parameter in the reported ternary $\text{Fe}_{3-y}\text{Co}_y\text{Si}$ as the reference data, the mean composition of the precipitated crystalline phase can be estimated.
- ii) The mean composition of the residual amorphous phase can be evaluated taking into consideration the volume crystalline fraction, v_c estimated through the area under the crystallization peaks obtained by Differential Thermal Analysis of the previously annealed sample.

Therefore, for percentage of Co, $x \sim 15$, the composition may be presented as:

$$\text{Fe}_{58.5}\text{Co}_{15}\text{Si}_{13.5}\text{B}_9\text{Cu}_1\text{Nb}_3 = v_c(\text{Fe}_{67}\text{Co}_{17}\text{Si}_{16}) + (1-v_c)(\text{Fe}_{23}\text{Co}_8\text{Si}_4\text{B}_{45}\text{Cu}_5\text{Nb}_{15})$$

The accurate determination of the microstructure, thus requires the accurate determination of volume fraction at any stage of crystallization.

3.1 Origin of magnetism

Every electron is, by its nature, a small magnet. The magnetism of solid is originated from the electrons of atoms. The circulating electron produces its own orbital magnetic moment, measured in Bohr Magnetons (μ_B), and there is also a spin magnetic moment associated with it due to the electron itself spinning, like the earth on its own axis. Although many electrons are moving by orbital motions and spin orientations around a nucleus, only two electrons with up and down spins can occupy one orbit. Therefore, most of the magnetic moments originated from spins cancel each other and does not contribute to the magnetic moment of a solid. In the case of transition elements whose d orbit is not fully occupied and rare earth elements whose f orbit is not fully occupied, magnetic moment appear due to the spin of any unpaired electron. According to Hundt's rule, electrons are occupied so that the total spin becomes maximum. In other words, the number of up-spins increases from 1 to 5 according to the atomic number, thereafter, total spin amount decreases as up-spins and down-spins cancel each other when two electrons occupy one orbit. The reason why the actual metal never has such a high of 5 Bohr magneton as the d-electrons are shared by many atoms in crystals as free electrons.

3.2 Types of magnetism

As describes above, the elements whose d-orbit or f-orbit are not fully occupied exhibit magnetic moments, but the magnetism of solids depends on how these atomic magnetic moments are aligned in crystals.

All materials can be classified in terms of their magnetic behavior falling into five categories depending on their bulk magnetic susceptibility. The two most common types of magnetism are diamagnetism and paramagnetism, which account for the magnetic properties of most of the periodic table of elements at room temperature.


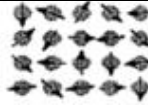
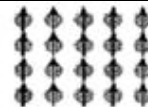
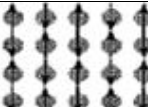
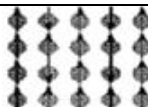
The four types of magnetism (except diamagnetism) are important in applications of magnetic materials. This is because of a quantum mechanical effect called 'Exchange interaction' that works in short distance of the order of atomic distance. In the ferromagnetic material, the exchange force cause alignment of magnetic moments in one direction, causing spontaneous magnetic moment in material.

On the other hand, if the exchange force causes antiparallel ordering of atomic spins in a crystal, the magnetic moments are cancelled in the crystal and spontaneous magnetization is lost. This type of material is called 'antiferromagnetic material'. The antiferromagnetic materials are often used to pin the magnetization of thin ferromagnetic films by the exchange coupling between a ferromagnetic/antiferromagnetic layers.

When the amount of magnetic moments of antiparallely ordered magnetic moments is different, the material exhibits spontaneous magnetization. This type of materials is called 'Ferrimagnetic materials'. This is the type of magnetism not observed in any pure elements, but only in compounds such as mixed oxides, known as Ferrites, from which 'Ferrimagnetism' derives its name.

Most materials do not have any order of magnetic moment, in which case the orientation of atomic magnetic moments are random, thus no spontaneous magnetization appear. These are called 'Paramagnetism', which show only small magnetization when magnetic field is applied due to the orientation of atomic magnetic moments. So the susceptibility of paramagnetic materials is orders of magnitude smaller than those for Ferromagnets and Ferrimagnets. Since most of materials show paramagnetism, the materials that can be used in magnetic engineering are pretty limited. Since magnetic order is disturbed by thermal agitation, ferromagnets, antiferromagnets and ferrimagnets lose their magnetic order at high temperature identified as the magnetic transition temperature. For ferromagnets, this transition temperature is called 'Curie temperature' and for antiferromagnets, it is mentioned as 'Neél temperature'. When the size of ferromagnetic particles becomes smaller than a few nanometer, the magnetic moments are thermally fluctuated and they become paramagnetic even at room temperature. This state is called 'Superparamagnetism'.

Table: 3.1. Summary of different types of magnetic behavior

Type of Magnetism	Susceptibility	Atomic/Magnetic Behavior	Example/ Susceptibility
Diamagnetism	Small (+)	Atoms have no magnetic moment 	Au -2.74×10^{-6} Cu -0.77×10^{-6}
Paramagnetism	Small (-)	Atoms have randomly oriented magnetic moment 	β -Sn 0.1910^{-6} Pt 21.0410^{-6} Mn 66.1010^{-6}
Ferromagnetism	Large (+) function of applied field, microstructure dependent	Atoms have parallel aligned magnetic moment 	Fe $\sim 100,000$
Anti ferromagnetism	Small (+)	Atoms have mixed parallel and antiparallel aligned magnetic moment 	Cr 3.610^{-6}
Ferri magnetism	Large (+) function of applied field, microstructure dependent	Atoms have antiparallel aligned magnetic moment 	Ba ferrite ~ 3

3.3. Exchange interaction and Ferromagnetic ordering:

The basic criteria for the onset of magnetic order in solids are (i) individual atoms should have magnetic moments (spins) and (ii) exchange interactions must exist between the atoms that couple them together.

Ferromagnetism is supposed to arise from interactions between neighbouring atomic moments, which make them to align parallel. In 1928, Heisenberg, described the quantum mechanical origin of ferromagnetism by considering the interaction between the electronic spins. The spins of the neighbouring electrons are coupled and in this way all the spins are oriented in the same direction. This parallel alignment of the spins gives rise to a macroscopic magnetic moment. The coupling can be expressed as shown in equation (3.1)

As proposed by Heisenberg, a system is characterized by its energy in order to describe the magnetic configuration of a system according to the following Hamiltonian:

$$H_j = -\sum_{i,j} J_{i,j} \sigma_i \sigma_j \dots\dots\dots(3.1)$$

where J_{ij} is the exchange-coupling constant between the spins \mathbf{S}_i and \mathbf{S}_j distributed on a regular lattice. Only nearest neighbours are included in the summation. The magnetic property of a system is thus dependent on the sign and strength of the interaction between the spins. If $J_{i,i+1} = J > 0$, parallel orientation of the spin is favored and at low temperatures all spins will be aligned ferromagnetically. At high temperatures the entropy dominates the interaction energy and the spins will fluctuate independently with the manifestation of paramagnetic phase, while at lower temperatures the interaction energy dominates and the system will order at the critical temperature (T_c), with all the spins pointing in the same direction with the appearance of ferromagnetic phase.

For if $J_{i,i+1} = J < 0$, the low temperature phase is antiferromagnetic with the spins aligned antiparallel to their neighbours below a characteristic temperature T_N , called the Néel temperature. Above T_N , the material exhibit paramagnetic behavior. In the simplest case, the lattice of an antiferromagnet is divided into two sublattices with the magnetic moments of these in antiparallel alignment. This gives rise to zero net magnetization. A special case of antiferromagnetism is ferrimagnetism. In ferrimagnetism, there are also two sublattices with magnetic moments in opposite directions, but the magnetization of the sublattices are of unequal strength resulting in a non-zero magnetization. At the microscopic level of domain structures, ferromagnetic and ferrimagnetic materials are therefore similar. The Curie and Néel temperature characterizes a phase transition between the magnetically ordered and disordered (paramagnetic) states.

If $J_{i,i+1} = J = 0$, the Hamiltonian describes a system being paramagnetic at all temperatures with all the spins pointed at random resulting in zero magnetic moment. Besides these common types of magnetic ordering, various other types of magnetic structures such as canted, helical and conical spin arrangements may exist.

3.4 Theories of Ferromagnetism

Ferromagnetism is a collective phenomenon since individual atomic moments interact so as to promote alignment with one another. This collective interaction gives rise to the temperature dependence of the magnetization. Two models have explained the interaction between atomic moments. Mean Field Theory considers the existence of a non-local internal magnetic field, called the Weiss field, which acts to align magnetic dipole moments even in the absence of an applied field H_a . Heisenberg Exchange Theory considers a local (usually nearest neighbour)

interaction between atomic moments (spins) which acts to align adjacent moments even in the absence of a field.

The basic assumption of the mean field theory is that this internal field is non-local and is directly proportional to the sample magnetization, $H_{INT} = \lambda_W \mathbf{M}$, where the constant of proportionality λ_W is called the Weiss molecular field constant. To consider ferromagnetic response in applied field \mathbf{H}_a as well as the randomizing effects of temperature, we consider the superposition of the applied and internal magnetic fields. By analogy with the problem of paramagnetic moments, the average atomic dipole moment can be expressed in terms of the Brillouin function $\langle \mu_m \rangle = \mu_B g J B_J(a')$, where $a' = \frac{g \mu_B (H + \lambda_W M)}{k_B T}$ for a collection of classical dipole moments. Similarly, the saturation magnetization, $M_s = N_m \langle \mu_B g J \rangle$ and:

$$\frac{1}{1 - \lambda_W M} = \frac{1}{1 - \lambda_W M} = B_J \{ H + \lambda_W M \} \dots \dots \dots (3.2)$$

Under appropriate conditions, this leads to solutions for which there is a non-zero magnetization (spontaneous magnetization) even in the absence of an applied field.

For $T > T_c$, the ferromagnetic Curie temperature the only solution to Eq. (3.2) is $M = 0$ i.e. no spontaneous magnetization and thus paramagnetic response. For $T < T_c$, we obtain solution with a non-zero, spontaneous magnetization, the defining feature of a ferromagnet.

The Heisenberg model considers ferromagnetism and the defining spontaneous magnetization to result from the nearest neighbor exchange interactions, which act to align spins in a parallel configuration, instead of a non-local, mean field. Let us consider first the Heisenberg ferromagnet. Here we assume the atomic moments (due to a spin vector \mathbf{S}) on nearest neighbor sites are coupled by a nearest neighbor exchange interaction that gives rise to a potential energy:

$$E_p = -J_{11} \mathbf{S}_i \times \mathbf{S}_{i+1} \dots \dots \dots (3.3)$$

that for $J_{11} > 0$ favors parallel alignment of the spins. The exchange energy, suitably scaled, replaces the Weiss molecular field constant in the mean field theory of ferromagnetism to explain the temperature dependence of magnetization.

An empirical description of the variations of the exchange energy with interatomic spacing called the Bethe-Slater curve is instructive in describing the effect of alloying on ferromagnetic Curie temperatures. In 3D transition metal solids, the Bethe-Slater curve, shown in Fig.3.1.(a) predicts the sign of the exchange interaction. The interplay between electron-electron Coulomb interactions and the constraints of the Pauli Exclusion Principle determine the sign of exchange interaction. In transition metal solids a measure of the overlap between nearest neighbor d-orbitals is given by the ratio of the atomic to the 3d ionic (or nearest neighbor) radius.

In the amorphous phase structural fluctuations give rise to fluctuations in the exchange interactions. A first order theory as to the fluctuation in the exchange interactions with fluctuation in interatomic spacing can be offered by considering a Taylor's series expansion of the exchange interaction as a function of nearest neighbor spacing of the form:

$$J_{11} = J_{11}^1 + \left(\frac{1}{J_{11}^1}\right)_{11} \Delta X \dots \dots \dots (3.4)$$

It can be readily seen that alloys which have exchange energies, J_{11}^1 which lie near the peak in the Bethe-Slater Curve Fig.3.1.(b) (e.g. Co, FeCo) will be insensitive to fluctuations in the interatomic spacing since $\frac{1}{J_{11}^1} \sim 0$. It should be noted that alloy addition will reduce magnetic coordination numbers should shift J_{11}^1 to the left of the elemental values.

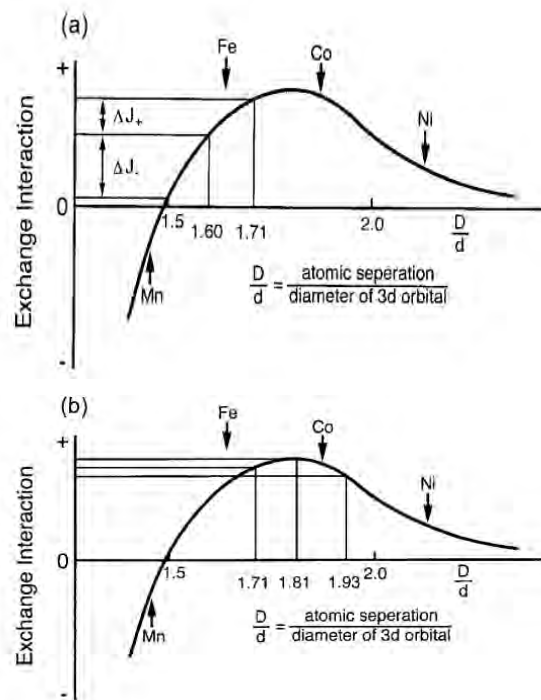


Fig.3.1 Bethe-Slater curve for the magnetic exchange interaction energy as a function of interatomic spacing (normalized by spatial extent of the magnetic 3d orbitals). Also showing large variations of J with position on the left of the curve [3.1]

3.5 Ferromagnetic domains:

In a ferromagnet, there are macroscopic volumes, called magnetic domains, over which atomic magnetic moments are aligned due to the internal (Weiss) field or alternatively the ferromagnetic exchange interaction. The direction of magnetic moments in a single domain shows the direction of magnetization of that domain. Thus, each of these domains has a spontaneous magnetization of magnitude M_s . The magnitude of magnetization in all domains may be same but the direction varies from one domain to the other. So, in the demagnetized state, ferromagnets show no net magnetization [Fig.3.2].

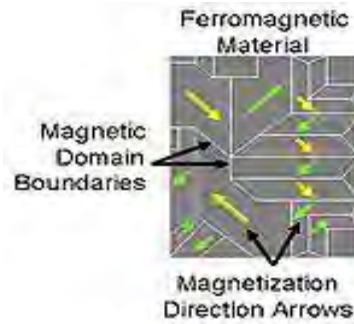


Fig.3.2 Magnetic domains in a ferromagnetic material in the demagnetized state.

As mentioned above, in the absence of an aligning field the magnetization vectors are aligned differently from domain to domain. Thus if we take the vector average of the magnetization over many domains we arrive at zero sample magnetization, $\langle M \rangle = 0$, because of vector cancellation of the random domain moments.

Having more than one domain requires an interfacial region between domains called a domain wall. Associated with this interface is positive domain wall energy. The directions of the magnetic moments are not changed suddenly from one domain to another but rotate gradually within the domain walls [Fig.3.3]. In soft materials, which have been optimized to have very low rotational energy barriers, the major determinant of the shape of magnetization curve is domain wall motion.

We will find it useful to describe several length scales that are associated with the domains and domain walls. These are expressed through consideration of domain wall energies. The energy per unit area in the wall can be expressed as a sum of exchange and anisotropy energy terms:

$$\gamma_{\text{wall}} = \gamma_{\text{ex}} + \gamma_{\text{k}} \dots \dots \dots (3.5)$$

where the anisotropy per unit volume K is multiplied by volume contained in a domain wall, $A_w \delta_w$ and divided by cross-sectional area to arrive at an anisotropy energy per unit area:

$$\gamma_k = K \frac{1 \ 1 \ 1 \ 1}{1} = K \delta_w = K(N_p a) \dots\dots\dots(3.6)$$

Where $\delta_w = N_p a$ (a is the lattice constant in the direction of rotation and N_p is the number of planes over which the rotation takes place) is the thickness of the wall.

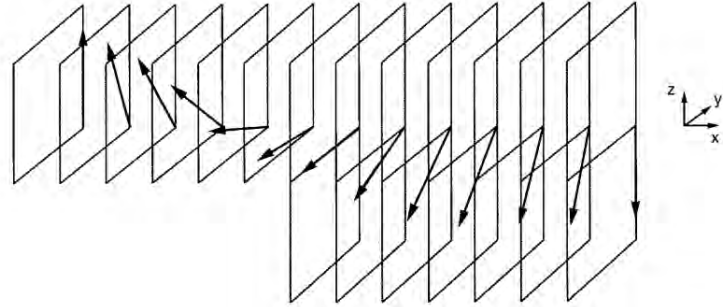


Fig.3.3 Rotation of atomic magnetic dipole moments in a 180° (Bloch) domain wall in a ferromagnetic material.

Thus γ_{wall} can be expressed:

$$\gamma_{wall} = \frac{1 \ 1 \ 1 \ 1}{1} + K_1(N_p a) \dots\dots\dots(3.7)$$

where the first term considers the cost in exchange energy in rotating magnetic dipole moments in a 180° domain wall as illustrated in the above fig.3.3. To determine the optimal wall thickness we differentiate γ_w with respect to δ_w

$$\frac{1}{1} \frac{1 \ 1 \ 1 \ 1}{1 \ 1 \ 1} = 0 = - \frac{1 \ 1 \ 1 \ 1}{1 \ 1 \ 1} + K_1 \dots\dots\dots(3.8)$$

yielding:

$$N_{eq} = 1 \frac{1 \ 1 \ 1 \ 1}{1 \ 1 \ 1} \dots\dots\dots(3.9)$$

For Fe, $N_{eq} \sim 300$ and the equilibrium thickness, $t_{eq} = N_{eq} a \sim 50$ nm. Expressed in terms of the exchange stiffness A_{ex} , the domain wall width δ_w is:

$$\delta_w = \pi \frac{1 \ 1 \ 1}{1} \dots\dots\dots(3.10)$$

Another important length scale is the distance over which the perturbations due to the switching of a single spin decays in a soft material. This length is called the ferromagnetic exchange length (L_{ex}) and can be expressed:

$$L_{ex} = 1 \frac{1 \ 1 \ 1}{1 \ 1 \ 1} \dots\dots\dots(3.11)$$

The ferromagnetic exchange length is $\sim 3\text{nm}$ for ferromagnetic iron or cobalt based alloys. The ratio of exchange length to (δ_w/π) is a dimensionless parameter κ , called the magnetic hardness parameter:

$$\kappa = \frac{1}{\delta_w} \sqrt{\frac{2A}{K_1}} \dots \dots \dots (3.12)$$

For hard magnetic materials κ is in the order of unity and thus there is little difference between the ferromagnetic exchange length and the domain wall width. On the other hand, for good soft magnetic materials, where K_1 approaches zero, can deviate substantially from unity.

Structure sensitive magnetic properties may depend on defect concentration (point, line and planar defects), atomic order, impurities, second phases, thermal history, etc. In multi-domain materials, the domain wall energy density,

$$\gamma = 4(AK_1)^{1/2} = \gamma(x) \dots \dots \dots (3.13)$$

is spatially varying as a result of local variations in properties due to chemical variations, defects etc. A domain wall will prefer to locate itself in regions where the magnetic order parameter is suppressed i.e. pinning sites. Since changes in induction in high permeability materials occur by domain wall motion, it is desirable to limit variation of $\gamma(x)$ (pinning). This is one of the key design issues in developing soft magnetic materials i.e. that of process control of microstructure so as to optimize the soft magnetic properties.

3.6.1 Amorphous Alloy or Metallic Glass:

In condense matter physics, an **amorphous** (from the Greek *a*, without, *morphé*, shape, form) or **non-crystalline solid** is a solid that lacks the long-range order characteristic of a crystal.

In part of the older literature, the term has been used synonymously with glass. The local structure in amorphous metallic material is distinct from that of window glass. By analogy, the term ‘metallic glass’ usually refers to a metallic alloy rapidly quenched in order to “freeze” its structure from the liquid state.

A ‘glass’ refers to a molten mass that is cooled rapidly to prevent crystallization. The expression ‘glass’ in its original sense refers to an amorphous or nanocrystalline solid formed by continuous cooling of a liquid while a solid is defined somewhat arbitrary as object having a viscosity greater than 10^{14} Pa.s [3.2]. Glasses have been found in every category of materials and of various bond types: covalent, ionic, Vander Walls, hydrogen and metallic. Different types of amorphous solids include gels, thin films and nanostructured materials.

3.6.2 Theoretical understanding of amorphous alloy:

The atoms in an amorphous solid are not periodically arranged and therefore the concept of a lattice is not appropriate for describing their positions. Thus in an amorphous solid there is not an equivalent concept to that of a lattice and a basis we must try to concentrate into describing atomic positions in a more probabilistic sense using the concept of a **Pair Distribution Function $g(r)$** .

The pair correlation function is defined as the probability that two atoms in the structure are separated by a distance r . To define $g(r)$ further begin by considering N atoms in a volume Ω , lettering $R_1, R_2, R_3, \dots, R_N$ denote the positions of N atoms with respect to an arbitrary origin. The distance r denotes the magnitude of vector connecting two atoms i and j ,

$$\text{i.e., } r = R_i - R_j \dots \dots \dots (3.14)$$

Two additional atomic distribution functions related to the pair correlation function are the spatially dependent atomic density $\rho(r)$ which is defined as:

$$\rho(r) = Ng(r)/\Omega \dots \dots \dots (3.15)$$

and the radial distribution function RDF(r) which is defined in terms of the pair correlation function as:

$$\text{RDF}(r) = 4\pi r^2 \rho(r) \dots \dots \dots (3.16)$$

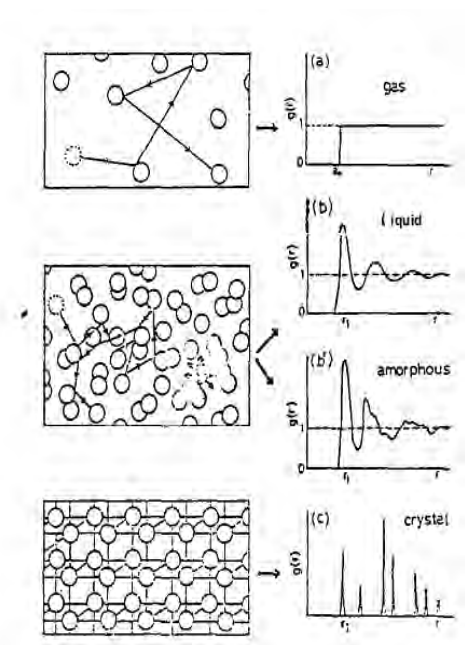


Fig.3.4 Schematic sketches of the atomic configuration and its pair distribution function $g(r)$ in a gas, liquid, glass and crystal.

Fig.3.4 illustrates schematically the distinction between the pair correlation functions for a gas, liquid, glass and crystal. In the gaseous state, the states is distributed randomly and are totally uncorrelated. However, the atom do not mutually approach within the atomic diameter a . Thus being a completely disordered material, a gas has a uniform unit probability of finding neighboring atoms at all possible distances which leads to a uniform, featureless $g(r)$.

In both the liquid and glassy states, the atoms are randomly distributed in a nearly close-packed structure. There exists a high degree of local correlation. The atomic configuration in the glassy state has more rigid packing compared with that of the liquid state. The essential aspect with which the amorphous solid structure differs with respect to that of crystalline solid is the absence of long range order. There is no translational periodicity.

A crystalline solid has a set of discrete distances between atomic positions and therefore the pair correlation function in a set of discrete δ -like functions, the amplitude of which reflects the particular coordination number for nearest neighbor, next nearest neighbor,.....etc. pair of atoms. This is consistent with Bragg scattering (diffraction). In amorphous alloys, $g(r)$ is neither discrete nor featureless; instead broad peaks reflect the short-range order in these materials.

3.6.3 Synthesization of amorphous alloys

Amorphous states of pure metals like Fe, Co, Ni etc. can be obtained only at a very low temperature. Alloys of these metals with glass forming materials can be obtained in the amorphous state by cooling the melt at a relatively lower rate of million degrees per second which can remain in the metastable state over an extended range of temperature.

Synthesizing amorphous alloys requires rapid solidification, in order to bypass the crystallization [3.3]. The metastable structure thus achieved nevertheless may possess a short range order (SRO) that resembles the equilibrium crystal structure [3.4].

Fig.3.5 presents the Temperature-Time-Transformation (TTT) diagram that shows a characteristic C curve behavior indicating the time taken for a small amount of crystalline phase to form in an under cooled liquid as a function of temperature. At the temperature close to melting point T_m , there is little driving force for crystallization, so that the crystal nucleation and growth rates are small, and the crystallization onset time t_0 is large. As the temperature decreases, the crystallization onset time reaches a minimum value t_1^* at a temperature T_n , and then increases again as a thermal energy becomes insufficient for atomic motion.

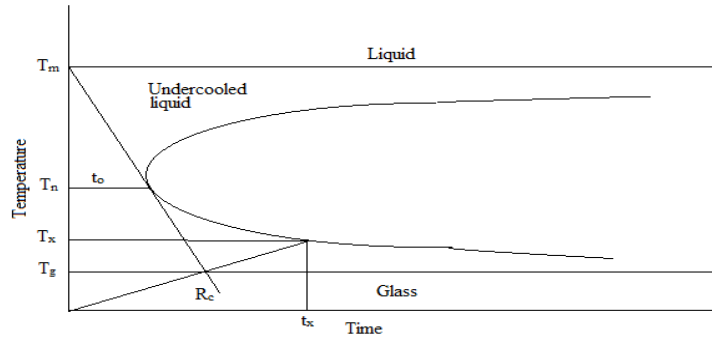


Fig.3.5 Schematic TTT diagram for the onset of crystallization.

The atomic motion is completely suppressed when temperature approaches close to the glass transition temperature (T_g), the point at which the amorphous structure is frozen in, so that the crystallization onset time t_0 , becomes large. Therefore, critical cooling rate R_c to avoid crystallization is given below:

$$R_c = \frac{1_1 - 1_1^*}{1_1^*} \dots\dots\dots(3.17)$$

3.6.4 The liquid-glass transition:

Mechanical hardness of condensed matter is dependent on the viscosity such that although amorphous materials structurally resembles a liquid state, their viscosity become comparable to that of a solid and this determines the stability of amorphous materials.

To illustrate the liquid-glass transition, Fig.3.6 presents an example that shows schematically the viscosity η and the time constant for structural relaxation τ of a $Pd_{77}Cu_6Si_{17}$ glass forming alloy. The solid lines represents the experimental data. In this figure, the logarithms of η and τ are plotted against the inverse of the reduced temperature T_m/T . Here τ is the average time required for atomic rearrangement and is related approximately to the shear modulus μ and viscosity η of a liquid by $\tau = \eta/\mu$ with $\mu = 10^{11}$ dynes cm^{-2} for liquid metals.

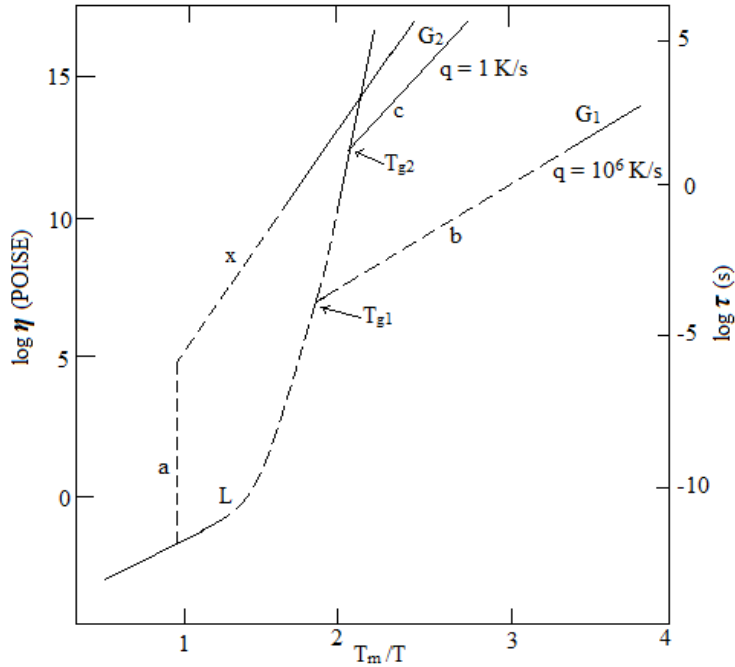


Fig.3.6 Viscosity $q(T)$ and constant $\tau(T)$ for structural relaxation in a PdCuSi alloy.

As shown in Fig.3.6, when a melt is cooled very slowly, the formation of crystal occurs at T_m and the viscosity is drastically increased as shown in curve (a). This corresponds to the viscosity of a melt in the internal equilibrium [3.5]. Actually, metastable equilibrium can no longer be reached on the experimental time scale since the molecular rearrangements required to obtain this state take an increasing amount of time with decreasing temperature below a certain temperature T_g . The nonequilibrium system is called an “amorphous” and T_g is the amorphous transition temperature. Conveniently, T_g is chosen as the temperature at which the metastable equilibrium viscosity has the value of 10^4 P which corresponds to a time constant τ of about one hour. Lines (b) and (c) show the temperature dependence of viscosity of the amorphous in a particular non-equilibrium configuration and are therefore designated as “isoconfigurational” lines. The state corresponding to (c) can be obtained either by cooling more slowly than for (b), thus allowing more time for equilibrium, or by so-called “structural relaxation” of state (b) towards its metastable equilibrium.

The temperature dependence of the viscosity is given by the Vogel-Fulcher law [3.6]:

$$\eta(T) = \eta_0 \exp\left(\frac{1}{1 - T/T_0}\right) \dots \dots \dots (3.18)$$

Here, T_0 is known as the ideal glass transition temperature, the constant B is a small fraction of the chemical bonding energy in the structure. In simple liquids, such as liquid metals or

organic metals, B is small and represents a substantial fraction of T_m . In network forming liquids, b values are of the order of chemical bonding energy and T_0 is low. Most interpretations of Eq.3.18 have in common concept that the flow process requires a cooperative motion involving a group of atoms.

In summary, a glass shows three characteristics upon heating: structural relaxation, the glass-liquid transition, and crystallization. Structural relaxation occurs whenever the glass attains acceptable mobilities such that $\tau_g(T, q \text{ etc.}) \approx t_{mea}$. The rate of structural relaxation critically depend on previous thermal history. Glasses produced in high quenching rates or subjected to cold-rolling or irradiation process exhibit a highly disordered structure and high atomic mobilities, and thus undergo structural relaxation readily at lower temperatures. Annealing drastically lower relaxation processes. On the other hand, the glass transition takes place when the time constant for structural relaxation of the relaxed glass $\tau_1(T)$, approaches $t_{mea} \propto q^{-1}$. The observed glass transition temperature T_g , thus, is determined by the heating rates employed in measurement and is less susceptible to previous heat treatment.

3.6.5 Factors contributing to glass formation and stability:

There are three interrelated factors that determine glass forming tendency. These are:

1. Thermodynamic conditions that favour the liquid phase relative to crystalline phase,
2. The kinetic conditions that inhibit crystallization and
3. The process factors that arise due to the experimental conditions.

The thermodynamic factors for glass formation are liquidus temperature (T_m) at which the alloy melts, the heat of vaporization and the free energy of all phases that arise or could potentially arise during solidification process. Viscosity of the melt, the glass transition temperature (T_g) and the homogeneous nucleation rate belong to kinetic parameters.

Processing parameters are the cooling rate, the heterogeneous nucleation rate and the supercooling temperature interval. The temperature of the glass transition is slightly dependent on the cooling rate. At each cooling rate, the glass will freeze in a different state of internal energy.

A single parameter that expresses glass forming tendency is the ratio of the glass transition temperature to the melting temperature defined as

$$T = \frac{T_g}{T_m} \dots\dots\dots(3.19)$$

which usually is mentioned as reduced glass transition temperature or reduced temperature.

Higher values of τ obviously favor glass formation. For metallic glass to be formed by rapid cooling τ should be greater than 0.45 as mentioned by H. S. Chen [3.7]. Based on alloy composition, there are two major groups that rapidly form glasses. In one of these groups the metal is from Fe, Co, Ni, Pd or Pt and the metalloid is B, C, Si, Ge or P. These metallic glasses constitute soft amorphous magnetic materials.

It is very difficult to get pure metals in the amorphous state. It is necessary to add glass forming materials to pure metals or alloys to get amorphous state and to bring cooling rate within a reasonable rate. Usually around 20% of glass forming materials like B, Si, P, C etc. which have atomic radii comparatively small compared to those of metallic atoms occupy the voids left between the bigger atoms of metals when they are closely packed. It can be showed that when there is random close packing of hard spheres, there is about 20% voids created between these atoms. The glass forming material also reduces the melting point of the alloys and thereby the separation between the glass forming temperature and the crystallization temperature is reduced.

The amorphous alloy composition most favorable for glass formation is near eutectic, i.e. the composition in which the transformation from the liquid state to solid state take place instantaneously without passing through liquid plus solid mixed phase. The deeper the eutectic, the better is the glass formation ability [3.8].

The magnitude of T_g and T_x are very different for amorphous materials and depend strongly on composition. The activation energy ranges typically between 2 and 6 eV [3.9].

The crystallization is associated with nucleation and growth process. Since the formation of an amorphous alloy depends on the absence of long-range order, change of composition is expected to affect T_g and T_x . This is because the long range ordering of atoms depends on the free energy difference between the crystallite state and the amorphous state.

3.7 Differential Thermal Analysis and its application:

Differential Thermal Analysis (DTA) is a technique to study the structural change occurring both in solid and liquid materials under heat treatment.

During this process, the temperature difference between a substance and a reference material is measured as a function of temperature whilst the subject and the reference material is subjected to same controlled temperature program.

The transition of an amorphous or glassy state to crystalline state is accompanied by an exothermic heat effect that gives rise to a sharp peak in temperature dependence of the heat

flow. To study this thermally induced transformations in amorphous alloys, Differential Thermal Analysis (DTA) is a widely used technique.

DTA detects the release or absorption of heat which is associated with the chemical and physical changes in materials as they are heated or cooled. Such information is essential for understanding thermal properties of materials. Analysis of decomposition of glass materials, crystalline phase changes, chemical reactions and glass transition temperature are some of the properties measured with DTA.

Amorphous alloys are in a metastable state and tend to transform in to stable crystalline phases. At temperatures below the crystallization temperature, structural relaxation effects take place which are caused by atomic rearrangements.

From the thermodynamic viewpoint [3.10-3.11], the ability of an alloy to be quenched into the glassy state is generally measured by the magnitude of quantity,

$$\Delta T_g = T_m - T_g \dots\dots\dots(3.20)$$

where T_m and T_g are the melting and glass transition temperature respectively. In a similar manner the stability of glass after formation is generally measured by the magnitude of the quantity,

$$\Delta T_x = T_x - T_g \dots\dots\dots(3.21)$$

where T_x is the temperature for the onset of crystallization. The crystallization temperature T_x is defined as the temperature at which crystallization occurs with long-range atomic ordering.

The crystallization is associated with the nucleation and growth process. Since the formation of an amorphous alloy depends on the absence of long-range atomic order, change of composition is expected to affect T_g and T_x . This is because long-range ordering of atoms depends on the free energy difference between the crystalline state and the amorphous state. The magnitude of T_g and T_x are very different for amorphous materials and depend strongly on composition. Using DTA technique it is possible to determine T_g and T_x .

Evaluation of activation energy based on DTA technique:

Based on the work of Murray and White [3.12, 3.13, 3.14] the kinetics of crystallization of materials can be understood by interpretation of DTA patterns of the materials.

The dependence of T_x on heating rate $\beta=dT/dt$ can be used to determine the activation energy of crystallization [3.15]. Considering the fraction x of amorphous material transformed into crystalline state in time t and at a constant temperature T , one obtains for the first order process [3.16, 3.17],

$$\left(\frac{1}{1}\right)_1 = 1_1 (1-x) \dots \dots \dots (3.22)$$

The magnitude of rate constant is determined by the temperature and is given by the Arrhenius equation

$$1_1 = 1_1 \exp\left(-\frac{E}{RT}\right) \dots \dots \dots (3.23)$$

Here, R is the gas constant T is the Kelvin temperature A and E are the constants that are properties of the material. The constant E called activation energy is often interpreted as the energy barrier opposing the reaction. The constant A most often called the frequency factor is a measure of the probability that amolecule having energy E will participate in a reaction.

When the temperature is changing with time the reaction rate is:

$$\frac{1}{1} = \left(\frac{1}{1}\right)_1 + \left(\frac{1}{1}\right)_1 \frac{1}{1} \dots \dots \dots (3.24)$$

The rate of change of x with temperature with the time coordinate fixed ($1/1$) is zero because fixing the time also fixes the number and position of the particles constituting the system. The only effect of an instantaneous change in temperature is in the velocity of the thermal motion of the particles. The total rate of reaction may then be expressed

$$\frac{1}{1} = A(1-x) \exp\left(-\frac{E}{RT}\right) \dots \dots \dots (3.25)$$

This expression holds for any value of T, whether constant or variable so long as x and T are measured at the same instant.

When the reaction rate is maximum its derivative with respect to time is zero.

Solving eq.(3.25) for $(1/1)$ ($1/1$):

$$\frac{1}{1} \left(\frac{1}{1}\right) = \frac{1}{1} \left(\frac{1}{1} \frac{1}{1} - 1_1 \frac{1}{1}\right) \dots \dots \dots (3.26)$$

The maximum value of $1/1$ occurs at temperature 1_1 defined by

$$1_1 \frac{1}{1} = \left(\frac{1}{1}\right)_{1_1} \dots \dots \dots (3.27)$$

From eq.(3.27) it is easily seen that

$$\frac{1 \left(\frac{1}{1_1}\right)}{1 \left(\frac{1}{1_1}\right)} = -\frac{1}{1} \dots \dots \dots (3.28)$$

Here $1 = \frac{1}{1}$ the heating rate.

From the measured data of the heating rate (1) and the respective crystallization temperature (1_1), the activation energy E can be deduced from the slope of a plot of $1 \frac{1}{1_1}$ versus $\frac{1}{1_1}$.

In the present investigation, activation energy was calculated and results are presented in chapter 5.

3.8 Theory of X-ray diffraction:

Nanocrystalline alloys, because of their crystallinity exhibit Bragg scattering peaks in X-ray diffraction experiments. However, due to their small size, significant fine particle broadening is observed in the Bragg peaks. The condition for constructive reinforcement of X-ray scattering from a crystalline solid is given by Bragg's law:

$$n\lambda = 2d\sin\theta \dots \dots \dots (3.29)$$

This equates the path difference of X-rays scattered from parallel crystalline planes spaced $d=d_{hkl}$ apart to an integral (n) number of X-ray wavelengths λ . Here, θ is the X-ray angle of incidence (and of diffraction) measured with respect to the crystalline planes. For an infinite crystal Bragg scattering occurs at discrete values of 2θ satisfying the Bragg condition i.e., Bragg peaks are δ -functions. For finite sized crystals (Fig.3.7) the peaks are broadened over a range of angles.

To better understand the phenomenon of fine particle broadening [3.18], we consider a finite crystal of thickness $t=md$ where m is an integer and d is the distance between the crystalline peaks i. e., there are m planes in t . Considering Fig.3.7 if the broadened Bragg peak begins at an angle $2\theta_2$ and $2\theta_1$ the breadth of the peak (or full width at half maximum) is given as:

$$B_{\theta} = \frac{1}{1} (2\theta_1 - 2\theta_2) = \theta_1 - \theta_2 \dots \dots \dots (3.30)$$

Now consider the path differences for each of two angles θ_1 & θ_2 for X-rays travelling the full thickness of the crystal:

$$(m+1)\lambda = 2t\sin \theta_1 \dots \dots \dots (3.31)$$

$$(m-1)\lambda = 2t\sin \theta_2 \dots \dots \dots (3.32)$$

and by subtraction:

$$t(\sin \theta_1 - \sin \theta_2) = \lambda$$

$$= 2t\cos\left(\frac{\theta_1 + \theta_2}{2}\right)\sin\left(\frac{\theta_1 - \theta_2}{2}\right) \dots \dots \dots (3.33)$$

Now, $\theta_1 + \theta_2 \sim 2\theta_B$ and $\sin (\theta_1 - \theta_2)/2 \sim (\theta_1 - \theta_2)/2$ so that

$$T = \frac{1}{1 \ 1 \ 1 \ 1 \ 1 \ 1} \dots \dots \dots (3.34)$$

A more exact empirical treatment yields:

$$T = \frac{1 \cdot 1 \cdot 1}{1 \ 1 \ 1 \ 1 \ 1 \ 1} \dots \dots \dots (3.35)$$

Which is known as Scherrer formula. It states that for a crystal of thickness t , we should expect a particle broadening of B of the Bragg peak at $2\theta_B$.

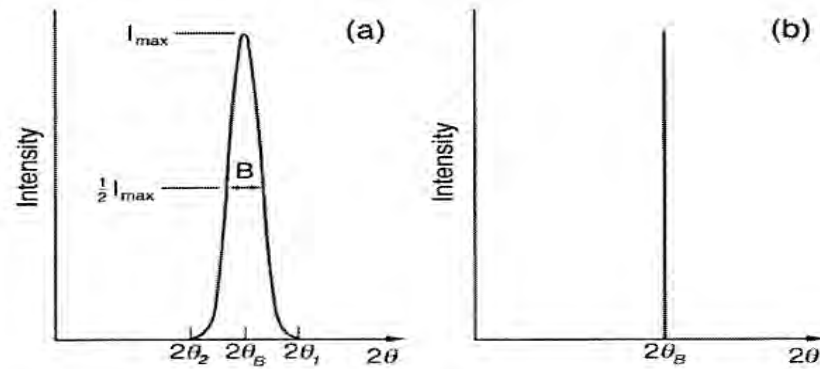


Fig.3.7 Illustration of the effect of fine particle broadening in XRD (a) fine particles and (b) perfect crystal. [adapted from Cullity] [3.18].

3.9 The fast cooling of the melt:

Amorphous metallic alloys are synthesized by rapid solidification processing techniques in alloy systems where the liquid phase remains stable to low temperature and there are competing crystalline phases below the liquidus i.e. alloys can be produced by a variety of rapid solidification processing routes including splat quenching, melt spinning, gas atomization and condensation from the gas phase. These typically require cooling rates of greater than 10^4K/s for binary alloys at a eutectic composition. Among the most common rapid solidification processing technique is melt spinning which yields amorphous metallic ribbons typically $20\mu\text{m}$ in thickness and gas atomization techniques that yield several μm to submicron powders the smallest of which can be made amorphous. The melt temperature influences the ribbon thickness and therefore the final nanocrystal size distribution throughout the transformed ribbon after nanocrystallization.

Malassaki [3.19] has discussed the thermodynamic and kinetic considerations for the synthesis of amorphous metallic phases. Glass forming ability (GFA) involves suppressing crystallization by preventing nucleation and growth of the stable crystalline phase so as to maintain a metastable quenched liquid phase. Glass forming ability can be correlated with the reduced glass forming temperature T_{rg} , which is defined as $T_{rg} = (T_L - T_G)/T_L$, where T_L and T_g are liquidus and glass transition temperatures respectively.

Five criteria have been enumerated for promoting the partitionless (i.e.) with no composition change freezing of a liquid to form a metallic glass. These are:

1. *Quenching to below T_0 curve*: The so called T_0 curve represents the temperature below which there is no thermodynamic driving force for partitioning and the liquid freezes into a solid of the same composition.
2. *Morphological ability* depends on the comparison of imposed heat flow and the velocity of the interface between the amorphous solid and the liquid phase.
3. *Heat flow*: The supercooling of the liquid phase must exceed L/C where L is the latent heat of solidification and C is the specific heat of the liquid, so as to prevent segregation.
4. *Kinetic criteria*: A critical cooling rate R_c , for quenching the liquid phase is empirically known to depend intimately on the reduced glass forming temperature T_{rg} .
5. *Structural*: Different atomic size ratios typically with difference exceeding ~13% are desired to retard the diffusional motion necessary for partitioning.

3.10 Primary Crystallization:

One of the main routes to obtain nanostructured materials is the primary crystallization of metallic glasses. In such transformations, crystallites with a different composition than amorphous precursors grow with a diffusion controlled regime. FINEMET alloys with nanocrystalline state are produced from its amorphous precursor through primary crystallization reaction. For an easy understanding of the mechanism of primary crystallization one can consider the schematic free energy diagram (Fig.3.8) for a binary alloy system.

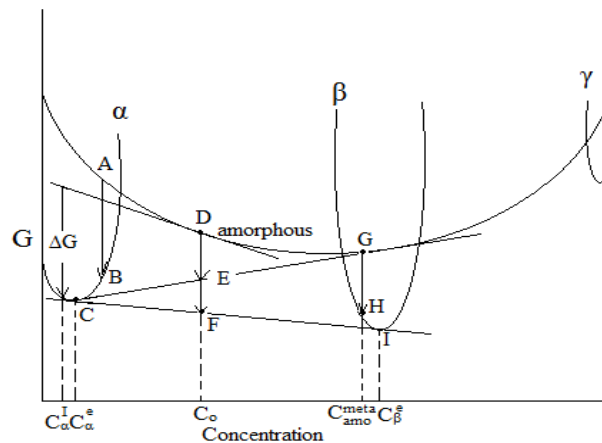


Fig.3.8 Schematic free energy concentration diagram of a model amorphous binary alloy system.

When an amorphous phase with composition 'A' is annealed, crystallization occurs without any change in concentration (A→B) then this type of crystallization is called Polymorphous Crystallization. In this type the crystal can grow only with atom transfer of a few atomic distances across the interface, like a massive transformation. Hence in general, coarse grain size microstructures can be obtained by this process. In the final stage, the supersaturated α phase decompose to achieve thermal equilibrium (B→C) composed of α and β phase (shown by tangent CI).

When the amorphous phase D is crystallized, then the α phase precipitates from the matrix of amorphous phase with composition D. The chemical driving forces for nucleation ΔG is the maximum at the concentration C_1 concentration of the primary crystal. Since the concentration of nuclei C_1 is quite different from that of the amorphous matrix phase C_0 , diffusion of the solute atoms must be involved in this process. This crystallization process is called primary crystallization. Due to diffusion controlled grain growth the microstructure obtained by this process is generally very fine. When large homogeneous nucleation rate or a high density of heterogeneous nucleation sites is available and the subsequent grain growth rate is effectively controlled, nanocrystalline microstructure forms by such primary crystallization process.

Perception of the primary phase from its amorphous matrix leads an increase in concentration of solute atoms in the remaining amorphous phase because at this time the solute atoms are rejected from primary particles. The concentration of the solute may reach as high as that of β phase. The microstructure obtained in this way is still in the metastable state composed of the α and the remaining amorphous phase (indicated by the tangent CG). As a consequence further annealing causes another polymorphous crystallization (G→H→I) of the remaining amorphous phase which end up with α/β equilibrium (CI). So the crystallization process which develops nanocrystalline microstructure from its amorphous precursor, progress in two stages as



Where α is a primary phase that precipitates from the amorphous matrix and β is a intermetallic compound. Formation of such two steps crystalline phase is elucidated in calorimetric experiment such as isochronal DSC or DTA measurement. FINEMET the experimental amorphous alloys in the present work are not simple binary alloys as shown in the model above, hence more than one type of intermetallic phase is expected in the second stage suggesting that the crystalline processes in multicomponent commercial amorphous alloys are more complicated than that described in this binary alloy model.

3.11 Magnetic Dipole Moments and Magnetization:

The vast majority of soft magnetic materials have one or more of the ferromagnetic transition metal elements, Fe, Co or Ni or the rare earth metal Gd as a majority component. The magnetic dipole moments of elemental and alloy magnets are most completely understood through the *Band Theory of Solids* [3.20]. The band theory of solids considers the broadening of localized atomic state with discrete eigenvalues into a continuum of states for more itinerant electrons over a range of energies. The theory allows for calculation of energy dispersion (i.e. energy as a function of wave vector) and orbital angular momentum specific and spin resolved densities of states. The calculation of spin-resolved energy-bands and densities of states allows for the description of atom resolved magnetic dipole moments, and, therefore, spontaneous magnetization of elemental and alloy magnetic solids. Among the successes of band theory descriptions of magnetic properties are:

1. The prediction of non-integral or half-integral atomic dipole moments and resulting ground state magnetizations in metals and alloys.
2. The prediction that band width and exchange splitting (energy differences between spin up and spin down bands) are intimately dependent on magnetic coordination number and atomic value.

Table-3.2 summarizes absolute zero and room temperature (where applicable) magnetizations and atomic dipole moments for some important transition metal and rare earth elemental magnets. Also shown are Curie temperatures i.e. ferromagnetic ordering temperatures which are not ground state properties that are directly calculable from band theory.

Table-3.2 Spontaneous and room temperature magnetizations, magnetic dipole moments and Curie temperature for elemental ferromagnets [2.1]

Element	$\mu_m @ 0 \text{ K} (\mu_B)$	$M_s @ 0 \text{ K}$ (G)	$M_s @ RT$ (G)	T_C (K)
Fe	2.22	1740	1707	1043
Co	1.72	1446	1400	1388
Ni	0.606	510	485	627
Gd	7.63	2060	–	292
Dy	10.2	2920	–	88

Fig.3.10(a) shows the Slater-Pauling curve that illustrates the variation of the mean atomic dipole moment as a function of composition in transition metal alloy systems. Fig.3.10(c) and (d) shows spin resolved densities of states $g_+(E)$ and $g_-(E)$ for Co and Fe atoms, in an equiatomic FeCo alloy, as a function of energy (where the Fermi energy E_F is taken as the zero of energy). The number of spin up, n_+ and spin down, n_- electrons in each band can again be calculated by integrating these densities of state:

$$n_+ = \int_{E_1}^{E_2} g_+(E) dE \quad \text{and} \quad n_- = \int_{E_1}^{E_2} g_-(E) dE \quad \dots\dots\dots(3. 36)$$

(here the Fermi energies, E_F , are the same and the zero's of energy are different for the two spin bands) and the atom resolved (i.e., Fe and Co) magnetic dipole moments can be calculated as:

$$\mu_m = (n_+ - n_-)\mu_B \quad \dots\dots\dots(3. 37)$$

Knowledge of atomic values or alloy density, then allows for the direct calculation of the alloy magnetization. Fig.3.10(b) shows the band theory prediction of the average (spin only) dipole moment in a $Fe_{1-x}Co_x$ alloys as a function of composition to be in good quantitative agreement with the experimentally derived Slater-Pauling curve.

For magnetic alloy design the Slater –Pauling curve is an important starting point. The desire for large induction limits the choices alloys to those rich in Fe or Co and therefore near the top of the Slater-Pauling curve. As described in the Slater-Pauling curve, Fe-Co alloys exhibit the largest magnetic inductions of any material, and also have Curie temperatures which are desirable for high temperature applications. Fe rich alloys typically have smaller inductions and lower Curie temperatures than Fe-Co alloys. Co alloys can also be soft but only if the FCC phase of Co is present. Co rich alloys typically have smaller inductions and larger T_c 's.

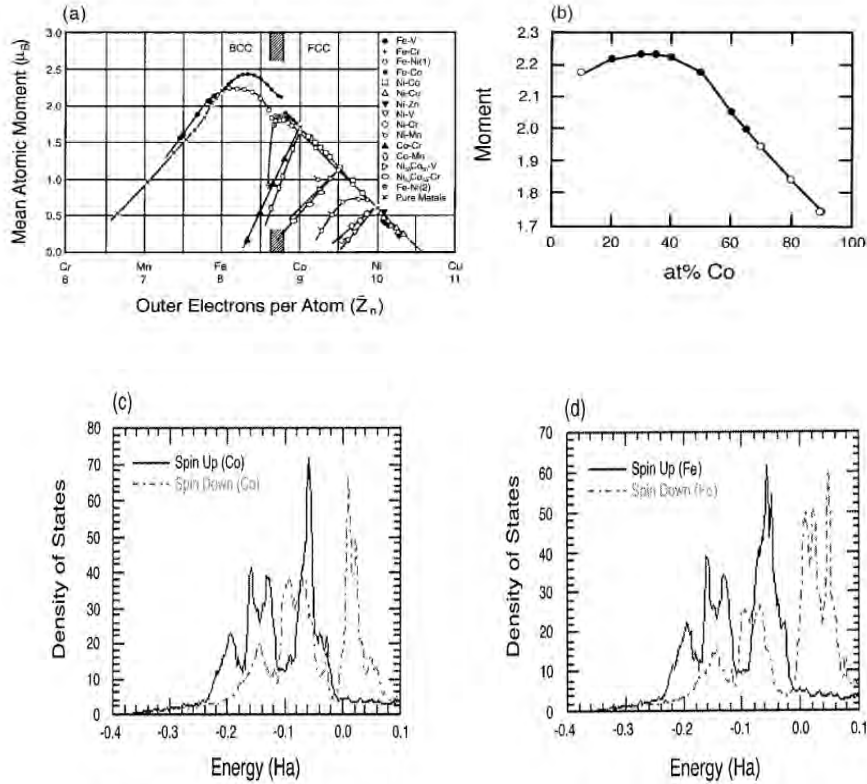


Fig.3.9.(a) Slater-Pauling curve for TM alloys (after Bozorth); (b) Spin only Slater Pauling curve for the ordered Fe-Co alloy as determined from LKKR band structure calculation; (c) Density of states for Co and Fe; (d) in the ordered equiatomic alloy[3.21]. The Fermi level is taken as the zero of energy.

3.12 Magnetocrystalline anisotropy and Magnetostriction:

A single crystal of magnetic material, such as iron, exhibits preferred directions of magnetization. This means that in the absence of an external field, the spontaneous magnetization takes up a specific direction with respect to the crystal axes. In iron the direction is one of the cube edges so that there are six equivalent preferred or easy directions for the magnetization. This phenomenon is referred to as magnetocrystalline anisotropy.

When the spontaneous magnetization exhibits a preferred direction, this is evidently a minimum energy position for it. Thus we may argue that if magnetization is rotated out of this direction by the application of a field, there must be an increase of energy, in the material, which we describe as the anisotropy energy. The magnetic anisotropy energy describes the angular dependence of the magnetic energy i.e. its dependence on θ and ϕ between the

magnetization and easy axis of magnetization [3.22, 3.23]. The anisotropy energy can be further subdivided into magnetocrystalline, shape and stress anisotropies, etc.

Since the magnetic anisotropy represents a barrier to switching the magnetization for soft magnetic materials, a small magnetic anisotropy is desired so as to minimize the hysteresis losses and maximize the permeability. The desire for small magnetocrystalline anisotropy necessitates the choice of cubic crystalline phases of Fe, Co, Ni or alloys such as FeCo, FeNi, etc. (with small values of K_1). In crystalline alloys, such as permalloy or FeCo, the alloy chemistry is varied so that the first order magnetocrystalline anisotropy energy density K_1 is minimized.

Similarly, stress anisotropy is reduced in alloys with nearly zero magnetostriction. Shape anisotropy results from demagnetization effects and is minimized by producing materials with magnetic grains with large aspect ratios. In amorphous soft magnetic alloys, low magnetic anisotropy results from the lack of crystalline periodicity.

Magnetostriction is the process by which the shape of a ferromagnetic material changes in the process of magnetization as a result of magnetoelastic interactions. Magnetostriction results in ferromagnetic material being strained during the process of magnetization. The average strain dL/L for a typical transition metal ferromagnet is in the order of 10^{-5} - 10^{-6} . Magnetostriction is a deleterious property for soft magnetic applications (i.e., it is the source of loss in transformers by transformer hum). The strain in a magnetostrictive material increases with increasing field until such point that it saturates having a value λ_s .

The physical origin of magnetostrictive response lies in spin-orbit interactions as is also the case for magnetocrystalline anisotropy. The magnetostrictive component involves magnetoelastic coupling and the dilation or expansion of the lattice as a consequence of rotation of the magnetization in the magnetization process. Magnetostrictive coefficients are also dependent on chemical composition and can be optimized (subject to other constraints) by varying the chemistry [3.24].

As an example of dependence of magnetic anisotropy and magnetostriction (as well as magnetization) on alloy chemistry, Fig.3.10. illustrates the variation of saturation induction, Curie temperature, magnetocrystalline anisotropy K_1 and magnetostriction λ , in FeCo alloys. In choosing a binary alloy composition in the binary $Fe_{1-x}Co_x$ system it is important to consider the maximum induction which occurs near $x = 0.3$ [2.1], the minimum magnetocrystalline anisotropy which occurs near $x = 0.5$ and finally compositions which minimize magnetostrictive coefficients.

In the FeCo alloys, magnetostriction coefficients λ_{111} and λ_{100} are both substantial near the equiatomic composition where the magnetocrystalline anisotropy vanishes. Across this alloy system, Curie temperatures are large enough to cause no problems in high temperature magnetization (i.e. 500 °C). Magnetostriiction considerations are known to be quite important in the design of soft magnetic materials for inductive devices, transformers and a host of other applications.

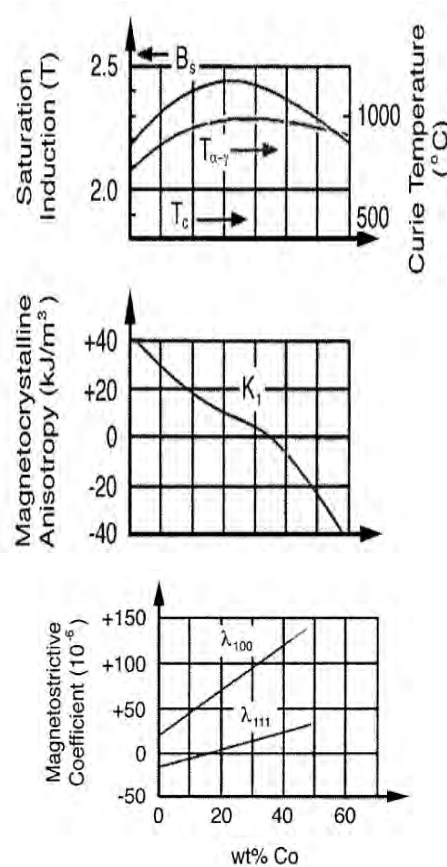


Fig.3.10 (a) Saturation magnetization and Curie temperature, (b) magnetocrystalline anisotropy K_1 and magnetostriction λ in the FeCo system (reproduced from Pfeifer and Radeloff [3.25]).

3.13 Random Anisotropy Model

A low or vanishing magnetocrystalline anisotropy is the major requirement for superior soft magnetic behavior. The magnetocrystalline anisotropy K_1 is related to crystal symmetry where the easy axis of magnetization is determined by the crystal axis. In case of the constituent phase of nanocrystalline $\text{Fe}_{73.5}\text{Cu}_1\text{Nb}_3\text{Si}_{13.5}\text{B}_9$, i.e., the Fe-Si(20at.%), the anisotropy constant is about $K_1 \approx 8 \text{kJ/m}^3$ [3.26] which contributes to the low coercivity ($H_c < 1 \text{A/m}$) and thereby, a high permeability ($\mu_r \approx 10^5$). The key to understand this is that the effective anisotropy

contribution of the small, randomly oriented grains is essentially reduced by exchange interaction [3.27, 3.28]. The critical scale where the exchange energy starts to balance anisotropy energy is given by the ferromagnetic exchange length,

$$L_0 = \sqrt{\frac{A}{K_1}} \dots \dots \dots (3.38)$$

Where A = exchange stiffness constant, which is about $L_0 \approx 35$ nm for the material parameters of Fe-Si (20 at.%). L_0 represents the minimum length scale over which the direction of magnetic moments can vary appreciably and for example, determines the domain wall width. Thus, if the grain size D is reduced below L_0 , the magnetization will not follow the randomly oriented easy axis of the individual grains, but increasingly is forced to align parallel by the exchange interaction. As a consequence, the effective anisotropy is an average over several grains and thus considerably reduced in magnitude.

The degree to which the magnetocrystalline anisotropy is finally averaged out has been explained in detail in terms of the ‘Random Anisotropy Model’ [3.27, 3.28]. The ‘Random Anisotropy Model’ was originally developed by Alben *et al.* in order to explain the soft magnetic properties of amorphous ferromagnets. A theoretically more sophisticated treatment can be found in the paper of [3.29].

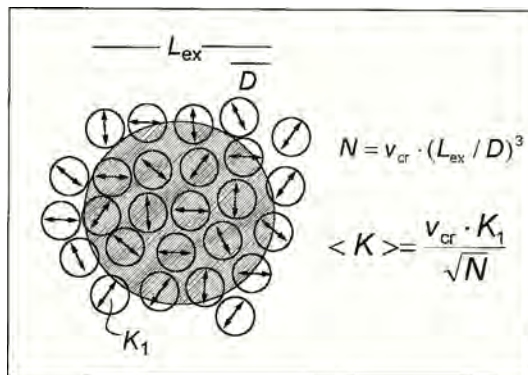


Fig.3.11 Schematic representation of the random anisotropy model for grain embedded in an ideal soft ferromagnetic matrix. The double arrows indicate the random fluctuating anisotropy axis, hatched area represents the ferromagnetic correlation volume determined by the exchange length $L = (A/K_1)^{1/2}$.

The basic idea sketched in fig.3.11 and starts from an assembly of grains of size D and volume fraction v_{cr} with magneto-crystalline anisotropies oriented at random. The effective anisotropy constant $\langle K \rangle$ relevant to the magnetization process results from averaging over the $N = v_{cr} \frac{V}{V_0}$ grains within the ferromagnetic correlation volume $V = V_0$ determined by the exchange

length L_{ex} . For a finite number N , of grains within the exchange volume there will be always some easiest direction determined by statistical fluctuations. Thus average anisotropy energy is determined by the mean fluctuation amplitude of the anisotropy energy of the N grains i.e.

$$\langle K \rangle \approx \frac{1}{\sqrt{1}} \overline{K_1} \left(\frac{1}{1} \right)^{3/2} \dots \dots \dots (3.39)$$

As local magneto-crystalline anisotropies are averaged out in this way, the scale on which exchange interaction dominates expands at the same time. Thus, the exchange length L_{ex} has to be normalized by substituting $\langle K \rangle$ for K_1 in Eq.(3.38) i.e. L_{ex} is self-consistently related to the average anisotropy by

$$L_{ex} = \frac{1}{\langle K \rangle} \dots \dots \dots (3.40)$$

The combination of Eqs.3.39 and 3.40 then yields for grain sizes smaller than the exchange length

$$\langle K \rangle \approx v_{cr}^2 K_1 (D/L_0)^6 = v_{cr}^2 D^6 K_1^4 / A^3 \dots \dots \dots (3.41)$$

The most significant feature predicted by the Random Anisotropy Model is the strong variation of $\langle K \rangle$ with the sixth power of grain size. Thus for $D \approx L_0/3$ i.e. grain sizes in the order of 10-15 nm, the magneto-crystalline anisotropy is reduced by three orders of magnitude towards a few J/m^3 i.e. small enough to enable superior soft magnetic behavior. Correspondingly, renormalized exchange length L_{ex} , expands into the μm -regime and thus is almost two orders of magnitude larger than natural exchange length L_0 .

If there are no other anisotropies, coercivity and initial permeability is closely related to $\langle K \rangle$ by

$$H_c = p_c \frac{\langle K \rangle}{J_s}; \quad \mu_i = p_\mu \frac{1}{1} \frac{1}{\langle K \rangle} \dots \dots \dots (3.42)$$

Where J_s is the average saturation magnetization of the material p_c and p_μ are dimensionless pre-factors close to unity. In the regime $D \ll L_{ex}$, coherent magnetization rotation as well as domain wall displacement is observed [3.28].

Actually, on the scale of 10 nm small grains, the magnetization vector appears to rotate coherently if a $2\mu m \approx (L_{ex})$ wide domain wall passes by.

Herzer's model considering the additional effect of a more long range uniaxial anisotropy (K_u) i.e. with an interaction length scale $\gg L_{ex}$. Under these conditions the effective anisotropy can be written as:

$$1 \frac{1}{1} \frac{1}{1} = 1 \left(\overline{1} + 1 \frac{1}{1} \frac{1}{1} \right) \dots \dots \dots (3.43)$$

Where $K_{eff,nc}$ is the effective anisotropy of the nanocrystalline material in the absence of the additional uniaxial anisotropy i.e. as originally expressed by Herzer. Inserting the Herzer expression into Eq.(3.43) yields:

$$K_{eff,nc} = \left(K_{111} + \frac{K_{111}^2 (K_{111})^{1/2}}{K_{111}^{1/2}} \right)^{1/2} \dots \dots \dots (3.44)$$

That cannot be solved analytically but in the limit $K_{111} \gg K_{111,111}$ reduces to:

$$K_{eff,nc} = K_{111} + \frac{1}{2} \frac{K_{111}^2 (K_{111})^{1/2}}{K_{111}^{1/2}} \dots \dots \dots (3.45)$$

as is experimentally observed. These macroscopic uniaxial anisotropies can be attributed to the effects of induced anisotropy due to the domain structure produced during annealing or due to magnetoelastic interactions.

3.14 Magnetic coupling in two phase microstructures:

There are two conditions required for Herzer’s model to have validity:

- (1) The grain size must be smaller than the magnetic exchange correlation length and
- (2) the grains must remain ferromagnetically coupled.

In a single phase nanocrystalline alloy, as long as the first criterion is met, and the alloy is below Curie temperature, the model holds. This is not necessarily the case for multiphase system such as we find in many of the nanocrystalline alloys that are produced from amorphous precursors.

For a two phase microstructures with a ferromagnetic intergranular amorphous phase and a single ferromagnetic nanocrystalline phase, the nature of the nanocrystal amorphous nanocrystal coupling is of paramount importance to the properties of these materials. This coupling depends upon the size of the nanocrystallites, and more importantly upon the amount, chemistry and thickness of the amorphous phase. The best properties, of course, are when both criteria are met, below presumably the lower Curie temperature of the amorphous phase.

Slawska-Waniewska *et al.* [3.30] have observed T-dependent magnetic response in partially and fully nanocrystallized FINEMET materials. They concluded that for sufficiently small nanocrystals with enough intergranular material between them to diminish or destroy coupling between grains that superparamagnetic response would be observed. This would not be the case for properly annealed samples with sufficient volume fraction of the nanocrystalline ferromagnet. Characteristic of superparamagnetic response, first proposed by Bean [3.31]

include: (1) a Langevin function (H/T) scaling of magnetization data; (2) disappearance of the coercivity above a blocking temperature and (3) time dependent magnetization, due to thermally activated switching of the magnetization.

Additional work on the superparamagnetism of uncoupled particles in FINEMET alloys was carried out by Skorvanek and O' Handley [3.32]. They studied magnetic interactions between nanoparticles above the Curie temperature of the intergranular amorphous phase. They showed that the magnetic interactions increase with the increasing nanocrystalline volume fraction. These interactions tend to suppress superparamagnetic fluctuations. They observed that coercivity $H_c(T)$ with the increase of temperature reached a maximum near the Curie temperature of the amorphous phase which indicates the suppression of interparticle coupling.

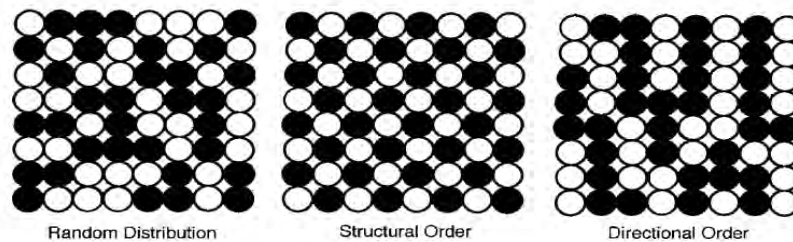


Fig.3.12 Schematic view of A (filled) and B(open) atom distributions in (a) a disordered (random), (b) a structurally ordered and (c) a directionally ordered AB alloy.

Defining a phenomenological parameter γ , parameterizes the exchange interaction through the amorphous matrix phase, Hernando [3.33, 3.34] has developed a model which predicts a peak in $H_c(T)$ at the Curie temperature of the amorphous phase. Further developments of this model are described Hernando *et al.* [3.35, 3.36]. Hernando [3.35] has found that above $\gamma_{am} \sim 0.85$ the material acts as an assembly of single domain particle that become superparamagnetic about T_1^{11} .

Interestingly, the observed Curie temperature T^{am} is nearly 100 K higher than T_1^{11} * that expected for the amorphous matrix of the same composition in an as cast ribbon. A parameterization of the intergranular spacing A is used in a description of the enhancement of T_1^{11} to T_1^{11} *. This intergranular spacing is:

$$A = d \left[\left(\frac{1}{X} \right)^{1/3} - 1 \right] \dots \dots \dots (3.46)$$

Where d is the average grain size and X is the volume fraction of α -Fe nanocrystals. With this parameter defined, a linear dependence has been postulated of the form:

$$T_1^{11} - T_1^{11} * = \frac{11}{\Lambda} (1_1^{1111} - T_1^{11} *) \dots \dots \dots (3.47)$$

With L_{ex} is the exchange correlation length. This result has been attributed to exchange coupling enhancement in the amorphous phase near the interface with the ferromagnetic nanocrystals. This enhancement will only be observable in materials with large surface area/volume ratios.

As mentioned earlier, Hernando [3.37] has offered a parameterization that describes decoupling of ferromagnetic nanocrystals above the Curie temperature of the amorphous phase. The details of this model involve definition of an exchange correlation length coefficient γ_{ex} , which has values ranging between zero (decoupled) and one (fully coupled-Herzer model). He has developed relationships for multiphase systems beginning by defining:

$$\gamma_{ex} = \exp\left[-\frac{L}{L_{am}}\right] \dots \dots \dots (3.48)$$

where L_{am} is the exchange length of the amorphous phase. Three notable relationships are:

1. The first of this is a modified exchange correlation length L^* , expressed as a function of the exchange correlation length coefficient:

$$L^* = \frac{L_{ex}}{\gamma_{ex}} \dots \dots \dots (3.49)$$

Where L_{ex} is the single phase exchange correlation length originally proposed by Herzer. The dependence of L^* on X profoundly modifies the D^6 dependence of H_c .

2. The second of these is a new parameterization of the magnetocrystalline anisotropy that is also a strong function of the exchange correlation length coefficient:

$$k^* = \frac{k_1}{\gamma_{ex}} \dots \dots \dots (3.50)$$

3. Finally, a third relationship describes critical size of crystallites δ^* below which a reduction in coercivity due to random anisotropy will be observed. It is:

$$\delta^* = \delta_0 \frac{L_{ex}}{L^*} \dots \dots \dots (3.51)$$

where δ_0 is the maximum size of crystallites. In the Herzer model, where $\delta < \delta_0$ then the critical size is independent of the amount of crystalline phase at any temperature. However, in the two-phase model, since δ grows to exceed δ^* (either by increasing temperature or decreasing volume fraction of crystalline material) a variety of experimental results can be explained (i.e. magnetic hardening etc.)

Hernando [3.37] has extended his two-phase effective anisotropy ideas, considering temperature dependent effects. He has shown that the average local anisotropy changes with temperature-dependence for a single-phase system as M_s^{4n-s} ($n > 2$). For two-phase materials:

$$M_s^* = \frac{M_s^{4n-s} (1 - X)}{1 - X} \dots \dots \dots (3.52)$$

Where $H_c(T)$ gives the single-phase dependence. The dependence of γ on temperature is found by considering temperature dependence of the terms used in the definition of γ_{ex} . In turn $\gamma_{ex}(T)$ can be used to determine the temperature dependence of the exchange correlation length charge :

$$L_{ex} = \left(\frac{A_m}{K_m} \right)^{1/2} \sim [A_m / (K_m)]^{1/2} \dots\dots\dots(3.53)$$

Where $n' > 2$ and A_m and K_m are exchange stiffness and magnetic anisotropy respectively, for the amorphous phase. So, when $L_{am} < \delta$ there is decoupling of adjacent grains where H_c is a maximum at $L_{am} = \delta$. Further increase in temperature should result in monodomain response which for combination of small particle volumes and magnetic anisotropies leads to superparamagnetic behavior and a characteristic temperature dependence of coercivity:

$$H_c(T) = \frac{K_m}{M_s} \left(1 - \frac{L_{am}}{\delta} \right) \dots\dots\dots(3.54)$$

For temperature exceeding the blocking temperature of the particles, T_B .

3.15 Concepts and Theories of Permeability:

Permeability, the magnetic term simply means the response of atomic magnetic dipoles to the applied magnetic field. Mathematically it is defined as the ratio of flux density (B) to field strength(H). Symbolized by μ , the mathematical definition can be expressed as

$$\mu = B/H \dots\dots\dots(3.55)$$

Several types of permeabilities are defined mathematically according to requirement for study of properties of magnetic materials when field applied. A few are given below:

3.15.1 Complex permeability $\underline{\mu}$:

Because of the phase shift between flux density and field strength in the alternating field, their quotient in complex notation is likewise a complex quantity. The permeability then comprises a real and imaginary part. The customary notation, applicable in particular at small excitation and under sinusoidal magnetization condition is: $\underline{\mu} = \mu' - j\mu''$ where μ' & μ'' are the real and imaginary components.

The complex permeability is often represented by a locus curve, as shown in fig.3.13.

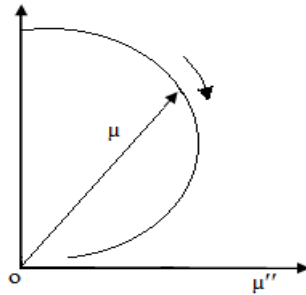


Fig.3.13 Representation of the complex permeability

3.15.2 Initial permeability μ_i :

Initial permeability is the amplitude permeability when the field strength or the flux density is vanishingly small.

Mathematically, the initial permeability μ_i in terms of magnitude is defined as the derivative of induction B with respect to internal field H in the demagnetized state:

$$\mu_i = \frac{dB}{dH}, \quad H \rightarrow 0, B \rightarrow 0 \quad \dots\dots\dots(3.56)$$

At microwave frequencies and also in low anisotropic materials, dB and dH may be in different directions. In the case of polycrystalline materials containing a large number of randomly oriented crystallites, the permeability will be a *scalar*, at least at low frequencies.

In electromagnetism, permeability is the degree of magnetization of materials that responds linearly to an applied magnetic field. Permeability in terms of magnitude is defined as the proportionality constant between the magnetic field induction B and applied intensity H,

$$B = \mu H \quad \dots\dots\dots(3.57)$$

If a magnetic material is subjected to an ac magnetic field as given below

$$H = H_0 e^{i\omega t} \quad \dots\dots\dots(3.58)$$

Then it is observed that the magnetic flux density B experiences a delay. The delay is caused due to the presence of various losses and is thus expressed as

$$B = B_0 e^{i(\omega t - \delta)} \quad \dots\dots\dots(3.59)$$

where δ is the phase angle and marks the delay of B with respect to H. The permeability is then given by

initial permeability of this toroid shaped sample was measured by obtaining the L value provided by an inductance analyzer used for permeability measurement (mentioned in detail in chapter 4) as value of L_0 is derived by the calculation given above.

3.16 Permeability mechanisms:

The behavior of μ' and μ'' versus frequency is called a *permeability spectrum*. To understand this spectra, it is necessary to discuss the permeability mechanisms including wall permeability and rotational permeability.

3.16.1 Wall permeability:

The mechanism of wall permeability arises from the displacement of domain walls in small fields. Let us consider a piece of material in the demagnetized state, divided into Weiss domains with equal thickness L by means of 180° Bloch walls shown in Fig.3.14. The magnetization M_s in the domains being oriented alternately in the +z or -z direction, the walls are parallel to the yz plane.

When field H with a component in the +z direction is applied, the magnetization in this direction will be favored.

A displacement dx of the walls in the direction shown by the dotted lines will decrease the energy density by an amount, $2M_s H_z dx/L$. This can be described as a pressure $M_s H_z$, exerted on each wall. The pressure will be counteracted by restoring force, which for small deviation may be assumed to be $-k dx$ per unit wall surface. The new equilibrium position is then given by $d = 2M_s H_z / K$.

From the change in the magnetization $\Delta M = 2M_s d/L$. The wall susceptibility χ_w may be calculated. Let H make the angle θ with z direction. The magnetization in the direction becomes $(\Delta M)_\theta = 2M_s (d/L) \cos \theta$.

And with $H_z = H \cos \theta$ and $d = 2M_s H_z / k$,

$$\text{We obtain } \chi_w = \frac{(\Delta M)_\theta}{H} = \frac{11 \uparrow 111 \uparrow 1}{11} \dots \dots \dots (3.68)$$

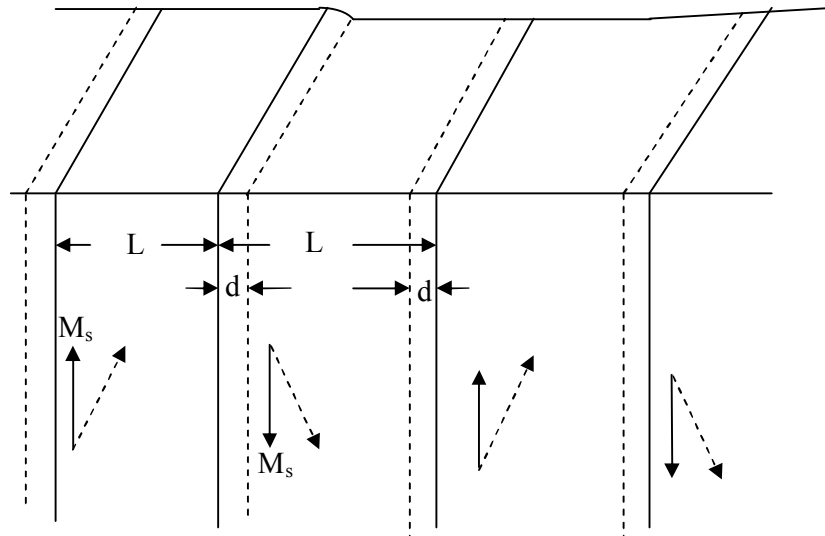


Fig.3.14 Magnetization by wall motion and spin rotation

3.16.2 Rotational permeability:

The mechanism of rotational permeability arises from rotation of the magnetization in each domain. The direction of \mathbf{M} can be found by minimizing the magnetic energy E as a function of the orientation. An important contribution to E comes from the crystal anisotropy energy. Other contributions may be due to the stress and the shape anisotropy. The stresses may influence the magnetic energy via the magnetostriction. The shaped anisotropy is caused by the boundaries of the sample as well as by pores, nonmagnetic inclusions and inhomogeneties.

The total anisotropy energy for small angular deviation α_x and α_y of \mathbf{M} , (where $\alpha_x = M_x/M_s$ and $\alpha_y = M_y/M_s$) from the equilibrium (z) direction may be expressed as

$$E = E_0 + \frac{1}{2} K_1 \alpha_x^2 + \frac{1}{2} K_2 \alpha_y^2 \dots \dots \dots (3.69)$$

where it is assumed that x and y are the principal axes of the energy minimum. Instead of E_{xx} and E_{yy} the anisotropy field H_{k1} and H_{k2} are often introduced. Their magnitude is defined by

$$H_{k1} = 2M_s / E_{xx} \text{ and } H_{k2} = 2M_s / E_{yy} \dots \dots \dots (3.70)$$

Where H_{k1} and H_{k2} represent the stiffness with which the magnetization is bound to the equilibrium direction for the deviations in the x and y directions respectively. The rotational susceptibilities $\chi_{r,x}$ and $\chi_{r,y}$ for fields applied along x and y directions are respectively expressed as

$$\chi_{r,x} = M_s / H_{k1} \text{ and } \chi_{r,y} = M_s / H_{k2} \dots \dots \dots (3.71)$$

For cubic materials it is often found that χ_{11} and χ_{11} are equal or nearly equal. For $\chi_{11} = \chi_{11} = \chi_{11}$ and a field H which makes an angle θ with the z direction as shown in Fig.3.14 The rotational susceptibility $\chi_{r,c}$ in one crystallite becomes

$$\chi_{r,c} = \frac{1}{3} \sin^2 \theta \dots \dots \dots (3.72)$$

If the crystal anisotropy dominates other anisotropies, then χ_{11} will be constant throughout the material, so only the factor $\sin^2 \theta$ from equation has to be averaged. Snoek assuming a linear averaging of $\chi_{r,c}$, found the rotational susceptibility

$$\chi_r = \frac{1}{3} \chi_{11} \dots \dots \dots (3.73)$$

Thus we obtain the total internal susceptibility,

$$\chi = \chi_w + \chi_r = \frac{1}{3} \chi_{11} + \frac{1}{3} \chi_{11} \dots \dots \dots (3.74)$$

3.17 AC magnetic response:

Soft magnetic material's magnetic loss mechanism include: (1) hysteresis loss due to irreversible domain wall motion and rotational out of easy axes loss mechanism, (2) eddy current losses and (3) anomalous losses. The energy loss per cycle is given by $\oint H dB$ and linear response the power loss is $f \times B^2/2\mu$ where f is the frequency. In real materials (which are nonlinear) we express the hysteresis power loss as:

$$P_h \sim C_h f B_{max}^n \dots \dots \dots (3.75)$$

Where C_h may vary with the material and atypical exponent n is ~ 1.6 . Eddy current loss results from the fact that $d\phi/dt$ induces voltages in the core material with consequent V^2/R power appearing as heat. This power can be reduced by decreasing V and increasing R . Since $V \sim f B_{max}$ i.e.

$$P_e^2 = C_e f^2 B_{max}^2 \dots \dots \dots (3.76)$$

To reduce the eddy current loss in sheet transformers, they are often laminated so as to reduce the length scale of eddy current loops.

total power loss:

$$P_{TOT} = P_h + P_e = C_h f B_{max}^n + C_e f^2 B_{max}^2 \dots \dots \dots (3.77)$$

The important physical parameters which can be altered to minimize alternating current (AC) losses is electrical resistivity ρ that influence the hysteresis loss and also eddy current loss as well as the high frequency loss. Large electrical resistivities are essential for reducing AC losses. Electrical resistivities in amorphous alloys can be several hundred $\mu\Omega$ cm and for

nanocrystalline alloys $\sim 50 \mu\Omega \text{ cm}$, which in both cases offer significant advantage over crystalline metallic material ($\sim 1\text{-}10 \mu\Omega \text{ cm}$).

3.18 High frequency behavior & losses:

The frequency dependence of the absolute value of complex permeability and its imaginary part μ'' are expressed in terms of the relative loss factor $\mu''/|\mu|^2$.

The later is directly related to the cycle losses at constant induction amplitude B by

$$p/f = \pi B^2 \mu'' / \mu_0 |\mu|^2 \dots \dots \dots (3.78)$$

Fig shows the core losses of the nanocrystalline Fe-Cu-Nb-Si-B alloys are comparable to those of amorphous Co-based alloys and pass by the properties of conventional materials even that of ferrites, over the whole frequency range up to several 100 kHz.

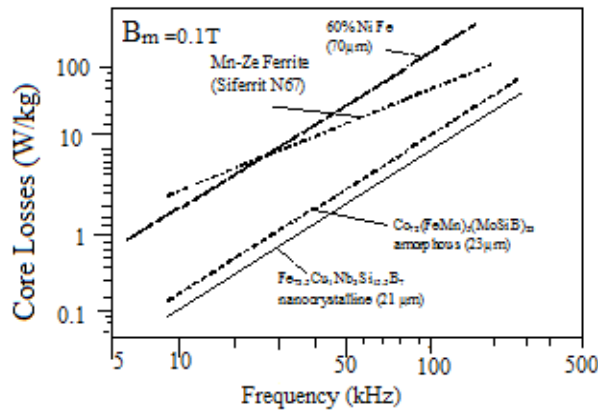


Fig.3.15 Low core losses of Fe-based nanocrystalline alloy at high frequency

The favorable high frequency behavior is essentially related to (i) the thin ribbon gauge of $d \approx 20 \mu\text{m}$ inherent to the production technique and (ii) to a relatively high electrical resistivity of typically $\rho \approx 115 \mu\Omega\text{-cm}$ related to the high Si-content in the b.c.c. grains [3.38] and the intergranular amorphous phase. Both parameters are comparable to amorphous metals and yield low eddy current losses p_e which in thin sheets at a frequency f and a induction level B are given per volume by

$$p_e = (3 \sinh x - \sin x) (\pi d f B)^2 / (x \cosh x - \cos x) 6\rho \dots \dots \dots (3.79)$$

$$|p_e|_{x \ll 1} = (\pi d f B)^2 / 6\rho$$

with $x = 2\sqrt{(f/f_w)}$, where $f_w = 4\rho / (\pi d \mu_0 \mu_i^2)$

Is the limiting frequency above which the exciting magnetic field no longer fully penetrates the specimen and accordingly, the permeability decreases as a function of frequency.

4.1 Melt spin system:

Amorphous alloys in the form of ribbons have been prepared by single roller melt-spinning technique in air. Melt spin system presented schematically in fig.4.1 is a small laboratory system, especially designed for production of amorphous and microcrystalline ribbons. Melting of material is performed by a high frequency generator with water-cooled induction coil. Molten material flows through a slot on a fast rotating copper wheel. The melt is quenched with a cooling rate of more than 10^6 K/s which solidifies in an amorphous structure.

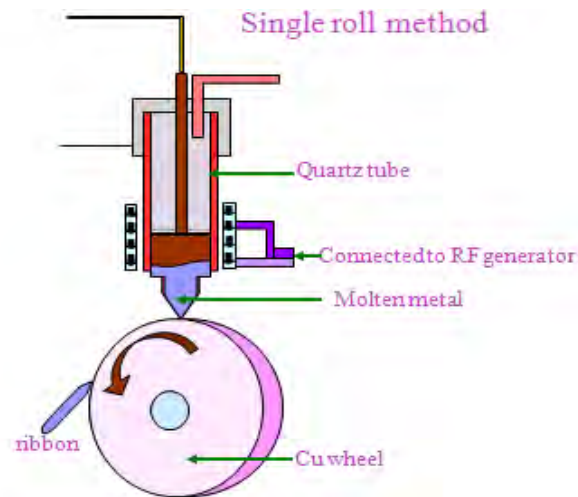


Fig 4.1 Schematic diagram of melt spin system

4.2 Preparation of Fe-based soft magnetic ribbon by melt spin system

Amorphous alloys of composition of $(\text{Fe}_{0.8}\text{Co}_{0.2})_{73.5}\text{Cu}_1\text{Nb}_3\text{Si}_{13.5}\text{B}_9$ were prepared in the form of ribbons using melt-spin machine. The purity and origin of constituent elements were Fe (99.95%), Co (99.95%), Cu(99.95%), Nb(99.99%), Si(99.95%), B(99.99%) from Johnson Matthey (Alfa Aesar). Constituent elements in the correct proportions were mixed and melted in the arc-melting furnace under vacuum of 10^{-6} mbar pressure. In order to homogenize perfectly, the alloys were melted three times. The ingots were then poured into a quartz tube having an orifice diameter of 1 mm. quartz tube was placed inside an induction coil associated with machine. A steel casing covers whole assembly of single roller melt-spin machine. In the beginning the chamber inside the casing was flashed by Ar gas three times. The chamber was then filled with Ar gas. The alloy ingots were then melted by induction melting. Appropriate temperature of the melt was assumed from the color by eye estimation. When the color of the

melt was appropriate amorphous ribbons were obtained in Ar atmosphere by purging the melt using Ar pressure. Wheel speed of single roller melt spin machine was around 25 m/s.

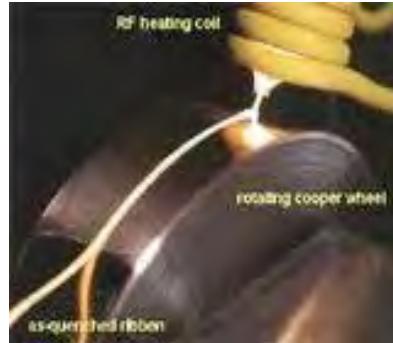


Fig.4.2 Melt spinning Machine

4.3 Thermal Analysis Techniques

Thermal analysis comprises of a group of techniques in which a physical property of a substance is measured as a function of temperature, while the substance is subjected to a controlled temperature program. In differential thermal analysis, the temperature difference that develops between a sample and an inert reference material is measured. When both are subjected to identical heat treatments. The related technique of differential scanning calorimetry relies on differences in energy required to maintain the sample and reference at an identical temperature.

4.3.1 Differential thermal analysis (or DTA)

The Differential Thermal Analysis (DTA) is a technique to study the structural change occurring both in solid and liquid materials under heat treatment. These changes may be due to dehydration, transition from one crystalline variety to another, destruction of crystalline lattice, oxidation, decomposition etc. The principle of DTA consists of measuring the heat changes associated with the physical and chemical substance is gradually heated. This technique can also be used to identify the magnetic ordering of the amorphous ribbons. In order to discuss the possible applications of DTA, let us briefly define the various temperatures that are useful in characterizing the amorphous nanocrystalline alloys.

This technique has been used in determining the first crystallization temperature (T_{c1}) and second crystallization temperature (T_{c2}) of our nanocrystalline soft magnetic material. The first

crystalline temperature is defined as the temperature at which the alloy passes from the solid to liquid state. For our purposes it is sufficient to describe T_c as the temperature at which atomic mobility is great enough to allow diffusive rearrangement to occur in a matter of minutes. The crystallization temperature T_{cc} is defined as the temperature at which crystallization occurs with long range ordering. Metallic nanocrystalline glass ribbons usually are ductile in the as quenched condition, but may often embrittle by exposure to elevated temperature.

DTA techniques have been used to determine T_c and T_{cc} of our nanocrystalline ribbon of composition $(Fe_{0.8}Co_{0.2})_{73.5}Cu_1Nb_3Si_{13.5}B_9$. Based on Kissinger plots, crystallization activation energy of T_c and T_{cc} phases have been evaluated and presented in section 5.2 to 5.4 of chapter 5.

Principle

DTA is the process of accurately measuring the difference in temperature between a thermocouple embedded in a sample and a thermocouple in a standard inert material such as aluminium oxide, while both are being heated at a uniform rate. These differences of temperature arise due to phase transition or chemical reactions in the sample involving the evolution of heat or absorption of heat due to exothermic reaction or endothermic reaction measured. The exothermic and endothermic reactions are generally shown in the DTA trace as positive and negative deviations respectively from a baseline. So, DTA gives a continuous thermal record of reactions occurring in a sample.

When sample and reference substances are heated or cooled at a constant rate under identical environment, their temperature differences are measured as a function of time or temperature shown by the curve. The temperature of the substance which is thermally inactive, rises uniformly when heated, while the temperature of the sample under study changes anomalously when there is physical or a chemical change of the active specimen at a particular temperature. When there is an exothermic reaction, there is a peak in the temperature versus time curve, heat supplied from outside is consumed by the reaction. And when the reaction is over, the sample temperature gradually catch up the temperature of the inactive specimen. The temperature difference is detected, amplified and recorded by a peak.

From any endothermic reaction or change the active specimen absorbs heat which is reflected in the corresponding trough in the temperature versus time curve.

Changes in the sample, either exothermic or endothermic, can be detected relative to the inert reference. Thus, a DTA curve provides data on the transformations that have occurred, such as

glass transitions, crystallization, melting and sublimation. The area under a DTA peak is the enthalpy change and is not affected by the heat capacity of the sample.

Apparatus

As shown in Fig.4.3 a DTA consists of a sample holder comprising thermocouples, sample containers and a ceramic or metallic block; a furnace; a temperature programmer; and a recording system. The key feature is the existence of two thermocouples connected to a voltmeter. One thermocouple is placed in an inert material such as Al_2O_3 while the other is placed in a sample of the material under study. As the temperature is increased, there will be a brief deflection of the voltmeter if the sample is undergoing a phase transition. This occurs because the input of heat will raise the temperature of the inert substance, but be incorporated as latent heat in the material changing phase.

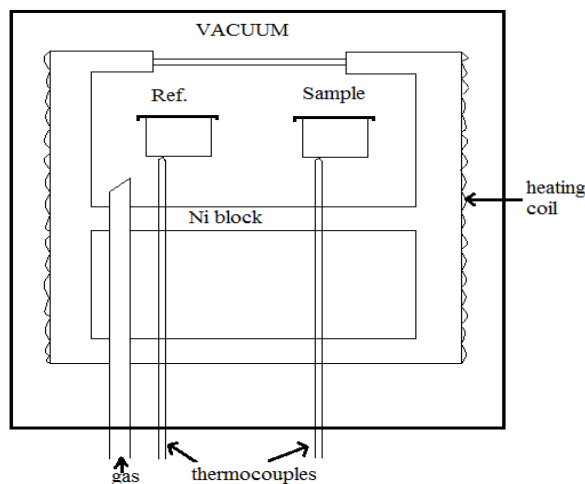


Fig. 4.3 Schematic illustration of a DTA cell.

The temperature in the sample holder is measured by a thermocouple, the signal of which is compensated for the ambient temperature and fed to the temperature controller. This signal is compared with the program signal and the voltage impressed to the furnace is adjusted. Thus the sample and the reference substance is heated and cooled at a desired rate. The temperature in the sample holder is digitally displayed on the DTA measurements model TG/DTA 6300 and is also recorded on the recorder.

4.4 Annealing

Annealing, in metallurgy and materials science, is a heat treatment wherein a material is altered, causing changes in its properties such as strength and hardness. It is a process that produces conditions by heating to above the critical temperature, maintaining a suitable

temperature, and then cooling. Annealing is used to induce ductility, soften material, relieve internal stresses, refine the structure by making it homogeneous, and improve cold working properties.

In the cases of copper, steel, silver, and brass, this process is performed by substantially heating the material (generally until glowing) for a while and allowing it to cool. Unlike ferrous metals, which must be cooled slowly to anneal, copper, silver and brass can be cooled slowly in air or quickly by quenching in water. In this fashion the metal is softened and prepared for further work such as shaping, stamping, or forming.

Annealing occurs by the diffusion of atoms within a solid material, so that the material progresses towards its equilibrium state. Heat is needed to increase the rate of diffusion by providing the energy needed to break bonds. The movement of atoms has the effect of redistributing and destroying the dislocations in metals and (to a lesser extent) in ceramics. This alteration in dislocations allows metals to deform more easily, so increases their ductility.

Stages

There are three stages in the annealing process, with the first being the recovery phase, which results in softening of the metal through removal of crystal defects (the primary type of which is the linear defect called a dislocation) and the internal stresses which they cause. Recovery phase covers all annealing phenomena that occur before the appearance of new strain-free grains. The second phase is recrystallization, where new strain-free grains nucleate and grow to replace those deformed by internal stresses. If annealing is allowed to continue once recrystallization has been completed, grain growth will occur, in which the microstructure starts to coarsen and may cause the metal to have less than satisfactory mechanical properties.

Setup and equipment

Typically, large ovens are used for the annealing process. The inside of the oven is large enough to place the workpiece in a position to receive maximum exposure to the circulating heated air. For high volume process annealing, gas fired conveyor furnaces are often used. For large workpieces or high quantity parts Car-bottom furnaces will be used in order to move the parts in and out with ease. Once the annealing process has been successfully completed, the workpieces are sometimes left in the oven in order for the parts to have a controlled cooling process. While some workpieces are left in the oven to cool in a controlled fashion, other materials and alloys are removed from the oven. After being removed from the oven, the workpieces are often quickly cooled off in a process known as quench hardening. Some typical methods of quench hardening materials involve the use of media such as air, water, oil, or salt. Quench hardening is generally applicable to some ferrous alloys, but not copper alloys.

4.5 Thermal Treatment of the amorphous ribbon:

With a view to study nanocrystallization behavior by XRD and magnetic properties upon evaluation of nanocrystalline phase on amorphous matrix thermal treatment i.e. annealing is required to perform. For XRD, as prepared amorphous ribbon were cut into small pieces of about 2cm length and for magnetic measurement such as permeability toroidal core were wound for annealing treatment. A laboratory built muffle furnace was heated to a certain temperature and kept for the time required to complete annealing. All the isothermal annealing of the amorphous samples was performed in air atmosphere.

4.6 Powder / polycrystalline diffraction

About 90 % of all solid materials can be described as crystalline. When X-ray interact with a crystalline substance (Phase), one gets a diffraction pattern. The X-ray diffraction pattern of a pure substance is, therefore, like a fingerprint of the substance. The powder diffraction method is thus ideally suited for characterization and identification of polycrystalline phases. Today about 50000 inorganic and 25000 organic single component, crystalline phase, diffraction patterns have been collected and stored on magnetic or optical media as standers. The main use of powder diffraction is to identify components in a sample by a search/ match procedure. Furthermore, the areas under the peak are related to the amount of each phase present in the sample.

4.6.1 Theoretical Considerations

In order to better convey an understanding of the fundamental principles of X-ray diffraction instruments, let us quickly look at the theory behind these systems. An electron in an alternating electromagnetic field will oscillate with the same frequency as the field. When an X-ray beam hits an atom, the electrons around the atom starts to oscillate with the same frequency as the incoming beam. In almost all directions we will have destructive interference, that is, the combining waves are out of phase and there is no resultant energy leaving the solid sample. However, the atoms in a crystal are arranged in a regular pattern and in a very few directions we will have constructive interference. The waves will be in phase and there will be well-defined X-ray beams leaving the sample at various directions. Hence, a diffracted beam may be described as a beam composed of a large number of scattered rays mutually reinforcing one another.

The orientation and interplanar spacing of these planes are defined by the three integers h, k, l called indices. A given sets of planes with indices h, k, l cut the a -axis of the unit cell in h sections, the b axis in k sections and the c axis in l sections. A zero indicates that the planes are parallel to the corresponding axis. For example the $2\ 2\ 0$ planes, in fig. 4.6, cut the a - and the b - axes in half, but are parallel to the c -axis.

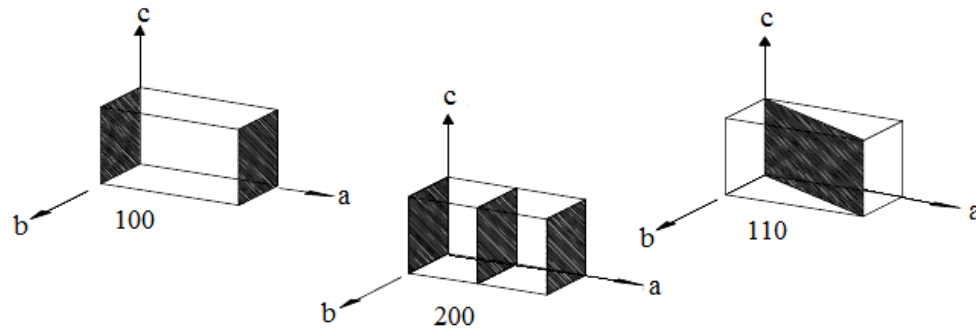


Fig.4.4 Diffractometer Slit System

If we use the three dimensional diffraction grating as a mathematical model, the three indices h, k, l become the order of diffraction along the unit cell axes a, b and c respectively. Let us consider the theoretical model depending on what we use the terms X-ray reflection and X-ray diffraction as synonyms.

Let us consider an X-ray beam incident on a pair of parallel planes P_1 and P_2 , in fig.4.7 separated by an interplaner spacing d . The two parallel incident rays 1 and 2 make an angle θ with these planes. A reflected beam of maximum intensity will result if the waves represented by 1' and 2' are in phase. The diffraction in path length between 1 to 1' and 2 to 2' must then be an integral number of wavelengths λ . We can express this relationship mathematically in Bragg's law $n\lambda = 2d \sin \theta$.

The process of reflection is described here in terms of incident and reflected (or diffracted) rays, each making an angle θ with a fixed crystal plane. Reflections occur from planes set an angle θ with respect to the incident beam and generates a reflected beam at an angle 2θ from the incident beam. The possible d -spacing defined by the indices h, k, l are determined by the shape of the unit cell. Rewriting Bragg's law we get, $\sin \theta = \lambda/2d$.

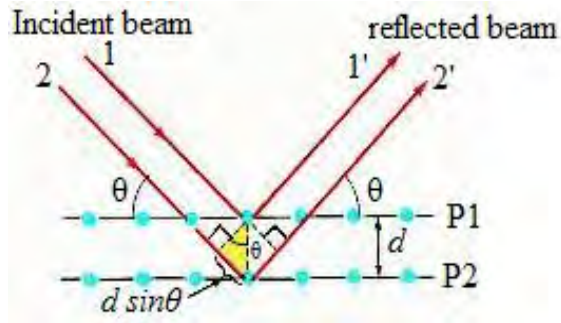


Fig.4.5 Bragg reflection of two parallel incident rays 1 and 2.

Therefore the two possible values where we can have reflections are determined by the unit cell dimensions. However, the intensities of the reflection are determined by the distribution of the electrons in the unit cell. The highest electron density is found around atoms. Therefore, the intensities depend on what kind of atoms we have and where in the unit cell they are located. Planes going through areas with high electron density will reflect strongly, planes with low electron density will give weak intensities.

Diffraction Slit System

The diffractometer slit system has been presented in Fig 4.6. The focal spot for a standard focus X-ray tube is about 10 mm long and 1 mm wide, with a power capability of 2000 watt, which equals to a power loading of 200 watt/mm². Power ratings are dependent on the thermal conductivity of the target material. The maximum power loading of a Cu X-ray tube is 463 watt/mm². This power is achieved by a long fine focus of the tube with a target size of 12 mm long and 0.4 mm wide. In powder diffraction the line focus or line source of the tube is normally utilized the line source emits radiation in all directions, but in order to enhance the focusing it is necessary to limit the divergence in the direction along the line focus. This is realized by passing the incident beam through a solar slit, which contains a set of closely spaced thin metal plates. In order to maintain a constant focusing distance it is necessary to keep the sample at an angle THETA (Omega) and the detector at an angle of 2-THETA with respect to the incident beam. For an THETA:THETA goniometer the tube has to be at an angle of THETA (Omega) and the detector at an angle of THETA with respect to the sample.

Diffraction Spectra

A typical diffraction spectrum consists of a plot of reflected intensities versus the detector angle 2θ or θ depending on the goniometer configuration. The 2θ values for the peak depend on the wavelength of the anode material of the X-ray tube. It is therefore customary to reduce a peak position to the interplanar spacing d that corresponds to the h, k, l planes that caused the reflection. The values of the d -spacing depend only on the shape of the unit cell. We get the d -spacing as a function of 2θ from Bragg's law $d = \lambda/2 \sin \theta$. Each reflection is fully defined when we know the d -spacing, the intensity (area under the peak) and the indices h, k, l . If we know the d -spacing and the corresponding indices h, k, l we can calculate the dimension of the unit cell.

ICDD Data Base

International Center diffraction data (ICDD) or formerly known as (JCPDS) Joint Committee on Powder Diffraction Standard is the organization that maintain the data base of inorganic and organic spectra's. The data base is available from the diffraction equipment manufacturers or from ICDD direct. Currently the data base is supplied either on magnetic or optical media. Two data base versions are available the PDF I and the PDF II.

The PDF I data base contains information on d -spacing, chemical formula, relative intensity, RIR quality information and routing digit. The information is stored in an ASCII format in a file called PDF I data. For search/match purposes most diffraction manufactures are reformatting the file in a more efficient binary format.

The PDF II data base contains full information a particular phase including cell parameters. Scintag's newest search/match and look-up software package is using the PDFII format. Optimized data base format, index files and high performance PC-computers make PDF II search times extremely efficient. The data base format consists of a set number and a sequence number. The set number is incremented every calendar year and the sequence number starts from 1 for every year. The yearly releases of the data base are available in September of each year.

4.6.2 Applications

Identification of phases: the most common use of powder (polycrystalline) diffraction is chemical analysis. This can include phase identification (search/match), investigation of high/low temperature phase, solid solutions and determination of unit cell parameters of new materials.

Polymer Crystallinity:

A polymer can be considered partly crystalline and partly amorphous. The crystalline domains act as a reinforcing grid, like the iron framework in concrete and improve the performance over a wide range of temperature. However, too much crystallinity causes brittleness. The crystallinity parts give sharp narrow diffraction peaks and the amorphous component gives a very broad peak (halo). The ratio between these intensities can be used to calculate the amount of crystallinity in the material.

Residual Stress:

Residual stress is the stress that remains in the material after the external force that caused the stress have been removed. Stress is defined as force per unit area. Positive values indicate tensile (expansion) stress, negative values indicate a compressive stress. The deformation per unit length is called strain. The residual stress can be introduced by any mechanical, chemical or thermal process, e.g. machining, plating and welding.

The principle of the stress analysis by the X-ray diffraction is based on measuring angular lattice strain distributions. That is, we chose a reflection at high 2-Theta and measure the change in the d-spacing with deferent orientations of the sample. Using Hook's law the stress can be calculated from the strain distribution.

Texture Analysis: The determination of the preferred orientation of the crystallines in polycrystalline arrogates is referred to as texture analysis, and the term texture is used as a broad synonym for preferred crystallographic orientation in the polycrystalline material, normally a single phase.

Grain Size Determination: When the size of the individual crystals is less than about 1000 Å, grain size can be determined from line broadening, $B = 0.9\lambda/t \cos\theta$ where B = broadening of diffraction line measured at half its maximum intensity (radians) and t = diameter of crystal particle. All diffraction lines have a measurable breadth, even when the crystal size exceeds 1000 Å, due to such causes as divergence of the incident beam and size of the sample (in Debye cameras) and width of the X-ray source (in diffractometers). The breadth B refers however, to the extra breadth, or broadening, due to the particle-size effect alone. In other words, B is essentially zero when particle-size effect alone. In other words, B is essentially zero when particle-size about 1000 Å.

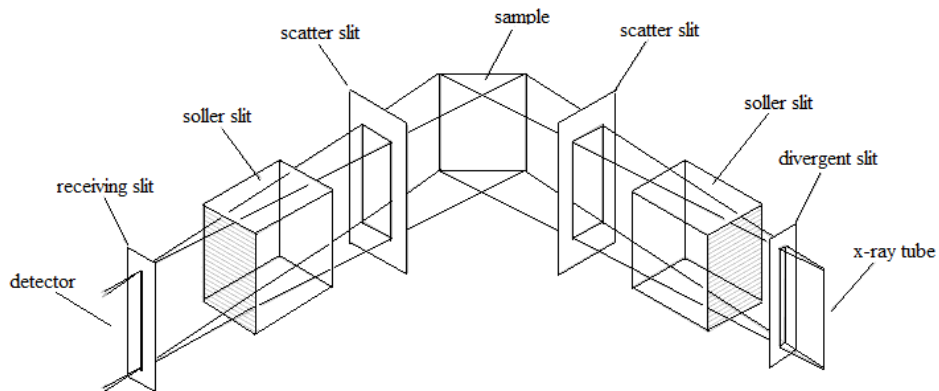


Fig.4.6 Diffractometer Slit System

4.6.3 Philips X'Pert Pro Multipurpose X-ray Diffractometer

The X'Pert PRO diffraction system utilizes a modular system approach to provide performance for applications ranging from routine characterization to in-depth research investigations. The PreFIX (Pre-aligned Fast Interchangeable X-ray Optics) concept enables the diffraction system to be reconfigured in a few minutes without the need for re-alignment to handle different types of analysis. A suite of data analysis software from Philips is available. During X-ray diffraction analysis, X-ray beams are reflected off a specific wavelength, for any given d-spacing (distance between adjacent atomic planes) there are only specific angles at which the exiting rays will be 'in phase' and therefore, will be picked up by the detector producing a peak on the 'diffractogram'. Just like a 'fingerprint', every mineral has its own distinct set of diffraction peak that can be used to identify it.



Fig.4.7 X-ray Diffractometer (model: PW 3040-X'Pert PRO Philips) with high temperature attachment.

The system enables us to do the analysis on phase identification and quantification, as well as crystal structure studies. The specifications of the system are:

- X-RAY SOURCES: 3 kW Copper tube
- OPTICS: focusing and parallel PreFix optics, programmable slits, tunable diffracted beam monochromator.
- DETECTORS: Xe proportional counter and solid state X'cellerator
- SAMPLES STAGES: Single sample holder, 15-sample changer
- VARIABLE TEMPERATURE CAPABILITY: Anton-Parr 77 – 725 K and 300 – 1475 K cameras
- SOFTWARE AND DATABASES: Data collector, X'Pert Plus crystallographic analysis software with Rietveld capability, ProFit line profile analysis software.
- INSTRUMENT STATISTICS: The system uses Cu K_{α} radiation that has a wavelength of 1.54 Å. Analysis are commonly run using a 40 kV 45mA x-ray tube voltage, a 0.04° soller slit, 1° divergence and antiscatter slits, and a 1/2° (for powder) or 1/4° (for clays) receiving slit.

4.6.4 Materials Geometries:

Ring Geometry:

The ideal sample geometry of soft magnetic materials is a ring. This shape is preferable because a ring shape eliminates factors that can distort the magnetic test results. The main source of distortion of test data on soft magnetic materials is usually from air gaps present in the magnetic test circuit. These air gaps lower the apparent permeability of the material, and can be difficult to control. As a ring geometry is continuous path, the magnetic circuit is closed, without any air gaps that cause distortions. In addition, the magnetic path length, which is required to convert the applied current in the sense windings into applied magnetic field is easy to calculate an unambiguous for ring samples.

In many cases, block or rod samples can be machined into a ring specimen for the most accurate magnetic measurements. If this machining process is on a sample, a technique that produces minimal cold working the material is preferred such as wire EDM or laser cutting.

In ring shaped samples, primary windings are wound on the ring to generate a magnetic field in the sample via applied current to the primary windings. A secondary coil is also wound into the ring to inductively measure the magnetic induction of the sample.

Squares, Rectangles, and Others Closed Geometries: In some cases, the soft magnetic material specimen is a rectangular or square geometry, which does not lend itself to be machined into a ring. In these instances, accurate magnetic measurements can still be performed, since the sample geometry creates a closed magnetic circuit. For these measurements, primary and secondary coils are wound into the sample, as with ring measurements. The magnetic path length of the test circuit must be either determined or known in order to convert the applied primary current into applied magnetic field.

Testing Epstein Strips-the Epstein Frame: Epstein strips, which are 3 cm × 25-30 cm long strips, are the overwhelming sample geometry in which core loss of electrical steels and laminations are measured. The strips are measured in a test fixture called an Epstein Frame, which basically reproduces the primary and secondary winding one would use to test a ring sample. Diagrams of an Epstein frame are shown in fig.4.10.

An Epstein frame consists of four primary coils, or H-coils, which magnetize the samples. A multiple of four strips are measured.

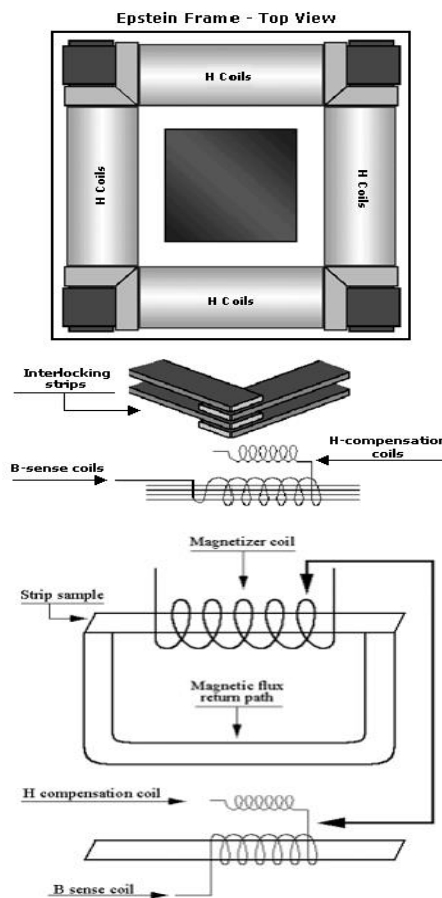


Fig 4.8 Testing individual strip sample

4.6.5 Preparation of the Samples for Complex Permeability measurement:

The amorphous ribbon were wound into toroidal having outer and inner diameters 13 to 15 mm and with the ratio of outer and inner diameters always kept less than 1.2 in order to improve the homogeneity of the applied field, as also to reduce the possibility of an inhomogeneous inductance response. Toroids were wound with 5 turns around to apply AC magnetic fields over a wide range of amplitudes. While measuring the permeability of the amorphous ribbon cores at high frequency, the high electric resistance of these materials generally precludes the troublesome skin effect found in ribbons. However, the cross-section of the amorphous ribbon core to be measured may have to be kept in small order in order to avoid dimensional resonance phenomena. To avoid an increase in resistance owing to skin effect, braided copper wire is used at frequencies higher than 100 kHz.

4.7 Inductance Analyzer:

The 3255B Precision Magnetics Analyzer, as shown in fig.4.11 provides 2-terminal measurement of inductors and transformers over the frequency range 20 Hz to 500 kHz. DC resistance measurements are performed at a drive level of 100 mV. The drive level for AC measurements can be varied from 1 mV to 10 V rms. Automatic level control (ALC) can maintain the drive level of at the component. During AC measurements the 3255B can supply a DC bias current which is variable between 1mA and 1A and when used with external 3265B DC bias units, up to 125 A DC bias current is available.

- The analyzer's measurements, display and control facilities include:
- Spot frequency measurements;
- Multi-frequency measurements at a number of user-defined frequencies;
- Display of actual measurement values;
- Output of measurements results to an Epson-compatible printer;
- Strong of components into bias according to their measured value and/or minor term (option)

All the above functions can be selected via manual front panel control via the GPIB interface for fully-automated high-speed testing. Self-calibration is performed to set calibration constants for signal processing elements in the measurement hardware and signal generation system, and to compensate for components, which drifted with time. To maintain full specified accuracy it should be run at least every three months. To measure the inductance of a component the analyzer should be powered up with the test leads or fixture connected to the

front panel BNC connectors. The analyzer should be operated in Measurement Mode. The measurement may be performed as single shot mode for single measurement or repetitive mode for continuous measurement.



Fig.4.9 Inductance Analyzer (Wayne Kerr) 3255 B

4.8 Initial permeability measurement:

Frequency and temperature dependence of real (μ') and imaginary part (μ'') of complex initial permeability of the as cast and annealed ribbons have been measured using a laboratory built furnace and Wayne Kerr 3255 B inductance analyzer. From this measurement, Curie temperature T_c , of the as cast amorphous phase have been determined. In addition to the measurement of Curie temperature, temperature dependence of initial permeability at different stages of crystallization has been studied for Fe-based soft nanocomposite magnetic materials. Frequency and annealing temperature dependence of complex initial permeability of the amorphous and the annealed samples provide wide information about material property of soft nanocomposite magnetic materials.

Wayne Kerr 3255B inductance provide the value of inductance L and loss factor $D = \tan\delta$. From inductance the value of real part of complex initial permeability μ' can be obtained by using the relation $\mu' = L/L_0$. Here, L is the inductance of the toroid and L_0 is the inductance of the coil of same geometric shape of vacuum. L_0 is determined by using the relation, $L_0 = \mu_0 N^2 S / \pi d$ where $S = m / \pi \rho d$. In these two equations μ_0 is the permeability of the vacuum, N is the number of turns, S is the cross-sectional area of the toroid, d is the average diameter and ρ is the density of the material. The imaginary part of the complex initial permeability can be determined by using the relation $\tan\delta = \mu' / \mu''$.

5.1 Crystallization behavior of $(\text{Fe}_{0.8}\text{Co}_{0.2})_{73.5}\text{Cu}_1\text{Nb}_3\text{Si}_{13.5}\text{B}_9$ alloy

The understanding of crystallization kinetics of magnetic amorphous nanocrystalline alloys has various scientific and technical interest because of the enhancement as well as deterioration of magnetic properties extremely depends on the degree of crystallization. Crystallization kinetics is often determined from Differential Scanning Calorimetry (DSC), Differential Thermal Analysis (DTA) and in magnetic materials from the thermomagnetic analysis (TMA) [5.1-5.2]. Crystallization kinetics have also been studied by a variety of techniques including high resolution transmission electron microscope (HRTEM), in-situ XRD (X-Ray Diffraction), extended X-ray absorption fine structure (EXAFS) measurements and resistance measurements. For the present research on $(\text{Fe}_{0.8}\text{Co}_{0.2})_{73.5}\text{Cu}_1\text{Nb}_3\text{Si}_{13.5}\text{B}_9$ alloy, DTA has been performed to identify the crystallization temperatures as well as activation energy required for crystallization. The X-Ray Diffraction Experiment was undergone to identify the evolution of phases with heat treatment.

5.2 DTA Results of $(\text{Fe}_{0.8}\text{Co}_{0.2})_{73.5}\text{Cu}_1\text{Nb}_3\text{Si}_{13.5}\text{B}_9$ alloy

Crystallization is a non-reversible, exothermic process [5.3]. Calorimetric studies of amorphous alloy provide substantial and fundamental information concerning the kinetics of crystallization. DTA is a direct and effective way to analyze the kinetics of nanocrystalline materials in respect of phase transitions.

The change of composition affects atomic ordering through nucleation and growth of crystallites. Again, the composition of alloy affects both the primary and secondary crystallization phases, because the time needed for the constituent atoms to arrange themselves in a long range order depends on their bond energies [5.4].

Regarding the study of FINEMET as an amorphous alloy, the identification of primary and secondary crystallization temperature carries much significance. Because the nanocrystalline phase comprising of FeCoSi is the product of primary crystallization. Again, identification of the secondary crystalline product is FeCoB is also important because evolution of this phase is detrimental to soft magnetic properties. The separation between these two phases is required to be verified because the ultra soft magnetic behavior expected from the FeCoSi phase can be suitably achieved when boride phases do not overlap with this phase.

The crystallization process is affected by heating rate as well as by composition. To keep the stability of the nanocrystalline alloy to achieve the expected soft magnetic behavior, both the nucleation and growth rate of nanocrystallites must be controlled. To study the effect of

composition on the stability of the amorphous and nanocrystalline alloy, heating rate must be kept constant at any DTA treatment.

5.3 Study of DTA traces of $(\text{Fe}_{0.8}\text{Co}_{0.2})_{73.5}\text{Cu}_1\text{Nb}_3\text{Si}_{13.5}\text{B}_9$ alloy

DTA traces for the amorphous $(\text{Fe}_{0.8}\text{Co}_{0.2})_{73.5}\text{Cu}_1\text{Nb}_3\text{Si}_{13.5}\text{B}_9$ alloy taken in nitrogen atmosphere with heating at the rates of 10-40°C/minute at the step of 10°C with continuous heating from room temperature to 1000°C, are presented in figures 5.1(a)-5.1(d) respectively.

In each of the figures, two exothermic peaks are distinctly observed corresponding to two different crystallization events initiated at temperatures $T_{1,1}$ and $T_{2,1}$ respectively. The primary crystallization temperature $T_{1,1}$ corresponds to evolution of nanocrystalline FeCo(Si) phase which provides the expected soft magnetic properties. The secondary crystallization temperature $T_{2,1}$ corresponds to the boride phases i.e. FeB and/or FeCo-B phase which cause magnetic hardening of the nanocrystalline alloy. Thus, the identification of these two temperatures is necessary to understand the appropriate temperature range for heat treatment in order to achieve the nanocrystalline phase and thereby, suitable range of temperature for application of this alloy.

The temperature gap between $T_{1,1}$ and $T_{2,1}$ are 140°C, 147°C, 143°C, 147°C for the heating rates 10°C, 20°C, 30°C, 40°C respectively. From different investigations [5.5] it was reported that this temperature gap evolves for inclusion of copper in FINEMET type alloys. Since only the product of primary crystallization i.e. the nanocrystalline FeCoSi phase is responsible for the desired ultra-soft magnetic behavior and on the contrary, the secondary crystalline FeB and/or FeCoB phase causes magnetic hardening, so keeping a suitable temperature gap between $T_{1,1}$ and $T_{2,1}$ is important.

The transition from amorphous to crystalline state is an exothermic process. It means both the peaks arise due to release of heat energy at particular temperatures. At that temperature, atoms are arranged in a crystalline periodic order, i.e. in a long range atomic order by consuming heat energy supplied through the process. The first crystallization peak temperature $T_{1,1}$ corresponds to structural relaxation i.e. release of stress initially formed by rapid solidification process. The second crystallization peak temperature $T_{2,1}$ corresponds to recrystallization i.e. reordering of atoms to form another crystalline phase.

From each of the DTA traces, it is obvious that the area under the first crystallization peak is larger than the area covered by the second crystallization peak. In table 5.1 crystallization peak temperatures of two phases ($T_{1,1}$ and $T_{2,1}$) and crystallization onset temperatures of two phases

($T_{1,1}$ and $T_{1,2}$) are given for different heating rates. From the table 5.1 it is noticeable that crystallization temperature range of first phase occurred within 18°C to 30 °C, but this range for the crystallization of the second peak is 9°C to 15 °C. So, it is notable that the crystallization temperature range of the first peak is always larger than that of the second peak. Only the crystallization of FeCoSi is completed during the primary crystallization process but since the crystallization of the boride phases is yet to occur, the heat consumption is observed more during the primary crystallization. Since the crystallization of FeCoSi is completed before the onset of secondary crystallization, the less amount of heat is consumed during rest of the crystallization process, i.e. during the secondary crystallization.

Fig.5.2 represents a combination of all DTA traces of amorphous $(\text{Fe}_{0.8}\text{Co}_{0.2})_{73.5}\text{Cu}_1\text{Nb}_3\text{Si}_{13.5}\text{B}_9$ ribbon. It is observed that the crystallization of each phase has occurred over a wide range of temperatures and that the peak temperatures shift to higher values with the increase of heating rate. That means, it requires more heat energy for the formation of crystalline phases with increasing heating rates.

From Fig.5.2 it is obvious that two crystallization phenomena have taken place within a large temperature gap of around 131°C-134°C, evaluated from the difference between two successive peak temperatures. This temperature gap exists because the clustering of copper atoms initiates the formation of primary crystallization product i.e. FeCoSi at temperature lower than the alloys without cobalt.

If the DTA of samples would be repeated after crystallization, no peak corresponding to crystallization would be observed. This is quite expected because the specimens were subjected to irreversible transformations.

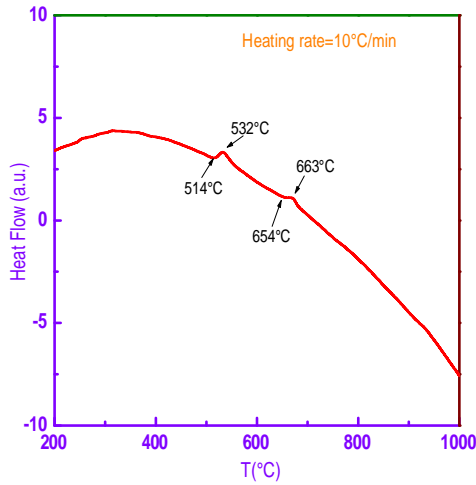


Fig.5.1(a) DTA trace of as cast nanocrystalline amorphous ribbon $(\text{Fe}_{0.8}\text{Co}_{0.2})_{73.5}\text{Cu}_1\text{Nb}_3\text{Si}_{13.5}\text{B}_9$ at the heating rate $10^\circ\text{C}/\text{min}$.

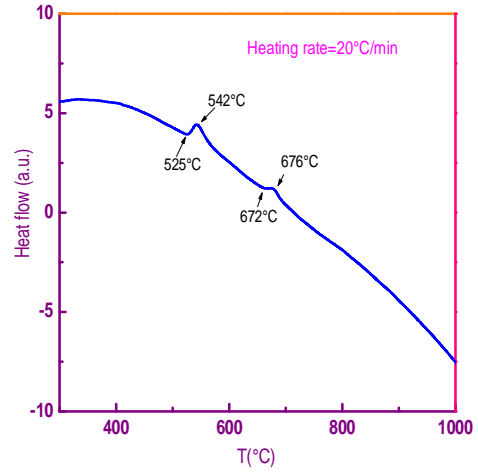


Fig.5.1(b) DTA trace of as cast nanocrystalline amorphous ribbon $(\text{Fe}_{0.8}\text{Co}_{0.2})_{73.5}\text{Cu}_1\text{Nb}_3\text{Si}_{13.5}\text{B}_9$ at the heating rate $10^\circ\text{C}/\text{min}$.

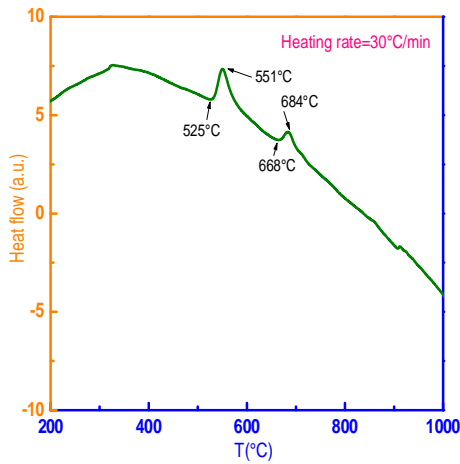


Fig.5.1(c) DTA trace of as cast nanocrystalline amorphous ribbon $(\text{Fe}_{0.8}\text{Co}_{0.2})_{73.5}\text{Cu}_1\text{Nb}_3\text{Si}_{13.5}\text{B}_9$ at the heating rate $30^\circ\text{C}/\text{min}$.

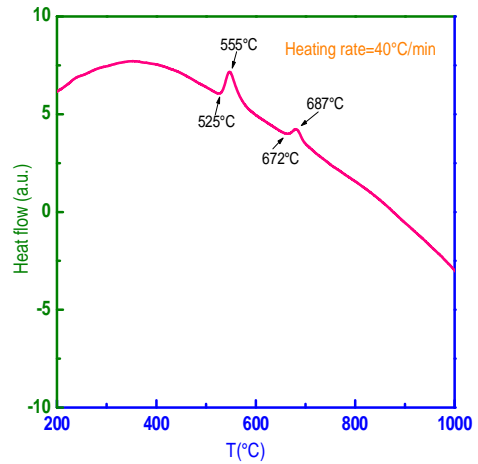


Fig.5.1(d) DTA trace of as cast nanocrystalline amorphous ribbon $(\text{Fe}_{0.8}\text{Co}_{0.2})_{73.5}\text{Cu}_1\text{Nb}_3\text{Si}_{13.5}\text{B}_9$ at the heating rate $40^\circ\text{C}/\text{min}$.

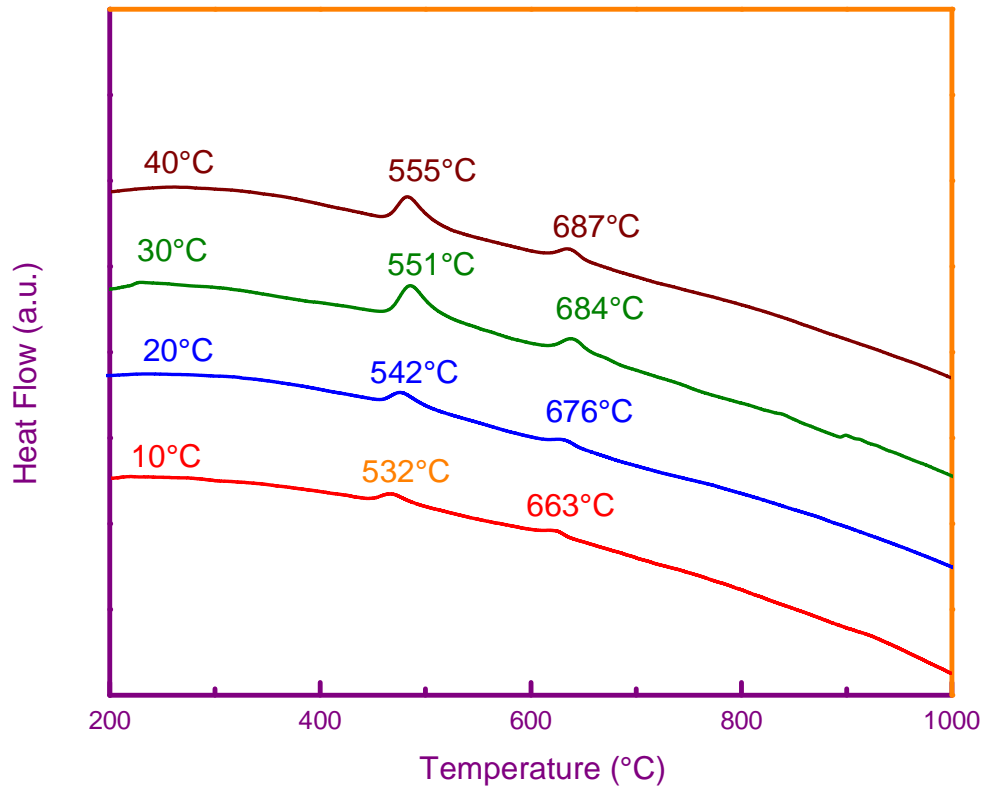


Fig.5.2 Effects of heating rate on DTA traces of nanocrystalline amorphous ribbon $(\text{Fe}_{0.8}\text{Co}_{0.2})_{73.5}\text{Cu}_1\text{Nb}_3\text{Si}_{13.5}\text{B}_9$ at the heating rates of 10- 40°C/min.

Table 5.1 Effects of heating rate on 1st and 2nd crystallization states of the nanocrystalline amorphous ribbon with composition $(\text{Fe}_{0.8}\text{Co}_{0.2})_{73.5}\text{Cu}_1\text{Nb}_3\text{Si}_{13.5}\text{B}_9$.

Heating rate (°C/min)	1 st starting $T_{1,1}$ °C	1 st peak $T_{1,1}$ °C	Temperature range of 1 st state in °C	2 nd starting $T_{1,1}$ °C	2 nd peak $T_{1,1}$ °C	Temperature range of 2 nd state in °C	$T_{1,1} - T_{1,1}$
10	514	532	18	654	663	9	131
20	525	542	17	672	676	4	134
30	525	551	26	668	684	16	133
40	525	555	30	672	687	15	132

5.4 The activation energies for formation of nanocrystalline phase

The activation energy of crystallization of α -FeCo(Si) and FeCoB phases have been calculated using heating rate and crystallization peak temperature following Kissinger's equation,

$$E = -K\beta \ln \frac{1}{1 - X_c} \dots\dots\dots(5.1)$$

where β is the heating rate T_p is the crystallization peak temperature E is the activation energy and K is the Boltzmann constant.

The activation energy of the first crystalline phase α -FeCo(Si) and the second crystalline phase (FeB and/or FeCoB) have been calculated using Kissinger's plots shown in fig.5.3(a) and fig 5.3(b) respectively and the values are given in table 5.2. It is found that first thermal crystallization activation energy (E_1) of α -FeCo(Si) phase is 3.11 eV and that of second FeB and/or FeCoB phase (E_2) is 4.01 eV.

As depicted above, the apparent activation energy E_c in fact is composed of two parts: nucleation and growth with respect to activation energy E_n and E_g respectively. The early stage of crystallization is expected to be dominated by the nucleation process for a crystalline phase. At this stage, formation of Cu clusters leads to a low activation energy for preferential nucleation. However, with the increase of crystalline volume fraction, the Cu-rich regions gradually run out. At the same time, the Nb and B atoms, which are not soluble in the b.c.c. phase, are excluded from the crystallized regions and the surrounding regions rich in Nb and B, in turn block the further growth of grains. The higher the Nb and B contents the stronger is the growth blocking process [5.6]. Consequently, the crystallization activation energy for nucleation and growth increases. Zhang *et al.* found that with the addition of Cu, the crystalline nuclei of α -Fe(Si) segregated and precipitated at a lower temperature. Thus, the formation of Cu-rich regions reduces the activation energy for nucleation E_n of α -FeCo(Si), so that the α -FeCo(Si) phase may nucleate and precipitate preferentially in the Cu-rich regions [5.7].

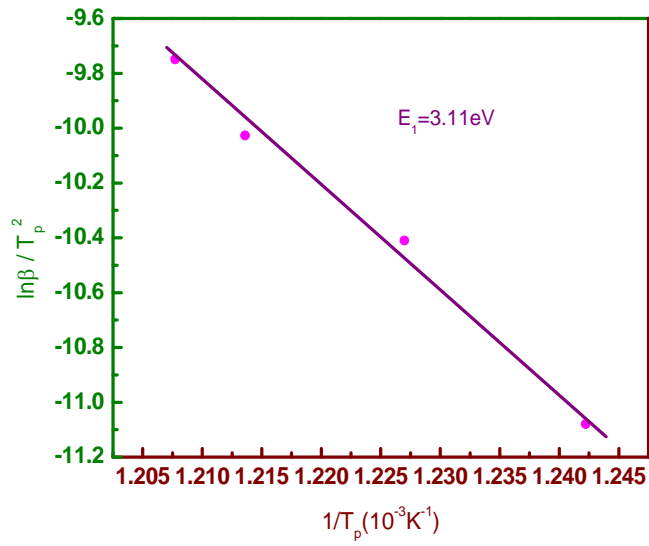


Fig.5.3(a) Kissinger's plot to determine the activation energy of FeCo(Si) phase.

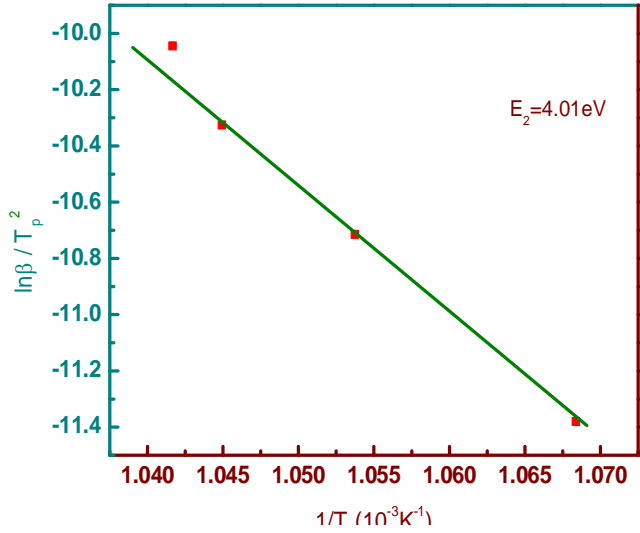


Fig.5.3(b) Kissinger's plot to determine the activation energy of boride phase.

5.5 A comparison between DTA results of $(\text{Fe}_{0.8}\text{Co}_{0.2})_{73.5}\text{Cu}_1\text{Nb}_3\text{Si}_{13.5}\text{B}_9$ alloy and other FINEMETs

The comparative values of DTA results for present alloy and that for original FINEMET sample is given in table 5.2. The results show that the peak temperature corresponding to crystallization decreases with addition of Co [5.8]. This indicates that the crystallization process began at lower temperature which occurs due to existence of cobalt that reduces the glass forming ability [5.9]. So, due to replacement of Co, the evolution of expected nanocrystalline phases (FeCoSi) can be found at a lower temperature. From table 5.2 it is also found that the temperature gap between two successive crystallization is less for the present sample than the alloy without cobalt. Also, it is clear from table 5.2 that the activation energy for formation of first crystalline phase (FeCoSi) is lower than that for the original FINEMET composition which is expected due to replacement of cobalt [5.9]. This result indicates that the role of Co is to facilitate the formation of nanocrystalline α -FeCoSi phase. All these results are very much consistent with the findings of other researches on Co replaced FINEMET samples [5.10-5.11].

Considering DTA at a heating rate of 20°C/min for the alloy composition $\text{Fe}_{73.5-x}\text{Co}_x\text{Cu}_1\text{Nb}_3\text{Si}_{13.5}\text{B}_9$, C. Gómez-Polo *et al.* [5.11] found that the first and second crystallization onset temperatures $T_{1,1}$ and $T_{2,1}$ for alloy without Co ($x=0$) were 553°C and 690 °C respectively, while for alloy with $x=5$, these temperatures were found 543 °C and 687 °C respectively. In our present research for the alloy with 14.7% Co (i.e. $x=14.7$), undergoing DTA at a heating rate of 20°C/min, the first and second crystallization onset temperatures $T_{1,1}$ and $T_{2,1}$ were found at 525 °C and 672 °C respectively. This shows that the crystallization onset temperature decreases as proportion of cobalt content increases in the FINEMET. So, our result is compatible with the previous reports found for Co replaced FINEMETs [5.11].

Table 5.2 Comparison of the activation energies and peak temperatures of original FINEMET and $(\text{Fe}_{0.8}\text{Co}_{0.2})_{73.5}\text{Cu}_1\text{Nb}_3\text{Si}_{13.5}\text{B}_9$ alloy [5.9]:

Heating rate (°C/min.)	$(\text{Fe}_{0.8}\text{Co}_{0.2})_{73.5}\text{Cu}_1\text{Nb}_3\text{Si}_{13.5}\text{B}_9$					$\text{Fe}_{73.5}\text{Cu}_1\text{Nb}_3\text{Si}_{13.5}\text{B}_9$				
	T_1 °C	T_2 °C	$(T_2 - T_1)$ °C	E_1 eV	E_2 eV	T_1 °C	T_2 °C	$(T_2 - T_1)$ °C	E_1 eV	E_2 eV
10	532	663	131	3.11	4.01	550	686	136	3.21	3.81
20	542	676	134			554	700	146		
30	551	684	133			561	708	147		
40	555	687	132			567	715	148		

5.6 Microstructure Analysis of amorphous and nanocrystalline $(\text{Fe}_{0.8}\text{Co}_{0.2})_{73.5}\text{Cu}_1\text{Nb}_3\text{Si}_{13.5}\text{B}_9$ alloy by XRD experiments

XRD experiment was carried out in order to understand the evolution of microstructure with respect to different annealing temperatures for 30 minutes. The appropriately annealed samples were subjected to XRD by using a Philips X'Pert PRO X-ray diffractometer to examine the microstructural evolution as a function of annealing temperature. From the experiment, we obtained results of three kinds of structural parameters including lattice parameter, grain size and silicon content of nanocrystalline FeCo(Si) grains from which we shall further attempt to find out the intrinsic and extrinsic magnetic properties as mentioned in section 2.1 with evolution of microstructures at different annealing temperatures. There must have some effect of structural parameters on soft magnetic properties of the alloy which we shall try to explain afterwards.

Lattice parameters for all the annealed samples have been determined from (110) diffraction peak using formula $a_0=d\sqrt{2}$, while grain size have been calculated using equation (5.4) Silicon content of the Fe(Si) nanograins was calculated from the established quantitative relationship between lattice parameter and Si-content in Fe-Si alloys by Bozorth [5.12]. All the results of θ , d-values, full width at half maxima (FWHM) of the intensity peak corresponding to (110) planes, Grain size D_g and Si content from XRD analysis are listed in table 5.3.

Table 5.3 Experimental XRD data of $(\text{Fe}_{0.8}\text{Co}_{0.2})_{73.5}\text{Cu}_1\text{Nb}_3\text{Si}_{13.5}\text{B}_9$ alloy for as cast and annealed at different annealing temperatures for 30 minutes.

Temperature in °C	θ (degree)	D(Å)	FWHM	a_0 (Å)	D_g (nm)	Si (at%)
500	22.77	-	3.78	-	2.281007	-
525	22.54	1.99997	0.561	2.828385	15.34416	21.40695
550	22.5668	1.99982	0.53	2.828173	16.24481	21.50606
575	22.6074	2.00094	0.526	2.829756	16.37317	20.76607
600	22.61455	2.00014	0.661	2.828625	13.02986	21.29463
625	22.61305	1.99996	0.78	2.828371	11.04185	21.41356
650	22.5702	1.99678	0.678	2.823873	12.69906	23.51461
700	22.5755	2.00304	0.338	2.832726	25.77932	19.37858

5.7 Identification of phases by XRD experiment

The XRD patterns for the alloy $(\text{Fe}_{0.8}\text{Co}_{0.2})_{73.5}\text{Cu}_1\text{Nb}_3\text{Si}_{13.5}\text{B}_9$ annealed at temperatures 475°C, 500°C, 525°C, 550°C, 575°C, 600°C, 625°C, 650°C and 700°C each for 30 minutes are presented in fig 5.4.

It is evident from fig.5.4 when the sample annealed below 500°C, i.e. at 475°C, it exhibited only one broad peak around $2\theta=45^\circ$ at the position of d_{110} reflection which is generally known as diffuse hallow. This diffuse hallow indicates the amorphous nature of the sample. It means at the annealing temperature below 500°C, no crystalline peak has been detected. So, the onset of crystallization temperature determined from these results is 500°C.

The value of FWHM of the peak at the annealing temperature, 500°C is 3.78, which for 525°C is 0.561. For the higher annealing temperatures, the FWHM value is getting smaller. It shows that crystallization occurs to a good extent at the annealing temperature 525°C. The crystallization onset temperatures from DTA experiment for different heating rates were found in the range of 514°C to 525°C, which shows a good consistency with the XRD results.

Due to annealing at 500°C, the first crystallization peak was found at an angle 45.53°. But from the XRD data, no evidence of Si content was found to be partitioned in the crystalline part at that temperature. It reveals that α -FeCo is the first crystalline phase to segregate out in the system during crystallization process, which is also found by Mössbauer spectra in several investigations [5.13].

Investigation by Mössbauer study [5.14] have been identified that addition of Co causes alteration of disordered DO_3 type structure of FeSi grains, occurred in classical nanocrystallite FINEMET, into FeCo(Si) solid solution of low silicon concentration. For annealing at higher temperatures i.e. 525°C, 550°C, 575°C, 600°C, 625°C, 650°C and 700°C, the FeCo(Si) phases were found at the lower values of 2θ at 45.08°, 45.13°, 45.21°, 45.23°, 45.23°, 45.14° & 45.15° respectively with 100% peak intensity on (110) line. The other two fundamental peaks corresponding to α -FeCo(Si) on (200) and (211) diffraction line for annealing temperatures at and above 525°C is obtained in this figure. But due to their low intensity, they are not clearly visible before 550°C annealing. The balance of composition is maintained by the distribution of amorphous phase in the system.

From DTA result it is expected that FeCoB phase would form beyond 650°C. But the formation of crystalline phase other than FeCo(Si) in the XRD pattern has not been detected for T_a upto 700°C for the sample as expected from the DTA analysis of $(\text{Fe}_{0.8}\text{Co}_{0.2})_{73.5}\text{Cu}_1\text{Nb}_3\text{Si}_{13.5}\text{B}_9$. Absence of Fe-B phase in XRD spectra is possibly due to very

small volume fraction of boride phases (Fe_3B , Fe_2B , Fe_{23}B_6 and/or $(\text{FeCo})_{23}\text{B}_6$) [5.9, 5.15, 5.16] present.

The XRD patterns illustrated in fig. 5.4 reveal that the differences in the Bragg's peak as well as the intensity of the fundamental reflections becomes gradually stronger as the temperature of the heat treatment increases. This increase in the sharpness of the intensity peaks with the annealing temperature indicates that crystalline volume fraction has been increased and also, grains become coarser with increased crystallinity.

From Mössbauer spectra of the thermally treated samples of Co substituted FINEMETs, evidence of α -FeCo and $(\text{FeCo})_3(\text{BSi})$ crystalline phases might be found along with iron oxides (α - Fe_2O_3 and λ - Fe_2O_3) of less than 1% of the total composition [5.5]. Reason of oxide formation lies in the fact of performing annealing in air atmosphere. It should be demonstrated herewith that the addition of refractory elements [Nb, Ta, Mo etc.] delays the occurrence of crystallization and oxidation and increases the thermal stability of the amorphous alloy [5.5]. In spite of addition of refractory elements it should be suggested that the heat treatment should be done in an inert (non-reactive) atmosphere to avoid oxidation and other reactions.

The systematic but negligible shift of peak towards the larger angles with increasing temperature indicates that lattice parameter of the phase gradually decreases due to the increasing of silicon content of the α -FeCo phase. Both the decrease in lattice parameter and increase in intensity of the fundamental peak with increasing annealing temperature suggest that Si atom diffuse most intensively into the b.c.c. FeCo with increase of annealing temperature. The diffusion of Si in b.c.c. α -FeCo is finally found as the nanocrystalline b.c.c. FeCo(Si) lattice which is identified by XRD and therefore we see the increase in intensity due to increase of the crystalline part in the alloy.

The lattice parameter, the silicon contents in b.c.c. nanograins and the grain size of b.c.c. grain can easily be calculated from the fundamental peak of (110) reflections.

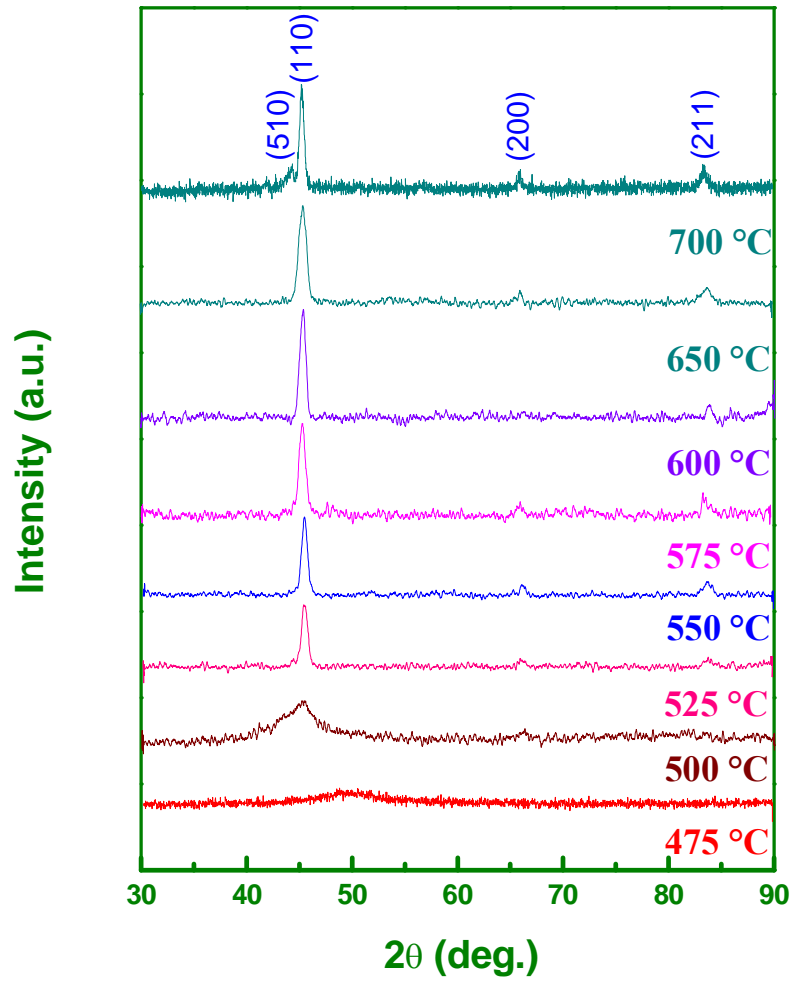


Fig.5.4 XRD patterns of $(\text{Fe}_{0.8}\text{Co}_{0.2})_{73.5}\text{Cu}_1\text{Nb}_3\text{Si}_{13.5}\text{B}_9$ alloys for as cast and annealed at different annealing temperatures for 30 minutes.

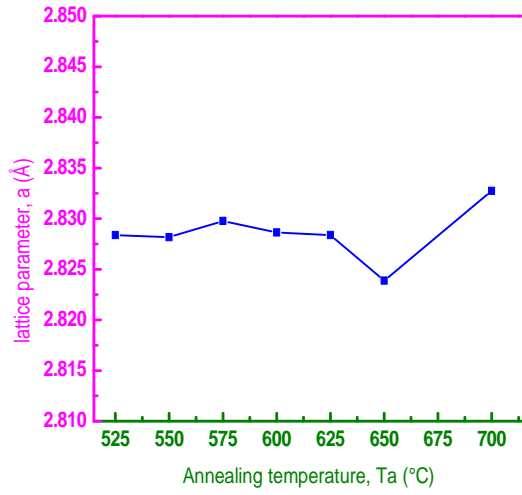


Fig.5.5 Variation of lattice parameter with annealing temperature

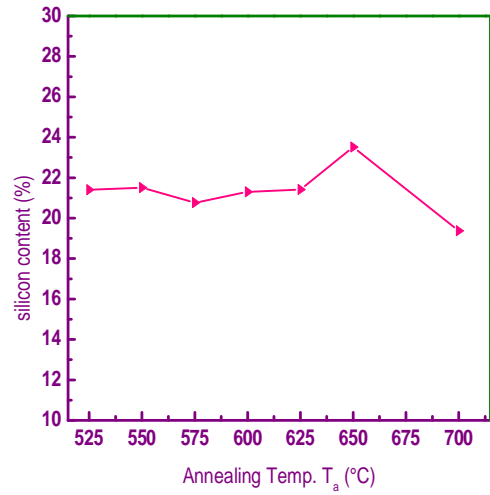


Fig.5.6 Variation of Si% with annealing temperature

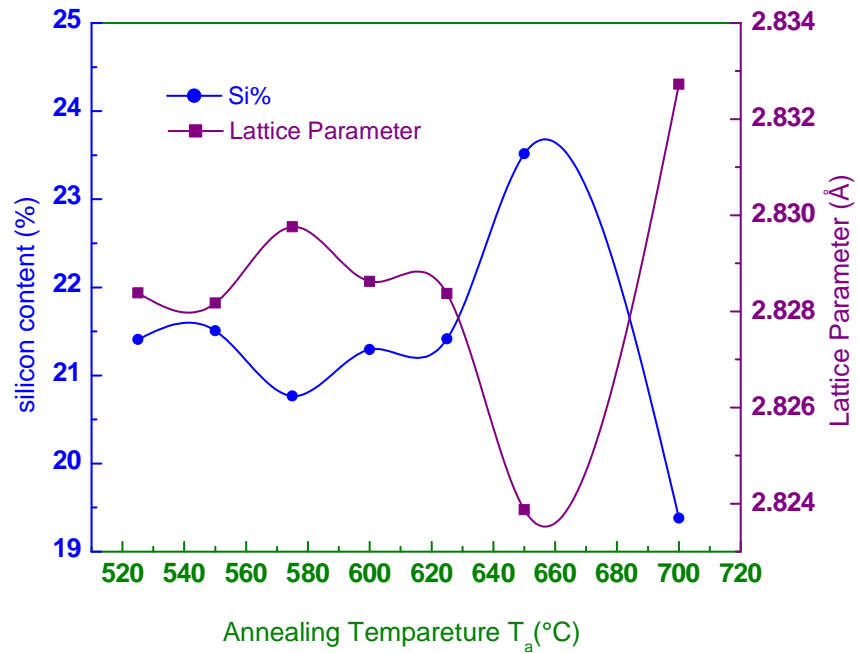


Fig.5.7 Variation of lattice parameter and Si% with annealing temperature

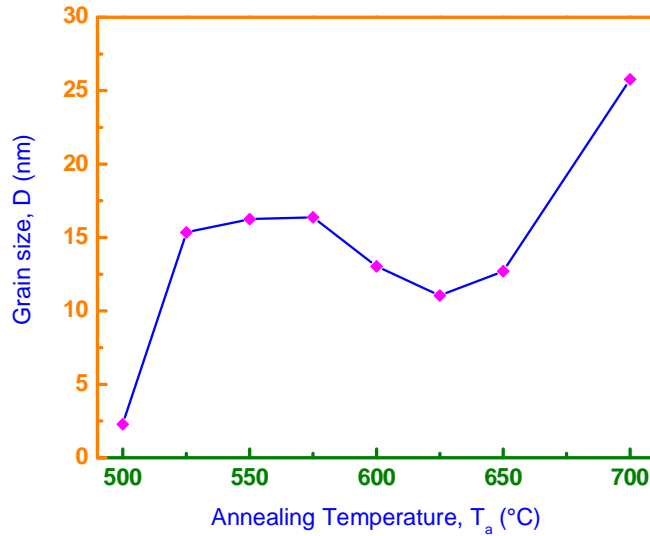


Fig.5.8 Variation of grain size with annealing temperature

5.8 Lattice parameter determination

Lattice parameter of crystalline b.c.c. Fe-Si was determined at different annealing temperatures of the experimental alloys. Structure of the b.c.c. FeCoSi grains depends on the annealing temperature. Normally lattice parameter of an alloy composition is determined by Debye-Scherrer method after extrapolation of the diffraction curve for the sample. Generally for the accurate determination of the lattice parameter, a number of fundamental peaks are required, but in this type of tailored materials upon crystallization only the major fundamental peak (110) is used in calculation of a_0 [5.8]. We have, therefore, determined the lattice parameter using only that particular reflection using equation

$$2d\sin\theta = \lambda \text{ and } a_0 = d\sqrt{2} \dots \dots \dots (5.2)$$

Where $\lambda = 1.54178 \text{ \AA}$ is the wavelength of Cu-K α radiation and a_0 is determined lattice parameter of the grain, d is the inter-planar spacing and θ is the diffraction angle.

For every steps lattice parameter was determined with an error estimated to be $\pm 0.001 \text{ \AA}$ using equation 5.2 and all the values are listed in table 5.3 and the pattern of change in lattice parameter with respect annealing temperature is presented in fig.5.5.

In fig. 5.5 the variation of lattice parameter as a function of annealing temperatures, T_a for 30 minutes annealing are presented for the sample under study at annealing temperatures ranging from 500°C- 700°C.

Fig. 5.5 shows that, with the increase in annealing temperature, the lattice parameter was not changed notably up to the annealing temperature 625°C. At 650°C, lattice parameter was decreased significantly. The reason of decrease in lattice parameter can be explained from the fact of relative atomic sizes of the main two constituents of the b.c.c. phase i.e. Fe and Si. The lattice parameter of pure Fe is 2.8664 Å. But the lattice parameters at various annealing temperatures for the present alloy are significantly less than that of pure Fe. Si having a smaller atomic size compared to Fe, diffuses in the α -FeCo lattice during annealing at different temperatures which results in a contraction of α -FeCo lattice. Thus, the newly formed substitution solid solution of α -FeCo(Si) during the crystallization process has a smaller size comparing to the α -FeCo lattice. So, the more diffusion of Si, there should be more contraction of the α -FeCo lattice and thereby, the decrease of lattice parameter. Decrease of lattice parameter with annealing temperature suggests negligible peak shift due to stacking fault as in general no peak is observed experimentally.

In the present sample, there is a partial replacement of Co for Fe. Researchers found that the average TM-TM (Transitional Metal) near-neighbor distance decreases with the increase of Co concentration [5.17] which results in the decrease of lattice parameter comparing to the original FINEMET. As the presence of Co produces a decrease in the lattice parameter, the actual Si content would be less [5.17] in the crystalline phase. So the contribution of Si content for the change of lattice parameter would be less. This might be the reason for which the variation in lattice parameter with annealing temperature is not so obvious for the present sample comparing to original FINEMET up to 625°C. However, the decrease in lattice parameter is evident at or around 650°C when the diffusion of Si became easier at that temperature due to stress-relief in microstructure caused by heat-treatment.

When the sample is annealed above 650°C, the increase of lattice parameter with subsequent decrease of Si content, as showed in figs. 5.5-5.6 indicates that silicon diffuses out of α -FeCo(Si) grains for which the size of α -FeCo lattice is regained. Thus there happened a recrystallization of the α -FeCo(Si) grains beyond 650°C. This result is compatible with those reported for similar composition [5.18].

The behavior of lattice parameter with annealing temperature provides interesting information about compositions of nanocrystalline phase formed by primary crystallization. All the

obtained values of lattice parameter in this work are always significantly smaller than that of pure α -Fe. Hence it could be speculated that the metalloid elements of alloy has been dissolved in the b.c.c. FeCo phase. But the metalloid element Boron is practically insoluble in α -Fe ($\lll 0.01$ at.%) and the solubility of Cu and Nb are very low (<0.2 at.% Cu; <0.1 at.% Nb; only above 550°C) [5.19]. Hence the nanocrystalline phase in this experiment for sample $(\text{Fe}_{0.8}\text{Co}_{0.2})_{73.5}\text{Cu}_1\text{Nb}_3\text{Si}_{13.5}\text{B}_9$ consists essentially of Fe, Co and Si only.

5.9 Silicon content in nanograins

Lattice parameter measurements give the hint about a non-negligible solute content establishing the fact that the b.c.c.-ferromagnetic phase consists of iron, cobalt and silicon essentially.

Crystalline nanograins having composition FeCo(Si) were formed in the amorphous ribbon through heat treatment. The saturation magnetostriction and magnetocrystalline anisotropy of α -FeCo are sensitive to the content of the solute. It is therefore important to determine the concentration of Fe, Co and Si in the nanograin. As lattice parameter of the nanograins have been measured for different heat treatment conditions, it is easy to calculate the Si content in the nanograin from the quantitative relationship between lattice parameter (a) and Si content (Si%) developed by Bozorth [5.12]. The simple equation to calculate Si content from lattice parameter is:

$$b = -467a_0 + 1342.8 \dots \dots \dots (5.3)$$

where b is at.% Si in nanograins, a_0 is the lattice parameter of the nanograins.

The silicon contents of the alloy $(\text{Fe}_{0.8}\text{Co}_{0.2})_{73.5}\text{Cu}_1\text{Nb}_3\text{Si}_{13.5}\text{B}_9$ at different annealing temperatures 500°C , 525°C , 550°C , 575°C , 600°C , 625°C , 650°C and 700°C for 30 minutes are found to be in the range of 19.38% to 23.52%. All these results are presented in table 5.3 and the pattern of change in silicon content with respect to annealing temperature is presented in fig.5.6.

Fig.5.6 shows the percentage of Si in α -FeCo(Si) phases with the gradual increase of annealing temperature attaining a maximum value of 23.52 at.% at 650°C . It is notable that Si contents in the nanocrystallites at different annealing temperatures are higher than Si content of the amorphous precursor which is 13.5%. This increase of Si content in the crystalline phase with increasing annealing temperature can be explained by the fact that the element Si from the amorphous phase diffuses into α -FeCo space lattice during crystallization process to form α -FeCo(Si) nanograins. This means that the crystallization of this alloy is a diffusion controlled

process with temperature as controlling parameter. So, higher annealing temperature results in more diffusion of Si enriching the FeCo(Si) nanograins. The fact of increase in intensity of diffraction peaks and besides, increase in Si content in nanograins with increase of annealing temperature indicates that the diffusion of Si results in the increase of nanocrystalline volume fraction in the amorphous precursor. The percentage of partitioned Si in the nanocrystalline α -FeCoSi phase is maximum at $T_a = 650^\circ\text{C}$. After 650°C , decrease in Si content is observed which can be explained by the fact that at higher temperatures silicon diffuses out of nanograins due to recrystallization corresponding to formation of boride phases which is consistent with the result of other Finemets [5.18].

Figure 5.7 presents the inverse relationship between lattice parameter and silicon content. This kind of relation between lattice parameter and Si content was observed in the reports [5.18] which is verified in present work effectively. At the initial stage of crystallization lattice parameter first decreases with increase of silicon content, because silicon diffuses in the b.c.c. Fe-Co phase, to form the soft nanocrystalline FeCo(Si) phases. Such decrease of lattice parameter with increase of silicon content prevails up to 650°C , beyond which the lattice parameter increases with decrease of silicon content. This is the sequence of recrystallization when silicon diffuses out initiating formation of boride phases.

5.10 Grain size determination

In 1963 Kneller *et al.* [5.20] studied on nanometric grains. They found that the magnetic properties of isolated grains change drastically as their size is reduced to the nanometer range. When these nanometric grains are consolidated to form a nanostructured material, the magnetic properties are largely determined by the grain size and the exchange interaction between the adjacent grains.

Herzer [5.21] successfully established the theoretical explanation on the grain size dependence of superior soft magnetic properties based on his Random Anisotropy Model (RAM) after the pioneer experimental invention of FINEMET alloy by Yoshizawa *et al.* [5.22]. One member of the FINEMET family is the Sample $(\text{Fe}_{0.8}\text{Co}_{0.2})_{73.5}\text{Cu}_1\text{Nb}_3\text{Si}_{13.5}\text{B}_9$ which is under investigations of the present work. Thus an important part of the present study was to determine the nanocrystalline grain size.

Grain size of all annealed samples of the alloy composition was determined using Scherrer method [5.23]. Grain size was determined from XRD patterns of (110) reflections for different annealing temperature at constant annealing time 30 min. from which grain size was determined using the formula,

$$D_g = \frac{\lambda}{4\beta \sin^2 \theta} \dots \dots \dots (5.4)$$

where $\lambda=1.54178 \text{ \AA}$ is the wavelength of Cu-K $_{\alpha}$ radiation, θ is the diffraction angle and β is the full width at half maximum (FWHM) of diffraction peak in radian for different steps of annealing temperature.

Instrumental broadening of the system was determined from θ - 2θ scan of standard Si. At the position of (110) reflections, the value of instrumental broadening was found to be 0.07° . This value of instrumental broadening was subtracted FWHM value of each peak. Asymmetrical broadening of the peak due to stacking fault of b.c.c. crystal was corrected by using computer software. Total broadening of the peak due to twin fault was considered negligible in the present case. All determined grain size was values for every steps of heat treatment are listed in table 5.3.

From fig. 5.4 it is clear that at lower annealing temperature 500°C , the FWHM of the peak is large and with the increase of annealing temperature, the value of FWHM are getting smaller. The peaks are, therefore becoming sharper with the shifting of peak position towards higher 2θ value. The peak shifts indicate the change of the values of silicon content of the nanograins and therefore, the change of the values of lattice parameter of nanograins.

Fig. 5.8 and table 5.3 shows that at 500°C , the grains are smaller in size i.e. $\sim 2 \text{ nm}$ since no evidence of Si partitioning was found at that annealing temperature and hence grain growth is still not so evident. The increase of annealing temperature initiates partitioning of Si in the b.c.c. FeCo phase and thus grain growth due to formation of nanocrystalline b.c.c. FeCoSi grains. In the range of annealing temperatures 525°C - 650°C , the grain size remains in the range of 11 to 16 nm corresponding to soft magnetic b.c.c. FeCoSi phases. Above 650°C , grains grow rapidly and attain a maximum value of 26 nm at 700°C indicating formation of FeB and/or FeCoB phases. Formation of boride phase is detrimental to soft magnetic properties as showed in further experiments and also supported by different reports [5.2]. These facts reveal that heat treatment temperature should be limited within 550°C - 650°C to obtain optimum soft magnetic behavior, which will be clear from further experiments in this thesis.

The formation of the nanometric microstructure corresponding to the grain growth with the increase of T_a is ascribed to combined effects of Cu and Nb and their low solubility in iron. Cu which is insoluble in α -FeCo, segregates prior to or at the very beginning of nanocrystallization forming Cu-rich clusters and the nucleation of FeCo(Si) grains is thought to be multiplied by clustering of Cu which stands as the reason for the grain growth at the initial stage of

crystallization. On the other hand the rejection of Nb at the crystal interface (due to their higher crystallization temperature) causes hindrance to grain growth for which the change in grain size is not so obvious constant up to 650°C. The increase of nucleation density caused by Cu as well as inhibition of grain growth by Nb results in homogeneous distribution of nanograins in the surrounding amorphous matrix. Our result corresponds well with the reported results of Rubinstein *et al.* [5.24].

In fact, implementation of more improved technique e.g. APFIM, SEM or TEM might explain this obtained result from XRD better. In the XRD method much larger area is subjected for investigation. Consequently, problems of statistical significance might arise since a small number of large grains might cause an overestimation of grain size and textured growth (which could arise due to ribbon shape amorphous precursor) possesses a special problem. As mentioned earlier in the simple Scherrer formula, the width of a given reflection is used for grain size determination which underestimates the grain size as the strains evidently present in the nanostructures are not taken into account. However, the shortcomings regarding evaluation of structural parameters does not affect much in correct estimation of the parameters and still XRD is a widely used experiment for investigation of microstructures of crystals.

5.11 Dynamic Magnetic properties of $(\text{Fe}_{0.8}\text{Co}_{0.2})_{73.5}\text{Cu}_1\text{Nb}_3\text{Si}_{13.5}\text{B}_9$ alloy

Dynamic magnetic properties of as-quenched nanocrystalline samples with composition $(\text{Fe}_{0.8}\text{Co}_{0.2})_{73.5}\text{Cu}_1\text{Nb}_3\text{Si}_{13.5}\text{B}_9$ has been measured as a function of frequency in the range from 1 kHz to 500 kHz. Permeability measurements were performed on toroid-shaped samples at frequency of 1 kHz to 500 kHz and an applied ac driving field ($\approx 0.5\text{A/m}$) to ensure the measurements of initial permeability. Frequency spectrum of real part of initial permeability, relative loss factor and relative quality factor are analyzed. The measurements have been done for as cast sample and samples annealed at different annealing temperatures with constant annealing time. In order to avoid experimental error due to fluctuation in ribbon thickness and thermal treatment, just one piece of each ribbon has been measured at room temperature after subsequent annealing temperatures at constant annealing time. Magnetic properties of amorphous nanocrystalline magnetic materials are strongly dependent on its annealing temperature [5.2]. In the present work, initial magnetic permeability of the toroidal samples annealed at different temperatures are measured to understand their soft magnetic properties and correlation with the micro structural features which are obtained from XRD analysis.

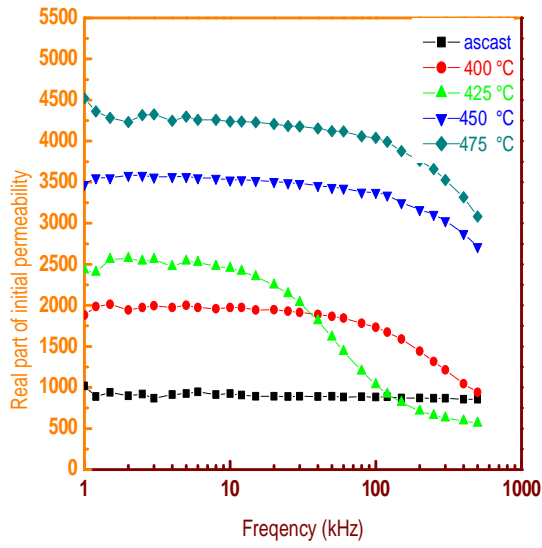


Fig. 5.9(a)

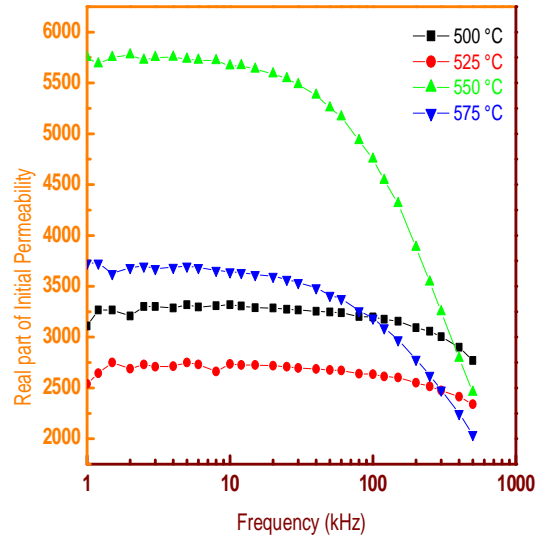


Fig. 5.9 (b)

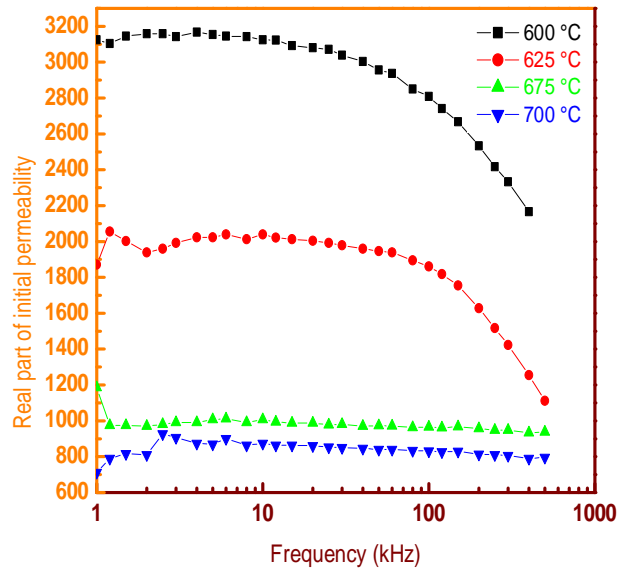


Fig.5.9(c)

Figs.5.9(a, b, c) Frequency dependent real part of complex initial permeability at different of $(\text{Fe}_{0.8}\text{Co}_{0.2})_{73.5}\text{Cu}_1\text{Nb}_3\text{Si}_{13.5}\text{B}_9$ alloy at annealing temperatures for constant annealing time 30 minutes.

5.12 Frequency dependence of initial permeability

In order to correlate the microstructural features on the soft magnetic properties of the alloy under study, magnetic initial permeability of toroidal shaped samples annealed at different temperatures are measured with very low field. Magnetic properties of the soft magnetic materials are mainly determined by the domain wall mobility especially in the range of irreversible magnetization.

One of the main purpose of this experiment was to determine empirically the optimum annealing temperature for the constant annealing time of 30 minutes, corresponding to maximum permeability, constancy of permeability and maximum frequency range over which the sample can be used as a soft magnetic material.

In figs. 5.9 (a, b, c) frequency dependence of real part of complex initial permeability μ' up to $f = 500$ KHz has been presented for as cast sample and the sample annealed at temperatures 400°C to 700°C for a constant annealing time of 30 min. The general characteristic of the curve is that μ' remains fairly constant up to some critical frequency characterized by the onset of resonance connected with the loss component. At critical frequencies, μ' drop rapidly. The low frequency value of μ' generally increases with the increase of annealing temperature. In association with higher value of low frequency permeability, the frequency at which resonance occurs appears at lower frequency. This shows that the high permeability ribbons can be used as core materials only in a limited frequency range.

This trend of increase of low frequency permeability is observed up to the annealing temperature of 550°C . For the annealing temperature of 575°C , the low frequency permeability decreases and for 700°C it drops to a very low value.

The change in low frequency permeability with annealing temperature is presented in figs.5.9(a)-(c) and combindly presented in fig.5.10. From the figures, it is observed that the low frequency value of initial permeability increases with the increase of annealing temperature attaining the maximum value at the annealing temperature of 550°C . When the annealing temperature is higher than 550°C , initial permeability decreases rapidly. This decrease of initial permeability may be attributed to the stress developed in the amorphous matrix by growing crystallites. This act as pinning centers for the domain wall mobility. The growing crystallites are far apart from each other representing small volume fraction that cannot be exchange coupled and the anisotropy cannot be averaged resulting in weak intergrain magnetic coupling. At this temperature, the initiation of crystallization takes place.

The feature of the permeability spectrums corresponding to annealing temperatures at and above 500°C shows that the low frequency value of initial permeability increases with the increase of annealing temperature and attains the maximum value at the annealing temperature of 550°C. When the annealing temperature is higher than 550°C, low frequency value of initial permeability decreases rapidly. From the combined graph presented by fig.5.10, the maximum value of low frequency permeability is shown clear for the annealing temperature of 550°C, the value of which is 5750. Thus, to obtain the highest permeability, the sample heat-treated at 550°C is most suitable. In other words, the best soft magnetic property can be found at the annealing temperature of 550°C for this alloy.

For samples annealed above 550°C, the initial permeability drops to lower value drastically. The probable reason might be evolution of boride phases and the nonmagnetic f.c.c phases including Cu clusters. These leads to the increase of magnetocrystalline anisotropy to a high value, which essentially reduces the local exchange correlation length weakening the intergranular magnetic coupling as a result of which magnetic hardening takes place.

The frequency response of the samples at different temperatures can in general be explained in terms of the growth of crystallites and their size distributions. The increase in permeability due to annealing indicate that the high temperature annealing remove the local defects as created during preparation of sample, which facilitates the domain wall movement.

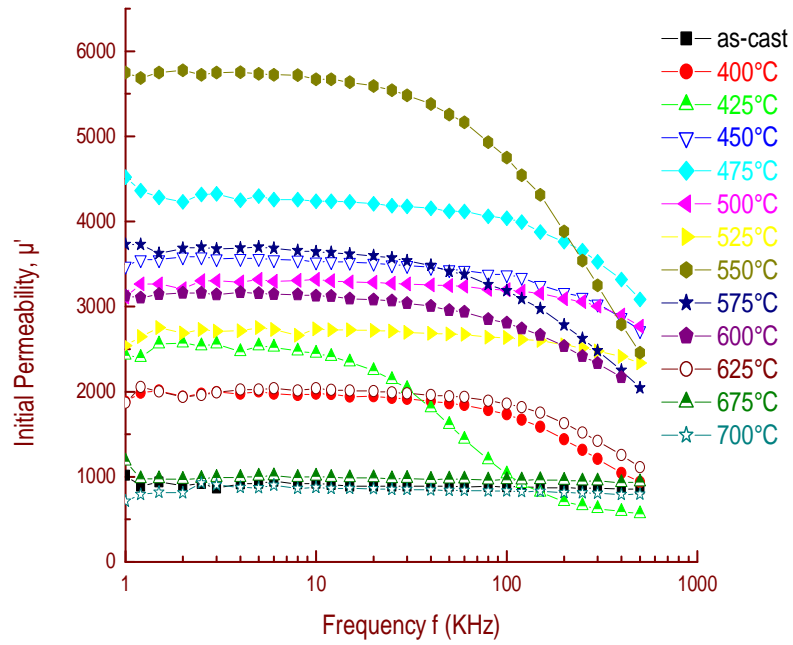


Fig.5.10 Frequency dependence of real part of complex initial permeability of $(\text{Fe}_{0.8}\text{Co}_{0.2})_{73.5}\text{Cu}_1\text{Nb}_3\text{Si}_{13.5}\text{B}_9$ alloy at different annealing temperatures for constant annealing time 30 minutes.

5.13 Loss factors and relative quality factor

Loss factor, $\tan\delta$ and relative quality factor, $\mu'Q$ are important parameters for the soft magnetic materials from the application point of view. Minimum loss factor and maximum relative quality factors are preconditions for achievement of good soft magnetic properties in FINEMET type alloys.

The loss factor is given by the ratio of real and imaginary parts of the complex permeability, i.e. $\tan\delta = \mu''/\mu'$. The loss factor arises due to eddy current loss as well as for the phase lag of the spin reorientation with respect to external field. Since the net loss factor, $\tan\delta$ found for this nanocrystalline material is quite complex, it is difficult to separate out the contribution from the eddy current loss and the phase lag of the spins with respect to the fields. The loss factor in general is found to be high for the entire sample at low frequency as well as for high frequency.

The increase of the loss factor with annealing temperature indicates that longer annealing time causes further growth of crystallites and their stability. As a result, loss is controlled mainly by interaction between grains, the size of grains and grain orientation as such the specimen thickness becomes important. The precipitation of very small percent of particles improves the high frequency losses and permeability. The phase lags between induced flux and the applied field increases but with more consistency with the increase of frequency.

The origin of loss factor can be attributed to various domain defects, which include non-uniform and non-repetitive domain wall motion, domain wall bowing, localized variation of flux density, and nucleation and annihilation of domain walls. At low frequencies, magnetic losses are controlled by hysteresis caused by irreversible magnetization process and at high frequency, the flux penetration becomes low and loss is mainly controlled by interaction between the grains as well as eddy current.

It is well known that upon optimal annealing, nanocrystalline alloys display minimum loss and very high relative quality factor $\mu'Q$ having the order of magnitude 10^5 - 10^6 . In this experiment, optimal annealing temperature is determined through successive annealing of the alloys from 400°C to 700°C.

5.14 Frequency dependence of Relative Quality Factor

Relative quality factor is given by the ratio of real part of initial permeability, μ' and loss factor $\tan\delta$ i.e. $\mu'/\tan\delta$ or $\mu'Q$. The high value of the relative quality factor exhibits a good soft magnetic property.

The frequency dependence of relative quality factor of the different annealed samples are shown in figures. 5.11(a)-(c). The relative quality factor is controlled by the real part of the initial complex permeability. The relative quality factor curve initially rises with respect to increasing frequency and after reaching a peak value, it decreases. The peak value for each curve represents the best soft magnetic behavior for the corresponding annealing temperature. Beyond the peak value, the quality factor is found to decrease which may be attributed to increase of loss components. This gives a choice of optimal annealing temperature for attaining best soft magnetic properties.

With the increase of annealing temperature, the relative quality factor first increases up to 550 °C after which it decreases. The highest value of quality factor is found for the sample annealed at 550°C, which also indicates the best heat treatment temperature to obtain the highest value of quality factor. From all curves, it is noticeable that the higher values of the relative quality factor in general lie within the range of 50 kHz to 500 kHz frequencies. Thus, the frequency range for application area might be chosen.

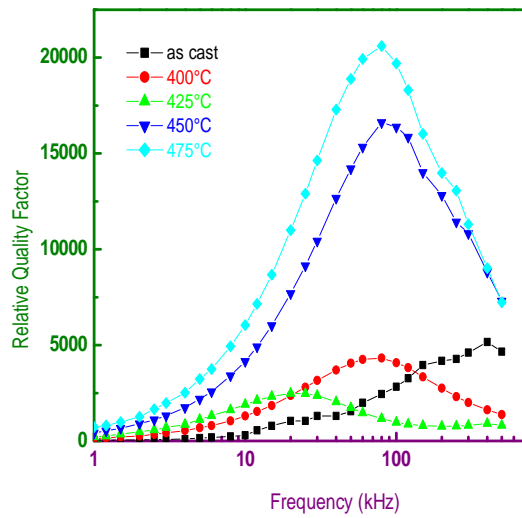


Fig. 5.11(a)

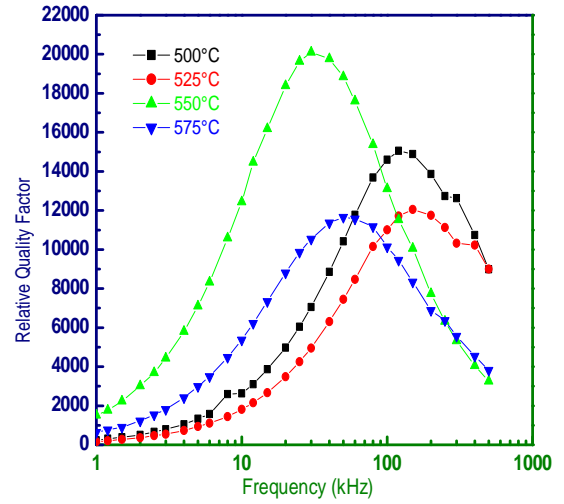


Fig. 5.11(b)

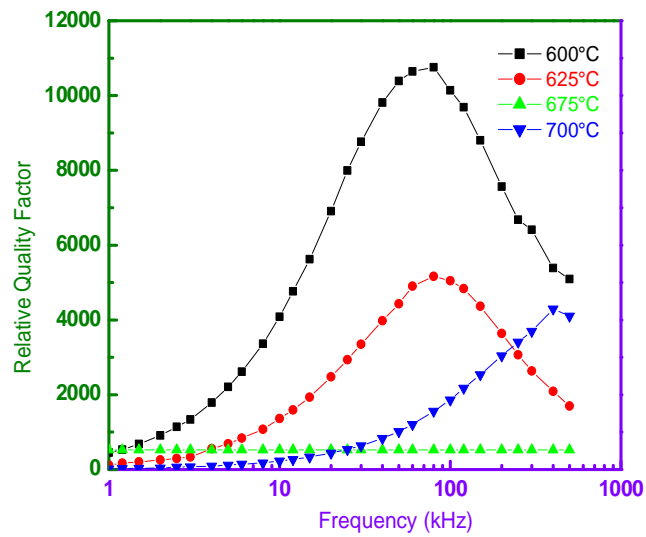


Fig. 5.11(c)

Fig.5.11(a,b,c) Frequency vs Relative Quality factor for as cast and different annealing temperatures for constant annealing time 30 minutes.

5.15 Curie Temperature Measurements of $(\text{Fe}_{0.8}\text{Co}_{0.2})_{73.5}\text{Cu}_1\text{Nb}_3\text{Si}_{13.5}\text{B}_9$ alloy

Nanocrystalline amorphous ribbons of composition $(\text{Fe}_{0.8}\text{Co}_{0.2})_{73.5}\text{Cu}_1\text{Nb}_3\text{Si}_{13.5}\text{B}_9$ have been chosen for the determination of the Curie temperature (T_c) using the μ vs. T curves. Temperature dependence of ac initial permeability of the samples subjected to a heating rate $5^\circ\text{C}/\text{min}$. and the constant frequency of 10 kHz has been used for exciting current from a signal generator as shown in figures 5.12(a)-(c). Numerical values of T_c s for different annealing temperatures for the fixed frequency 10 kHz are presented in table 5.4.

T_c is a basic quantity in the study of magnetic materials. It corresponds to the temperature at which a magnetically ordered material becomes magnetically disordered, i.e., becomes paramagnet. T_c also signifies the strength of the exchange interaction between the magnetic atom. In figures 5.12(a)-(c), initial permeability increase with increase of temperature and has the maximum value at a certain point. Beyond this point, there is a decrease in the permeability. This temperature is known as the Curie temperature T_c . The well defined values of T_c obtained from our measurements support the fact that in spite of chemical and structural disorder, ferromagnetic glasses have well defined magnetic ordering temperature. The sharp fall of the initial permeability is observed at 421°C for the amorphous $(\text{Fe}_{0.8}\text{Co}_{0.2})_{73.5}\text{Cu}_1\text{Nb}_3\text{Si}_{13.5}\text{B}_9$ sample.

From fig. 5.12(a) it is shown for the as cast $(\text{Fe}_{0.8}\text{Co}_{0.2})_{73.5}\text{Cu}_1\text{Nb}_3\text{Si}_{13.5}\text{B}_9$ sample that no notice about effects in the glassy materials is produced at temperature below 421°C [5.25]. It is interesting to note that the sharp fall of the permeability at T_c enables us to determine T_c unambiguously. The sharp fall of the permeability at T_c indicates that the material is quite homogeneous from the point of view of amorphosity of the materials. It is also observed from this curve that the permeability increases with the temperature and attains a maximum value just before T_c which we consider as Hopkinson effect.

5.16 Temperature dependence of initial permeability:

In fig. 5.12(a)-(c) the real part of complex initial permeability μ' has been presented as a function of annealing temperature T_a at a fixed frequency of 10 kHz. The curve reveals strong dependence of initial permeability on annealing temperature.

For samples as cast and annealed from 400°C to 475°C , as shown in fig.5.12(a), permeability passes through a maximum just before a sharp fall to near zero with the manifestation of Hopkinson effect characterizing the ferro-paramagnetic transition which is compatible with reported results [5.8]. From variation of μ' with temperature for toroidal samples annealed at 400°C to 475°C , Curie temperature of the residual amorphous matrix determined from the

maximum value of $d\mu'/dt$ are 426°C, 430°C, 433°C and 439°C for the sample annealed at 400°C, 425°C, 450°C and 475°C respectively.

Practically the accurate determination of T_c of amorphous material is really difficult due to irreversible component of the structural relaxation like long range internal stress, topological and chemical short-range order. This structural relaxation without destroying the amorphous state may influence T_c . Therefore during the measurement of T_c the heating rate has been adjusted in such a way that no substantial relaxation takes place. However, the Curie temperature estimated from the curves presented in figures 5.12(a)-(c) for the as cast and annealed samples in the amorphous state has been given in table 5.4.

At higher measuring temperatures above Curie temperature of the amorphous matrix, μ_1^{11} permeability decreases to very low value. Franco *et al.* [5.26] have demonstrated superparamagnetic behavior is a general feature of these nanocrystalline alloys. The practical requisite for observing superparamagnetic relaxation in the nanocrystalline alloys is the absence of interaction between the nanograins in the residual amorphous matrix. At $T > T_c^{am}$ very low value of permeability for the samples annealed at 425°C suggests that superparamagnetic type of behavior may be presented. Where the exchange interaction between the nanograins mainly occurs via sufficiently thick paramagnetic interfacial amorphous matrix in which the nanocrystallites possessing high magnetic moments are dispersed. When the measuring temperature approaches the Curie temperature of the intergranular amorphous phase, the exchange coupling between the crystallites is largely reduced. As a consequence, the initial permeability drops down to a very low value.

As shown in fig. 5.12(b), at the annealing temperature of 525°C the permeability drops to a lower value. This is the temperature around which the initiation of crystallization takes place. Since newly growing crystallites are still far apart from each other having weak intergrain magnetic interaction among themselves, μ' has a low value at that temperature. With further increase of temperature, sharp increase in permeability takes place up to $T_a = 550^\circ\text{C}$ due to decrease of average anisotropy of the nanograins with a retaining value of magnetization [5.27]. It is noteworthy that the temperature corresponding to the increase of permeability at higher measuring temperature coincided with the temperature at which coercivity vanishes [5.28]. The increase of permeability with increasing annealing temperature corresponds to increase of volume fraction of the crystallites, which may be attributed to the decrease of the thickness of the amorphous grain boundary favoring the interaction between the nanograins

compatible with the previous observation [5.26] and is limited by Curie temperature of the b.c.c. FeCo(Si) nanograins.

The feature which can be observed from fig.5.12(b)-(c) is that as the annealing temperature is above crystallization temperature i.e. 500°C to 700°C, the sharpness of fall to lower values of permeability is smeared out with the appearance of a tail in the high temperature region. This might be an indication of loss of homogeneity of the sample for initiation of nucleation i.e. for proceeding of crystallization. These results in a good agreement with those previously reported for the FINEMET composition [5.26].

From the results of temperature dependent permeability for samples annealed at 500°C to 700°C, the grain coupling is largely but not completely interrupted above the Curie temperature of the amorphous matrix. A system in which the magnetic coupling between particles is significant and prevents superparamagnetic relaxations is termed as superferromagnetism by S. Mørup [5.29]. The precise coupling mechanism for this type of behaviour at $T > T_c^{am}$ may be explained in terms of exchange penetration through thin, paramagnetic intergranular layer and/or dipolar interactions [5.30].

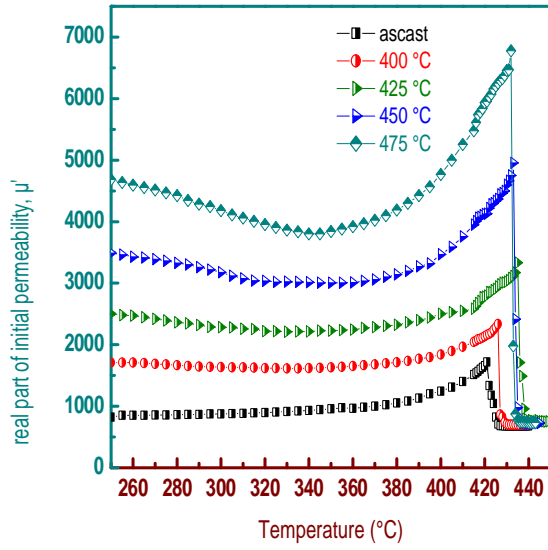


Fig.5.12(a)

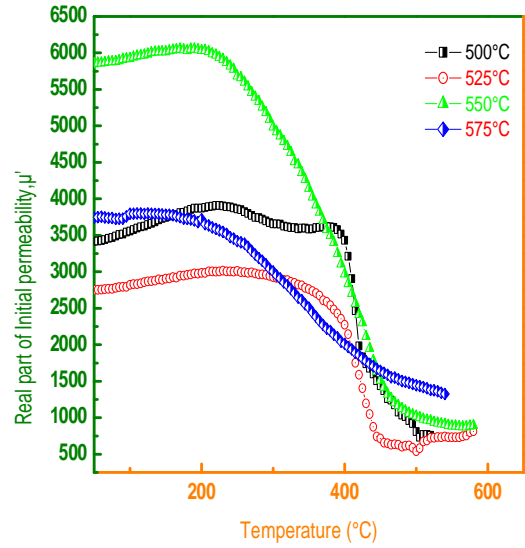


Fig. 5.12(b)

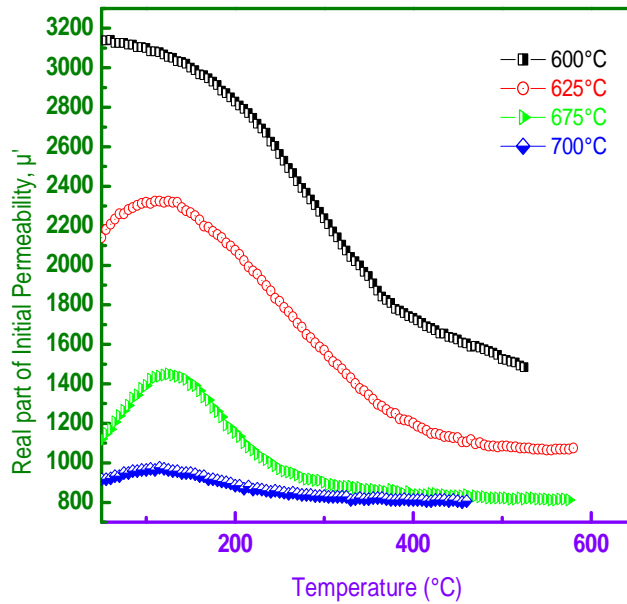


Fig. 5.12(c)

Fig.5.12(a, b, c) Temperature dependent real part of complex initial permeability of $(\text{Fe}_{0.8}\text{Co}_{0.2})_{73.5}\text{Cu}_1\text{Nb}_3\text{Si}_{13.5}\text{B}_9$ alloy at different annealing temperatures for constant annealing time 30 minutes.

5.17 The initial permeability vs relative loss factor:

In fig.5.13, annealing temperature dependence of real part of initial permeability μ' and relative loss factor $\tan\delta/\mu'$ has been presented for frequency $f=10$ kHz in order to demonstrate evolution of magnetic softness with annealing treatment. When annealed at temperatures below the onset of crystallization i.e. 500°C , an increase of initial permeability with annealing temperature was observed due to irreversible structural relaxation of the amorphous matrix i.e. stress relief, increase of packing density by annealing out microvoids and changing the degree of chemical disorder. Further increase of annealing temperature leads to a sharp increase of permeability due to crystallization of $\alpha\text{-FeCo(Si)}$ phase and increased volume fraction of nanograins coupled via exchange interaction resulting in a reduction of anisotropy energy. An enhancement of initial permeability with annealing temperature was observed for the annealing temperature of 550°C . The relative loss factor $\tan\delta/\mu'$ decreases up to an order of 10^{-2} at this temperature. Beyond this temperature μ' drops to a lower value drastically and $\tan\delta/\mu'$ increases. The decrease of permeability may be attributed to the stresses developed in the amorphous matrix by the growing crystallites which act as pinning centre for the domain walls constraining domain wall mobility as well as intergrain magnetic couplings since the growing crystallites are far apart from each other representing small volume fraction that cannot be exchange coupled and anisotropy cannot be averaged. This condition indicates evolution of boride phases that lead to the increase of anisotropy to a high value that essentially reduces the local exchange correlation length weakening the intergranular magnetic coupling as a result of which magnetic hardening takes place [5.30].

The relative loss factor $\tan\delta/\mu'$ has been reduced by three orders of magnitude for the optimum annealed sample than for as cast sample. For the annealing temperature of 550°C , μ' attains a value of about 5.75×10^4 while the relative loss factor $\tan\delta/\mu'$ decreases to a value of about 0.0662×10^2 . This very high initial permeability and extremely low magnetic losses of the optimized nanocrystalline alloys are due to the drastic reduction in the local anisotropy randomly averaged out by the exchange interactions due to the formation of nanometric grains smaller than the ferromagnetic exchange length, as identified by x-ray diffraction of this study. It has been correlated with the observation of TEM by Buttino *et al.* [1.24] where they have found grains with 2 nm appears to be embedded in a residual amorphous matrix at the early stage of crystallization which is almost similar to the result found for present composition. This is also compatible with the phase transition temperature obtained from differential thermal

analysis. Devitrification proceeds with increasingly coarser microstructure for higher annealing temperature as a result of which permeability decreases.

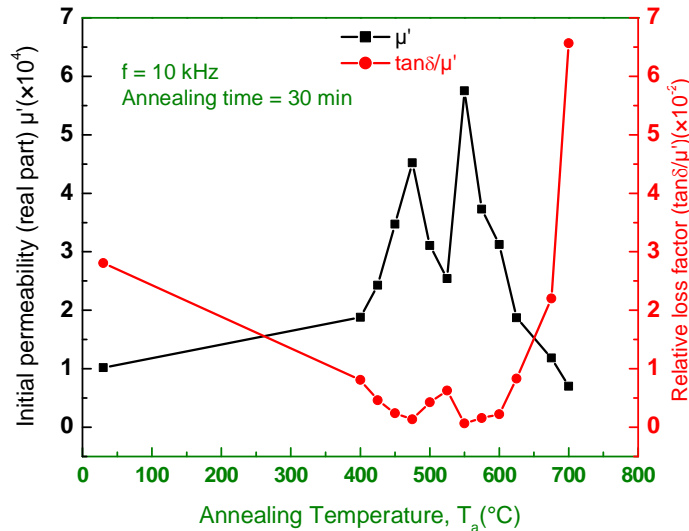


Fig.5.13 Annealing temperature (T_a) dependence of initial permeability(μ') and relative loss factor ($\tan\delta/\mu$) for $(\text{Fe}_{0.8}\text{Co}_{0.2})_{73.5}\text{Cu}_1\text{Nb}_3\text{Si}_{13.5}\text{B}_9$ alloy, for constant annealing time 30 minutes measured at 10 kHz frequency.

5.18 The variation of Curie temperature with respect to annealing temperature:

From table 5.4 it can be observed that the Curie temperature of the as cast and amorphous ribbon of composition $(\text{Fe}_{0.8}\text{Co}_{0.2})_{73.5}\text{Cu}_1\text{Nb}_3\text{Si}_{13.5}\text{B}_9$ is 421°C. Enhancement of the Curie temperature occurs when the sample is annealed in the temperature range 400-500°C. From X-ray diffraction, no crystalline phase was observed before the annealing temperature of 500°C. Enhancement of Curie temperature below crystallization temperature occurs because of irreversible structural relaxation as mentioned above. From previous researches, it has been observed that the annealing treatment leads to the increase in packing density of atoms [5.31]. Increase in packing density of atoms might have significant contribution in the enhancement of Curie temperature in the amorphous state. Above the crystallization temperature, Curie temperature of the amorphous matrix decreases significantly. The probable reason of decreasing the Curie temperature of the amorphous phase when annealed at and above the crystallization temperature is that the amorphous matrix is depleted with iron and the relative amount of Nb in the amorphous matrix increases, which weakens the exchange interaction resulting in a decrease of Curie temperature of the amorphous matrix.

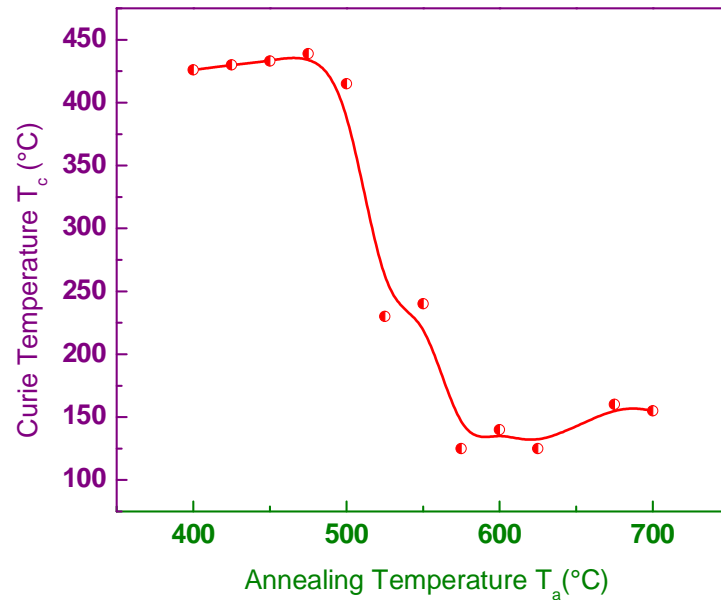


Fig.5.14 Variation of Curie temperature with respect to Annealing temperature

5.19 Enhancement of Curie temperature due to cobalt addition:

The Curie temperature of the as cast i.e. amorphous $(\text{Fe}_{0.8}\text{Co}_{0.2})_{73.5}\text{Cu}_1\text{Nb}_3\text{Si}_{13.5}\text{B}_9$ alloy was found at 421°C , while for the original amorphous FINEMET of composition $\text{Fe}_{73.5}\text{Cu}_1\text{Nb}_3\text{Si}_{13.5}\text{B}_9$ it was found at 354°C [5.8]. This shows that there is an enhancement of Curie temperature due to addition of cobalt. The physical causes may be explained as follows: Curie temperature of Fe is 770°C and that of cobalt is 1127°C . Replacement of Co for Fe would enhance the Curie temperature because of the much higher magnetocrystalline anisotropy of Co which increases thermal stability of this type of alloy.

Table -5.4 Curie temperatures obtained at different annealing temperatures.

Annealing Temperature, T_a(°C)	Curie Temperature, T_c (°C)
400	426
425	430
450	433
475	439
500	415
525	230
550	240
575	125
600	140
625	125
675	160
700	155

Nanocrystalline amorphous ribbon of the FINEMET family with nominal composition $(\text{Fe}_{0.8}\text{Co}_{0.2})_{73.5}\text{Cu}_1\text{Nb}_3\text{Si}_{13.5}\text{B}_9$ has been studied to find out the correlation between microstructural features and soft magnetic properties dependent on various stages of nanocrystallization during the isothermal annealing around the crystallization temperature of their amorphous precursors. The ribbon was produced by melt spinning technique with 20-25 μm thickness. Crystallization behavior and magnetic properties have been studied by DTA, XRD and inductance analyzer.

The crystallization behavior of the sample was investigated by DTA and XRD experiments. The onset of crystallizations was determined by DTA. The amorphous and annealed samples were examined by XRD to identify the microstructure of the sample. To understand the magnetic properties, frequency and temperature dependent permeability, loss factor and relative quality factor was evaluated with toroid-shaped samples in as cast condition and also for different annealing temperatures. The magnetic phase transition temperature, i.e. Curie temperature was obtained from these experiments. From the systematic investigation on the crystallization, structural and magnetic properties, the following conclusions can be outlined:

(1). DTA experiment was performed for four different heating rates 10, 20, 30 and 40°C/min. in steps of 10°C/min up to a temperature of 1000°C. DTA reveals the primary and secondary crystallization onset temperatures with the manifestation of two well-defined exothermic peaks corresponding to nanocrystalline FeCoSi and FeB and/or FeCoB phases respectively. The knowledge of crystallization temperatures has been fruitfully utilized during the isothermal annealing of these amorphous ribbons for nanocrystallization, which ultimately controls the magnetic properties of FINEMET alloys.

For heating rates 10, 20, 30 and 40°C/min., the onset of the first crystalline phases ($T_{1,1}$) were found 514°C, 525°C, 525°C and 525°C and that of the second crystalline phases ($T_{2,1}$) were found 654°C, 672°C, 668 °C and 672°C respectively.

The activation energy values of the first crystalline phase α -FeCo(Si) and the second crystalline phase (FeB and/or FeCoB) calculated using Kissinger's plots were 3.11 and 4.01eV. The temperature difference between two crystallization peaks ($T_{1,1} - T_{2,1}$) is found to exist around 131°C-134°C. This peak separation temperature is important for the stability of primary crystallization phase FeCoSi, against detrimental boride phases which is necessary for fabrication of high quality inductors.

(2). The amorphous stage of as cast ribbons has been confirmed by XRD. The evolution of nanocrystallites of b.c.c. FeCo(Si) and also boride phases (Fe_3B , Fe_2B , Fe_{23}B_6 and/or $(\text{FeCo})_{23}\text{B}_6$) were identified in this experiment. From this experiment, three kinds of structural parameters including lattice parameter, grain size and silicon content of nanocrystalline FeCo(Si) grains were obtained using the line broadening of fundamental peaks (110) from XRD patterns as affected by annealing around the crystallization temperatures.

From XRD experiment, the crystallization onset temperature for the sample is found between 500°C to 525°C which coincides well with the value obtained from DTA. XRD study reveals the boride phase at around 700°C for the sample which is also consistent with DTA result.

The grain sizes determined for the sample using the formula $D_g = \frac{1.11}{11111}$ varied from ~ 2 to 26 nm for the annealing temperature from 500°C to 700°C , where $\lambda = 1.54178 \text{ \AA}$ is the wavelength of Cu- K_α radiation, θ is the diffraction angle and β is the full width at half maximum (FWHM) of diffraction peak in radian for different steps of annealing temperature.

The lattice parameter a_0 was determined using the formula $a_0 = d\sqrt{2}$, with an error estimated to be $\pm 0.001 \text{ \AA}$ where d is the inter-planar spacing. The silicon content was calculated from lattice parameter using the formula $b = -467a_0 + 1342.8$, where b is at% Si in nanograins.

The lattice parameter and Si% shows an inverse relationship indicating that Si diffuses in the crystalline phase at the initial stage of crystallization at 525°C for which Si% increased with decrease in lattice parameter that continued up to 650°C . Beyond 650°C , Si% is found to decrease with increase in lattice parameter, that indicates diffusion of Si out of nanograins, indicating recrystallization i.e. formation of boride phases.

(3). Magnetic initial permeability of nanocrystalline/amorphous ribbon strongly depends on annealing temperature. The improvement in the in the soft magnetic properties can be ascribed to the much refined grain structure in the range of ~ 2 to 26 nm obtained at various temperatures during annealing. When alloys were annealed for 30 minutes at various temperatures, the maximum initial permeability (μ') were observed at $T_a = 550^\circ\text{C}$ for $(\text{Fe}_{0.8}\text{Co}_{0.2})_{73.5}\text{Cu}_1\text{Nb}_3\text{Si}_{13.5}\text{B}_9$ alloy. The temperature corresponds to a maximum initial permeability and lowest losses. A sharp increase of initial permeability at this temperature indicates that μ' is related to structural relaxation. Further increase of annealing temperature deteriorated the μ' . The high permeability is attributed to the drastic decrease of effective anisotropy due to nanometric grain size effect and strong intergrain magnetic coupling. The

sample showed magnetic hardening at 575°C to 700°C with very low value of μ' due to stress developed during the initiation of crystallization.

The highest value of real part of initial permeability is achieved for the sample annealed at 550°C, for which the least value of relative loss factor was found. So, 550°C is the most suitable heat treatment temperature from the application point of view in case of the present alloy as a soft magnetic material.

(4). For technological uses of nanocrystalline materials at elevated temperature and for thermo-magnetic stability it is important to look for compositions that give higher values of Curie temperature (T_c). The T_c is 421°C for as-cast amorphous $(\text{Fe}_{0.8}\text{Co}_{0.2})_{73.5}\text{Cu}_1\text{Nb}_3\text{Si}_{13.5}\text{B}_9$ alloy. Enhancement of T_c was observed for samples annealed below the crystallization temperature due to structural relaxation. T_c of interfacial amorphous phase has been found to decrease for samples when annealed above crystallization temperatures due to the depletion of Fe and increase of relative amount of Nb in the residual amorphous phase.

(5). The $(\text{Fe}_{0.8}\text{Co}_{0.2})_{73.5}\text{Cu}_1\text{Nb}_3\text{Si}_{13.5}\text{B}_9$ alloy has been synthesized by addition of Co by 14.7% in the original FINEMET composition. The change in properties as a result of addition of Co found in our experiment includes:

- i) Achievement of soft magnetic nanocrystallites in the amorphous alloy in lower heat treatment temperature than the original FINEMET
- ii) Enhancement of Curie temperature comparing to the original FINEMET sample indicates the improvement of thermo-magnetic stability due to Co addition.

There is much scope for further research in controlling the magnetic characteristics by changing composition and heat treatment. Certain important parameters like magnetic anisotropy, temperature dependence of magnetization and magnetostriction can be studied in detail for a better understanding of microstructure-property relationship of FINEMET type alloys.

References for Chapter 1

- [1.1] Köhler, F., “*Rapid-Quenched Magnetosoft Materials*”, October 2006
- [1.2] Gleiter, H., “*Nanocrystalline Materials*”, Progress in Materials Science, 33 (1989) 223-315
- [1.3] Yoshizawa, Y., Oguma, S., and Yamauchi, K., “*New Fe-based soft magnetic alloys composed of ultrafine grain structure*”, J. Appl. Phys. 64 (10) 1988, 6044-6046
- [1.4] Makino, A., Inoue, A., Masumoto, T., “*Low core losses and magnetic properties of $Fe_{85-86}Si_{1-2}B_8P_4Cu_1$ nanocrystalline alloys with high B for power applications*”, Mater. Trans. 36, 924 (1995).
- [1.5] Vlasák, G., Švec, P., Duhaj P., “*Evolution of magnetostriction in $Fe_{73.5}Ni_xCu_1Nb_3Si_{13.5}B_9$ ($x=0, 10, 20, 30, 40$) alloy in the course of transformation*”, J. Mag. Mag. Mat. 254–255 (2003) 225–227
- [1.6] Ohnuma, M., H. Ping, D., Abe, T., Onodera, H., Hono, K., Yoshizawa, Y., “*Optimization of the microstructure and properties of Co-substituted Fe–Si–B–Nb–Cu nanocrystalline soft magnetic alloys*”, J. Appl. Phys., Vol. 93, No. 11, 2003, 9186-9194
- [1.7] Müller, M., Grahl, Mattern, N., Kühn, U., Schnell, B., “*The influence of Co on the structure and magnetic properties of nanocrystalline FeSiBCuNb and FeZrBCu-based alloys*”, J. Magn. Mag. Mat. 160 1996 284
- [1.8] Gómez-Polo, C., Marín, P., Pascual, L., Hernando, A., and Vázquez, M., “*Structural and magnetic properties of nanocrystalline $Fe_{73.5}Co_xSi_{13.5}B_9CuNb_3$ alloys*”, Phys. Rev. B, vol. 65 The American Physical Society, 2001 024433(1-6)
- [1.9] Geraci, Zs., Kane, S. N., Greneche, J. M., Varga, L. K. and Mazaleyrat, F. “*Study of structural and magnetic properties of $(Fe_{100-x}Co_x)_{73.5}Si_{13.5}B_9Nb_3Cu_1$ alloys*” Phy. Stat. Sol. (C) vol.1 issue 12 2004 3603-3607
- [1.10] Kolano-Burian, A., Kolano, R., Kulik, T., Frenec, J., “*Magnetic properties of Co doped FINEMET at elevated temperature*”, Rev. Adv. Mater. Sci. 18(2008) 545-548.
- [1.11] Onuma, M., H. Ping, D., Abe, T., Onodera, H. and Hono, K., “*Optimization of the microstructure and properties of Co-substituted Fe–Si–B–Nb–Cu nanocrystalline soft magnetic alloys*”, J. Appl. Phys., 93(11) 2003 9186-9194.
- [1.12] Herzer, G., “*Grain Size dependence of coercivity and permeability in nanocrystalline ferromagnets*” IEEE Trans. Mag. 26(5) 1990 1397-1402
- [1.13] Yoshizawa, Y. and Yamachi, K. “*Fe-based soft magnetic alloys composed of ultrafine grain structure*”, Mater. Trans. JIM. 31 (1990a) 307

- [1.14] Noh, T. H., Lee, M. B., Kim, H. J., Kang, I. K. “*Relationship between crystallization process and magnetic properties of Fe-(Cu-Nb)-Si-B amorphous alloys*”, J. Appl. Phys. 67 (1990) 5568.
- [1.15] Kataoka, N., Matsunaga, T., Inoue, A., Masumoto, T., “*Soft magnetic properties of b.c.c. Fe-Au-X-Si-B (X=early transition metal) alloys with fine grain structure*”, Mater. Trans. JIM , 30 (1989), 947-950
- [1.16] Müller, M., and Matern, N., “*The influence of refractory element additions on the magnetic properties and on the crystallization behaviour of nanocrystalline soft magnetic Fe-B-Si-Cu alloys*” J. Mag. Mater. 136, (1994) 79
- [1.17] Inoue, A., Kobayashi, K., Kanerhira, J. and Masumoto, T., “*Mechanical properties and thermal stability of (Fe-Co-Ni)-M-B (M=IV,V and VI group transition metals) amorphous alloys with low boron concentration*”, Sci. Rep. Res. Inst. Tohoku Univ.(1981),vol. A 29, p.331-342
- [1.18] Suzuki, K., Makino, A., Kataoka, N., Inoue, A. and Masumoto, T., “*Soft magnetic properties of nanocrystalline b.c.c. Fe-Zr-B and Fe-M-B-Cu (M=transition metal) alloys with high saturation magnetization*” J. Appl. Phys., 70(10) (1991) 6232
- [1.19] Suzuki, K., Makino, A., Inoue, A. and Masumoto, T. “*Low core losses of nanocrystalline Fe-M-B (M=Zr, Hf, or Nb) alloys*” J. Appl. Phys., (1993), vol. 74, p.3316
- [1.20] Herzer, G., “*Nanocrystalline soft magnetic materials*” Handbook of Mag. Mater., (1997) K.H.J. Buschow(ed), vol.10, p.427
- [1.21] Alben, R., Becker, J. J. and Chi, M. C. “*Random anisotropy in amorphous ferromagnets*” J. Appl. Phys. (1978), vol. 49, p1653
- [1.22] Sawa, T. and Takahashi, Y., “*Magnetic properties of FeCu (3d transition metals) SiB alloys with fine grain structure*” J. Appl. Phys. 67 (1990) 5565
- [1.23] Dalpadodo, R. N. G. and Shirac, K., “*Barkhausen noise controlled by electric current through core*” J. Appl. Phys. 52 (1981) 1917
- [1.24] Buttino, G., Cecchetti, A., Poppi, M. and Zini, G., “*Permeability of ferromagnetic amorphous ribbons carrying AC and DC electric currents*” J. Magn. Mat. 41 (1984) 205-208
- [1.25] Hakim, A., Manjura Haque, S., “*Effect of structural parameters on soft magnetic properties of two phase nanocrystalline alloy of Fe_{73.5}Cu₁Ta₃Si_{13.5} B₉*” J. Magn. Magn. Mater. 284 (2004) 395-402
- [1.26] Franco, V., Conde, C.F., Conde, A., Kiss, L.F., “*Superparamagnetic behaviour in an Fe₇₆Cu₁Nb₃Si_{10.5}B_{9.5} alloy*” J. Magn. Magn. Mater. 215- 216 (2000) 400-403
- [1.27] C. Y. Um and M. E. McHenry, “*Magnetic properties of Fe-Nb-Ta-Mo-B alloys*” IEEE Trans. Magn. 40(4) (2004) 2724-2726

References for Chapter 2

- [2.1] McHenry, M. E., Willard, M. A. and Laughlin D. E., “*Amorphous and nanocrystalline materials for applications as soft magnets*” Prog. Mat. Sci. 44 (1999) 29-433.
- [2.2] Herzer, G., ‘*Nanocrystalline soft magnetic alloys*’, Handbook of Mag. Mater., K.H.J. Buschow(ed), 10 (1997) 415-462
- [2.3] Hono, K., Higara, K., Wang, Q., Inoue, A. and Sakurai, T., “*The microstructure evolution of a $Fe_{73.5}Si_{13.5}B_9Nb_3Cu_1$ nanocrystalline soft magnetic material*” Acta Metall. Mater. 40(9) (1992) 2137-2147
- [2.4] Hono, K. and Sakurai, T., “*Atom probe studies of nanostructured alloys*” Appl. Surf. Sci. 87-88 1995 166
- [2.5] Ayers, J. D., Harris, V. G., Sprague, J. A. and Elan, W. T., “*On the role of Cu and Nb in the formation of nanocrystals in amorphous $Fe_{73.5}Nb_3Cu_1Si_{13.5}B_9$* ” Appl. Phys. Lett. 64 (1994) 974
- [2.6] Köster, U., Schünemann, U., Blank-Bewersdorff, M., Brauer, S., Sutton, M. and Stephenson, G. B., “*Nanocrystalline materials by crystallization of metal-metalloid glasses*” Mat. Sci. Eng. A 133 (1991) 611-615
- [2.7] Yoshizawa, Y. and Yamauchi, K., 1991a, “*Magnetic Properties of Nanocrystalline Fe-Based Soft Magnetic Alloys*” Mater. Res. Soc. Symp. Proc. 232 183.
- [2.8] Sorescu, M., Um, C.Y., McHenry, M. E., Diamandescu, L., “*Thermal behavior of substituted FeCo-based metallic glasses*” J. Non-Crys. Sol. 351(2005) 663–667
- [2.9] Szumiata, T., Gawroński, M., Brzózka, K., Górka, B., Sovák, P., Pavlík, G., “*The influence of Co and V substitution on structural properties of FINEMET-type alloys*”, NUKLEONIKA 2007; 52(Supplement 1): S21–S28
- [2.10] Altube, A., Pierna, A. R., “*Thermal and Electrochemical properties of cobalt containing Finemet type alloys*” Electrochimica Acta 49 (2004) 303–311
- [2.11] Herzer, G., and Warlimont, H., “*Nanocrystalline soft magnetic materials by partial crystallization of amorphous alloys*” Nanostruct. Mater. 1 1992 263-268
- [2.12] Kataoka, N., Matsunaga, T., Inoue, A. and Masumoto, T., “*Soft Magnetic Properties of b.c.c. Fe-Au-X-Si-B (X=Early Transition Metal) Alloys with Fine Grain Structure*” Mater. Trans. JIM 30 1989 947-950
- [2.13] Yoshizawa, Y. and Yamauchi, K., “*Magnetic properties of Fe-Cu-M-Si-B (M = Cr, V, Mo, Nb, Ta, W) alloys*” Mater. Sci. Eng. A 133(1991)176
- [2.14] Müller, M., and Matern, N., “*The influence of refractory element additions on the magnetic properties and on the crystallization behaviour of nanocrystalline soft magnetic Fe-B-Si-Cu alloys*” J. Mag. Mater. 136 (1994) 79

- [2.15] Inoue, A., Kobayashi, K., Kanerhira, J. and Masumoto, T., “*Mechanical properties and thermal stability of (Fe-Co-Ni)-M-B (M=IV, V and VI group transition metals) amorphous alloys with low boron concentration*”, Sci. Rep. Res. Inst. Tohoku Univ.(1981),vol. A 29, p.331-342
- [2.16] Suzuki, K., Makino, A., Kataoka, N., Inoue, A. and Masumoto, T., “*Soft magnetic properties of nanocrystalline b.c.c. Fe-Zr-B and Fe-M-B-Cu (M=transition metal) alloys with high saturation magnetization*” J. Appl. Phys., 70(10) (1991) 6232-6237
- [2.17] Suzuki, K., Makino, A., Inoue, A. and Masumoto, T. “*Low core losses of nanocrystalline Fe-M-B (M=Zr, Hf, or Nb) alloys*” J. Appl. Phys., (1993), vol. 74, p.3316
- [2.18] Kubaschewsky, O., “*Iron-binary phase diagrams*”, Springer Verlag, Berlin, Heidelberg, N. Y., Verlag stahleisen mbH. Dusseldorf (1982)
- [2.19] Herzer, G., IEEE Trans. Magn., “*Grain structure and magnetism of nanocrystalline ferromagnets*” 25(5) (1989) 3327-3329.
- [2.20] Hampel, G., Pundt, A. and Hesse, J., “*Crystallization of $Fe_{73.5}Cu_1Nb_3Si_{13.5}B_9$ structure and kinetics examined by X-ray diffraction and Mossbauer effect spectroscopy*” J. Phys. Cond. Mater. 4 (1992) 3195
- [2.21] Gómez-Polo, C., Marín, P., Pascual, L., Hernando, A., and Vázquez, M., “*Structural and magnetic properties of nanocrystalline $Fe_{73.5}Co_xSi_{13.5}B_9CuNb_3$ alloys*”, Phys. Rev. B, vol. 65 The American Physical Society, 2001 024433(1-6)

References for Chapter 3

- [3.1] Gallagher, K. A., Willard, M. A., Zabenkin, V. N., Laughlin, D. E., McHenry, M.E., “*Distributed exchange interactions and temperature dependent magnetization in amorphous $Fe_{882-x}Co_xZr_7B_4Cu_1$ alloys*” J. Appl. Phys. 85(5) (1999) 5130-5132
- [3.2] Turnbull, D., “*Under what conditions can a glass be formed?*” Contemp. Phys. 10 (1969) 473-488
- [3.3] Johnson, W. L., “*Thermodynamic and kinetic aspects of the crystal to glass transformation in metallic materials*” Progress in materials science, 30 (1986) 81-134
- [3.4] Louca, D., Ahn, K., Ponnambalam V., and Poon, S. J., “*Local order in amorphous Fe-alloys*” Mat. Res. SOC. Proc. 754, (2003) PP.CC 7.7.1.-CC 7.7.6.
- [3.5] Spaepen, F., and Turnbull, D., “*Metallic Glasses*” Ann. Rev. Phys. Chem., 35 (1984) 241-263
- [3.6] Fulcher, G., “*Analysis of recent measurements of the viscosity of glasses*” J. Am. Ceram. Soc., 8(6) (1925) 339-355
- [3.7] Harris, R., Plischke, M. and Zuckerman, M. J., “*New model for amorphous magnetism*” Phys. Rev. Lett. 31 (1973) 160-162.

- [3.8] Cohen, M. H., and Turnbull, D., “*Composition Requirements for Glass Formation in Metallic and Ionic Systems*” *Nature* 189 (1961) 131-132
- [3.9] Berkowitz, A. E., Walter, J. L., Wall, K. F. “*Magnetic properties of amorphous particles produced by Spark Erosion*” *Phys. Rev. Lett.* (1981) **46** 1484
- [3.10] Takayama, S., “*Amorphous structure and their formation and stability*” *J. Mater. Sci.*, 11(1) (1976) 164-185
- [3.11] Irvine, J. T. S., Amano, E., Huanosta, A., Valenzuela, R., West, A.R., “*Characterization of magnetic materials by impedance spectroscopy*” *Solid State Ionics* 40/41(1990) 220-223
- [3.12] Murray, P. and White, J., “*Kinetics of the thermal dehydration of clays*”, *Trans. Brit. Ceram. Soc.* 48 (1949) 187-206
- [3.13] Murray, P. and White, J., “*Kinetics of thermal decomposition of clay. 2. Isothermal decomposition of clay materials*”, *Trans. Brit. Ceram. Soc.* 54 (1955) 151-187
- [3.14] Murray, P. and White, J., “*Kinetics of thermal decomposition of clay 4. Interpretation of the differential thermal analysis of clays*”, *Trans. Brit. Ceram. Soc.* 54 (1955) 204-237
- [3.15] Sewel, E. C., “*The consequences for differential thermal analysis of assuming a reaction to be first order*”, *Clay Minerals Bul.* 2 (1955) 233-241
- [3.16] Kissinger, H. E., “*Reaction Kinetics in Differential Thermal Analysis*” *Anal. Chem.* 29(11) (1957) 1702-1706
- [3.17] Boswell, F.G., “*On the calculation of activation energies using a modified Kissinger method*” *J. Therm. Anal.* 18(2) 1980 353-358
- [3.18] Cullity, B.D., “*Elements of X-ray diffraction*” Addison-Wesley, 1978.
- [3.19] Massalski T.B., “*Binary alloy phase diagrams*”, Materials Park, ASM International, USA, 1990.
- [3.20] Kouvel, J.S., “*Magnetism and Metallurgy*”, eds. A. Berkowitz and E. Kneller (Academic Press, New York, 1969) Vol. 2, p. 523.
- [3.21] MacLaren, J.M., Crampin, S., Vvedensky, D.D., Eberhart, M.E., “*Mechanical stability and charge densities near stacking faults*” *Phys. Rev. Lett.* 63(23) (1989) 2586-2589.
- [3.22] Coey, J.M.D., “*Rare-earth iron permanent magnets*”, Oxford Science Publications, Clarendon Press, 1996.
- [3.23] Skomski, R, Coey, J.M.D., “*Giant energy product in nano-structured two-phase magnets*” *Phys. Rev. B* 48(21) (1993) 15812.
- [3.24] Hilzinger, H.R., Hillmann, H., Mager, A., “*Magnetostriction measurements on Co-base amorphous alloys*” *Phys. Stat. Sol. (a)* 55(2) (1979) 763-769.

- [3.25] Pfeifer, F., Radeloff, C., “*Soft magnetic Ni-Fe and Co-Fe alloys - some physical and metallurgical aspects*” J. Magn. Magn. Mater. 19 (1980) 190-207.
- [3.26] Gengnagel, H. and Wagner, H., “*Magnetfeldinduzierte Anisotropie an FeAl-und FeSi-Einkristallen*” Z. Angew. Phys. 8, (1961) 174
- [3.27] Herzer, G., “*Grain structure and magnetism of nanocrystalline ferromagnets*” IEEE Trans. Magn., 25(5) (1989) 3327-3329
- [3.28] Herzer, G., “*Grain size dependence of coercivity and permeability in nanocrystalline ferromagnets*” IEEE, Trans. Magn. 26 (1990) 1397-1402
- [3.29] Chudnovsky, E. M., Saslow, W. M., Serota, R. A., “*Ordering in ferromagnets with random anisotropy*” Phys. Rev. B 33 (1986) 251
- [3.30] Ślawska-Waniewska, A., Nowicki, P., Lachowicz, H. K., Gorria, P., Barandiarán, J. M. and Hernando, A., “*Magnetic interactions in Fe-Zr-B-Cu nanocrystalline materials at elevated temperatures*” Phys. Rev. B 50(9) (1994) 6465-6467
- [3.31] Bean CP, Livingston JD. “*Superparamagnetism*” J. Appl. Phys. 30(4) (1959) S120.
- [3.32] Smith, C., “*Magnetic shielding to multi-gigawatt magnetic switches ten years of amorphous magnetic applications*” IEEE Trans. Mag. 18(6) (1982) 1376-1381.
- [3.33] Hernando, A., Kulik, T., “*Exchange interactions through amorphous paramagnetic layers in ferromagnetic nanocrystals*” Phys. Rev. B 49(10) (1994) 7064-7067
- [3.34] Hernando, A., Navarro, I. In: Hadjipanyis GC, Siegel, RW, editors. “*Nanophase Materials, Synthesis, Properties, Applications*”, The Netherlands: Kluwer, 1994. p.703
- [3.35] A. Hernando, I. Navarro, and P. Gorria, “*Iron exchange-field penetration into the amorphous interphase of nanocrystalline materials*” Phys. Rev. B 51(5) (1995) 3281-3284.
- [3.36] A. Hernando, M. Vázquez, T. Kulik, and C. Prados, “*Analysis of the dependence of spin-spin correlations on the thermal treatment of nanocrystalline materials*” Phys. Rev. B 51(6) (1995) 3581-3586.
- [3.37] Hernando A, Marin P, Vazquez M, Herzer G., “*Thermal dependence of coercivity in magnetic nanostructures*” J. Magn. Magn. Mater. 177-181 (2) (1998) 959-961.
- [3.38] Bozorth, R., “*Ferromagnetism*” (D. van Nostrand, Princeton, N.J.) (1951) 76.

References for Chapter 5

- [5.1] McHenry, M. E., Willard, M. A. and Laughlin D. E., “*Amorphous and nanocrystalline materials for applications as soft magnets*” Prog. Mat. Sci. 44 (1999) 29-433.
- [5.2] Manjura Hoque, S., Hakim, M. A., Khan, F. A., Chau, N., “*Ultra-soft magnetic properties of devitrified $Fe_{75.5}Cu_{0.6}Nb_{2.4}Si_{13}B_{8.5}$ alloy*” Mat. Chem. Phys. 101 (2007) 112-117.
- [5.3] Marzo, F.F., Pierna, A. R., Altube, A. A., “*Analysis of nanocrystallization of Finemet type alloy by temperature-modulated differential scanning calorimetry*” Journal of Non-Crystalline Solids 287(2001) 349-354
- [5.4] Chien, C. L. and Hasegawa, R.S.; “*Mössbauer study of glassy alloys $(Fe-Mo)_{80}B_{20}$* ” J. Appl. Phys. 49(3) (1978) 1721
- [5.5] Yoshizawa, Y., Oguma, S., Yamauchi, K. “*New Fe-based soft magnetic alloys composed of ultrafine grain structure*” J. Appl. Phys. 64(10) 1988 6044-6046
- [5.6] Yoshizawa, Y. and Yamachi, K. “*Fe-based soft magnetic alloys composed of ultrafine grain structure*”, Mater. Trans. JIM. 31 (1990a) 307
- [5.7] Liu, T., Chen, N., Xu, Z. X., Ma, R. Z. “*The amorphous to nanocrystalline transformation in $Fe_{73.5}Cu_1Nb_3Si_{13.5}B_9$ studied by thermogravimetry analysis*” J. Magn. Mater. 152 (1996) 359-364
- [5.8] Noor, S., “*Effects of two-step annealing on complex permeability of Fe-Cu-Nb-Si-B nanocrystalline soft magnetic materials*” M.Phil Thesis, March 2005, KUET, p70-72
- [5.9] Papaioannou, T. J., Svec, P., Janickovic, D., Karagianni, C. S., Hristoforou E., “*Phase transformations of Co-enhanced Finemet amorphous ribbons based on resistance-temperature Measurements*” J. Optoelect. Adv. Mater. 10(5) (2008) 1048 – 1051
- [5.10] Altube, A., Pierna, A. R., “*Thermal and electrochemical properties of cobalt containing Finemet type alloys*” Electrochimica Acta 49 (2004) 303-311
- [5.11] Gómez-Polo, C., Marín, P., Pascual, L., Hernando, A., and Vázquez, M., “*Structural and magnetic properties of nanocrystalline $Fe_{73.5}Co_xSi_{13.5}B_9CuNb_3$ alloys*”, Phys. Rev. B, vol. 65 The American Physical Society, 2001 024433(1-6)
- [5.12] Bozorth, “*Ferromagnetism*”, D. Van Norstrand Company, Inc., Princeton, NJ, 1964, p. 64
- [5.13] Sorescu, M., Um, C.Y., McHenry, M. E., Diamandescu, L., “*Thermal behavior of substituted FeCo-based metallic glasses*” J. Non-Crys. Sol. 351(2005) 663–667

- [5.14] Szumiata, T., Gawroński, M., Brzózka, K., Górka, B., Sovák, P., Pavlík, G.,
“The influence of Co and V substitution on structural properties of FINEMET-type alloys”
 NUKLEONIKA 2007 52(Supplement 1) S21–S28
- [5.15] Szewieczek, D., Raszka, T., *“Structure and magnetic properties
 of $Fe_{63.5}Co_{10}Cu_1Nb_3Si_{13.5}B_9$ alloy”* J. Achiev. Mater. Manf. Eng. 18(1-2) 2006 179-182
- [5.16] Chen, W. Z., Ryder, P. L., *“X-ray and differential scanning calorimetry study of
 amorphous $Fe_{63.5}Co_{10}Cu_1Nb_3Si_{13.5}B_9$ alloy”* Mater. Sci. Eng., B(34)1995 204-209
- [5.17] Borrego, J.M., Conde, C.F., Conde, A., Grenèche, J.M., *“Crystallization of Co-
 containing Finemet alloys”* J. Non-Crys. Solids, 287 (2001) 120-124
- [5.18] Franco, V., Conde, C. F., Conde, A., *“Changes in magnetic anisotropy distribution
 during structural evolution of $Fe_{76}Si_{10.5}B_{9.5}Cu_1Nb_3$ ”* J. Magn. Magn. Mat. 185 (1998) 353-359
- [5.19] Kubaschewsky, O., *“Iron-binary phase diagrams”*, Springer Verlag, Berlin, Heidelberg,
 N. Y., Verlag stahleisen mbH. Dusseldorf (1982)
- [5.20] Kneller, E. F., and Luborsky, F. E., *“Particle Size Dependence of Coercivity and
 Remanence of Single-Domain Particle ”*, J. Appl. Phys. 34 (1963) 656
- [5.21] Herzer, G., *“Grain Size Dependence of Coercivity and Permeability in nanocrystalline
 ferromagnets”*, IEEE Trans. Magn. , 26 (1990) 1337
- [5.22] Yoshizawa, Y., Oguma, S., Yamauchi, K., *“New Fe-based soft magnetic alloys
 composed of ultrafine grain structure”*, J. Appl. Physics. 64 (1988) 6044-6046
- [5.23] Cullity, B. D., *“Elements of X-Ray Diffraction”*, Adison-Wisley publishing company
 Inc., London, England, 1959, p. 262
- [5.24] Rubinstein, M., Harris, V. G. and Lubtiz, P., *“Ferromagnetic resonance in
 nanocrystalline $Fe_{73.5}Cu_1Nb_3Si_{13.5}B_9$ alloy”*, J. Magn. Magn. Mat. 234 (2001) 306-312
- [5.25] Luborsky, F. E., Decker, J. J. & R. O. McCary, *“Magnetic annealing of amorphous
 alloys”* IEEE Trans. Mag. 11(6) (1975) 1644-1649
- [5.26] Franco, V., Conde, C.F., Conde, A., Kiss, L.F., *“Superparamagnetic behavior in an
 $Fe_{76}Si_{10.5}B_{9.5}Cu_1Nb_3$ alloy ”*, J. Magn. Magn. Mater. 215-216 (2000) 400-403
- [5.27] Pfeiffer, H., and Schüppel, W., *“Temperature dependence of the magnetization in fine
 particle systems and the Hopkinson effect. Application to barium ferrite powders”* J. Magn.
 Magn. Mat. 130 (1994) 92-98
- [5.28] Herzer, G., *“Nanocrystalline soft magnetic materials”* Handbook of Mag. Mater.,
 K.H.J. Buschow(ed), 10 (1997) 415-462

- [5.29] Mørup, S., Christensen, P. H. and Clausen B. S., “*Magnetic hyperfine splitting in superparamagnetic particles in external magnetic fields*” J. magn. Magn. Mat. 68 (1987) 160-170
- [5.30] Lachowicz, H.K. and Slawska-Waniewska, A. “*Coexistence of various magnetic phases in nanocrystalline Fe-based metallic glasses*” J. Magn. Magn. Mat. 133 (1994) 238-242
- [5.31] Olzewski, A., Zbroszczyk, J., Olzewski, J., Cieurzyńska, W.H., Fukunaga, H., Narita, K., “*Magnetic behavior of amorphous and nanocrystalline $Fe_{92-x}Zr_7Cu_1B_x$ (x=2 or 6) alloys*” J. Mag. Mag. Mater. 215-216 (2000) 422

